Summer 7-1-2019

Nonpolar GaN-Based VCSELs with Lattice-Matched Nanoporous Distributed Bragg Reflector Mirrors

Saadat M. Mishkat-Ul-Masabih
University of New Mexico - Main Campus

Saadat M. Mishkat-Ul-Masabih

Candidate

Electrical & Computer Engineering

Department

This dissertation is approved, and it is acceptable in quality and form for publication:

Approved by the Dissertation Committee:

Dr. Daniel F. Feezell , Chairperson

Dr. Ganesh Balakrishnan

Dr. Sang M. Han

Dr. Ting S. Luk

NONPOLAR GAN-BASED VCSELS
WITH LATTICE-MATCHED NANOPOROUS
DISTRIBUTED BRAGG REFLECTOR MIRRORS

by

SAADAT M. MISHKAT-UL-MASABIH

B.S. in Electronics & Telecomm. Eng., North South University, 2011
M.S. in Electrical Engineering, University of New Mexico, 2016

DISSERTATION

Submitted in Partial Fulfillment of the
Requirements for the Degree of

Doctor of Philosophy
Engineering

The University of New Mexico
Albuquerque, New Mexico

July 2019

To my parents and my siblings,

for always inspiring me to shoot for the stars.

Acknowledgements

I am grateful to many people for making this work possible. First and foremost, I would like to thank my advisor Prof. Daniel Feezell for his dedicated guidance and support. Early on in my degree, I remember him mentioning that VCSEL projects are always of high risk and high reward. For the longest time, I doubted myself on whether I would be able to fulfill all the project requirements. But, Prof. Feezell believed in my ability and urged me to push forward which ultimately lead to groundbreaking results from my VCSEL project. Not only did I learn a ton from his vast knowledge on III-nitride materials and devices, his constructive criticisms greatly improved the quality of my work and allowed me to grow as a researcher.

Next, I am thankful to my committee members and collaborators, Prof. Ganesh Balakrishnan, Prof. Sang Han, and Dr. Ting Luk for their time and suggestions. Their valuable insight on optical, electrical, and mechanical properties of semiconductors helped me tremendously in understanding the material characteristics and device performance of my VCSELs.

I cannot express the immense gratitude I feel for my fellow group members, both past and present. All of whom have helped me towards the completion of my PhD in some way or another. Many thanks to Ashwin, Morteza, Mohsen, and Mike for introducing me to MOCVD and for taking care of my growths when I was busy doing something else. Discussions regarding fabrication with Andrew, Mahmoud, Rhett, Kenny, Farnood, and Abdel have always helped me in developing processes very

quickly and reliably. I am also grateful to Serdal, Arman, and Isaac for assisting me in various material and device related characterizations.

Many of the accomplishments mentioned in this thesis could not have been possible without the support of the technical and/or administrative staff. As such, I am forever indebted to the ECE, CHTM, and CINT staff members for putting up with my numerous requests and questions throughout the years.

Beyond the appreciation of the technical side of things, I would like to thank all my friends from back home and the ones I made during the course of my study. They were always there to lend a helping hand or to simply distract me from work whenever graduate student life became too overwhelming. Furthermore, I must also acknowledge the Bangladeshi community here at UNM for making Albuquerque feel like home, even though my real home is half-way around the world. Looking back, I will forever cherish these memories.

Last, but certainly not least, I would like to thank my parents, my older sister, and my younger brother. I would not be where I am at today without their unconditional love and encouragement. They have sacrificed a lot so that I can pursue a career of my choice, even if it meant me being away from home for an extended period time. I only hope that the work I performed in this thesis is substantial enough to repay them and make them proud.

Nonpolar GaN-Based VCSELs with Lattice-Matched Nanoporous Distributed Bragg Reflector Mirrors

by

Saadat M. Mishkat-Ul-Masabih

B.S. in Electronics and Telecommunication Engineering, North South University, 2011

M.S. in Electrical Engineering, University of New Mexico, 2016

Ph.D. in Electrical Engineering, University of New Mexico, 2019

ABSTRACT

Wide-bandgap optoelectronic devices have undergone significant advancements with the advent of commercial light-emitting diodes and edge-emitting lasers in the violet-blue spectral region. They are now ubiquitous in several lighting, communication, data storage, display, and sensing applications. Among the III-nitride emitters, vertical-cavity surface-emitting lasers (VCSELs) have attracted significant attention in recent years due to their inherent advantages over edge-emitting lasers. The small active volume enables single-mode operation with low threshold currents and high modulation bandwidths. Their surface-normal device geometry is conducive to the cost-effective formation of high-density 2D arrays while simplifying on-chip wafer testing. Furthermore, the low beam divergence and circular beam profiles in VCSELs allow efficient fiber coupling.

Nevertheless, GaN-based VCSELs are still in the early stages of development. Several challenges need to be addressed before high-performance devices can be commercially realized. One such challenge is the lack of high-quality distributed Bragg reflector (DBR) mirrors. Conventionally, epitaxial and dielectric DBRs are used which often involve complex growth and fabrication techniques. This dissertation provides an alternative

approach where subwavelength air-voids (nanopores) are introduced in alternating layers of doped/undoped GaN to form the DBR structure. Selective electrochemical etching creates nanopores in the doped layers, reducing the effective refractive index relative to the surrounding undoped GaN. Using only 16-pairs, DBR reflectance >99.9% could be achieved. Several research groups have shown optically pumped VCSELs using nanoporous DBRs on *c*-plane. However, there are no reports of electrically injected nanoporous VCSELs. Using *m*-plane GaN substrates, we have demonstrated the first ever electrically injected GaN-based VCSEL using a lattice-matched nanoporous DBR. The nonpolar *m*-plane orientation is beneficial for leveraging the higher per-pass gain and polarization-pinning properties absent in *c*-plane. Lasing under pulsed operation at room temperature was observed at 409 nm with a linewidth of ~0.6 nm and a maximum output power of ~1.5 mW. This is the highest output power from *m*-plane VCSELs to date with relatively stable operation at elevated temperatures. All tested devices were linearly polarization-pinned in the *a*-direction with high polarization ratios >0.9. Overall, the nanoporous DBRs help in mitigating some of the issues that limit the performance of III-nitride VCSELs.

Table of Contents

List of Figures

List of Tables

1. Introduction

In 1977, Prof. Kenchi Iga and his team proposed the concept of the vertical-cavity surface-emitting laser (VCSEL). The first device was demonstrated in GaInAsP/InP systems in 1979 [1,2] and it took another 17 years before the VCSEL could be commercially realized by Honeywell [3]. Since then, development of VCSELs has heavily focused on the red to infrared spectral range resulting in the global upsurge of companies specializing in arsenide and phosphide-based VCSELs. Such materials were of interest due to the wide assortment of alloys available with minimal lattice constant mismatch allowing the growth of low defect density epilayers. However, this was not the case in the lower visible and ultra-violet range of the spectrum. Several material related issues needed to be addressed before a functioning light-emitting device could be fabricated.

Group-III nitrides and its alloys have sufficiently large bandgaps to allow light emission in the shorter wavelengths. For the longest time, the major issue plaguing the III-nitride material system was the absence of p-type doping. In 1989, the research group of Prof. Isamu Akasaki and Prof. Hiroshi Amano epitaxially grew the first p-GaN by activating the Mg-doping as an acceptor using low energy electron beam irradiation [4]. Soon after, they developed the first GaN-based p-n homojunction light-emitting diode (LED). Following this breakthrough, Prof. Shuji Nakamura demonstrated the double-heterostructure InGaN/GaN LED in 1994 [5]. Recognized for their groundbreaking work in nitride material systems and contributions to modern lighting technology, Prof. Akasaki, Prof. Amano, and Prof. Nakamura were awarded the Nobel Prize in Physics in 2014.

Lattice-matched substrates for the growth of III-nitride crystals are still scarce. Growth of GaN is usually performed on non-native substrates such as SiC or sapphire [6]. The lattice constant mismatch along with the difference in thermal expansion coefficients results in a very high density of threading dislocations (~10^8-10^{10} cm^{-2}). This does not adversely affect the spontaneous operation characteristic in LEDs [7]. However, in laser diodes (LDs), such high defect density is severely detrimental to the device performance and lifetime.

Out of all the challenges hindering the progress of GaN-based VCSELs, none is more critical than the integration of high reflectance mirrors. Due to the narrow gain region in VCSELs, very high reflectance distributed Bragg reflectors (DBRs) are required on either side of the cavity to provide the resonant feedback. Unlike the mature GaAs- and InP-based DBRs, GaN-based systems lack lattice-matched high-refractive-index contrast materials necessary to make high quality DBRs. There is only one III-nitride alloy ($Al_{0.82}In_{0.18}N$) that is lattice matched to GaN but the refractive index difference is very low. DBRs comprising of any other III-nitride alloys would generate strain-induced defects in the stack, increasing the scattering loss and reducing the reflectance. Often complex VCSEL structures involving dielectric DBRs are used to mitigate this is difficulty.

This thesis will primarily focus on solving the challenge of incorporating DBRs in the VCSEL cavity. An unconventional method is proposed a where lattice-matched DBR with large refractive index contrast layers can be obtained relatively easily. But before we delve in the details of this new kind of DBR, one must understand the device principles and the material system for GaN-based VCSELs. The chapter will begin with a brief discussion of the fundamental concepts of a VCSEL, followed by the group III-nitride material system,

emphasizing the nonpolar crystal orientation and its benefits. Some potential applications for GaN-based VCSELs are presented next. Finally, the chapter will provide a review of existing design considerations for electrically injected GaN-based VCSELs and explain the motivation behind our design.

1.1. Operating principles of VCSELs

The device architecture of a laser diode can be classified into two categories: edge-emitting and surface-emitting. Edge-emitting laser diodes (EELDs) emit from one of the side facets of the structure which is in-plane to the epilayers, and VCSELs emit perpendicular to the growth plane from the top surface of the device. Figure 1.1 shows a schematic of the two different LD device architectures. The long gain regions in EELDs allow for low reflectance facets (~30%) to form the cavity. On the other hand, due to their vertical orientation, the gain region in VCSELs is very thin, which requires very high mirror reflectance (>99%) to achieve lasing. It is also this property which enables VCSELs to have a much smaller device footprint compared to EELDs [8]. The reduced size implies that devices will have lower threshold currents and thus reduced heating and the short cavity length would enable single-mode operation. Furthermore, the surface-normal geometry is conducive to the cost-effective formation of high-density 2-D arrays. VCSELs also have a circular beam profile with low beam divergence allowing efficient fiber coupling and significantly simplify on-chip testing. Their relatively small cavity volumes also results in higher modulation bandwidths at low bias currents than their edge-emitting counterparts [9].

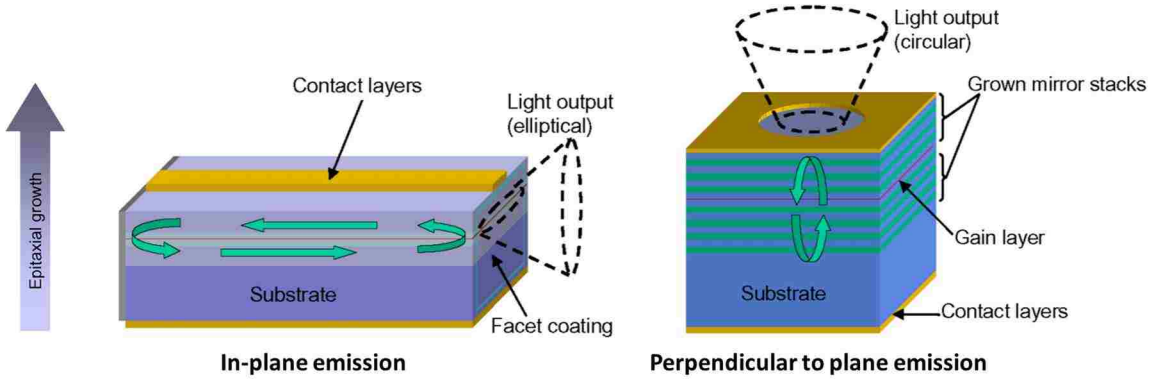

Figure 1.1. Schematic of EELD and VCSEL, showing the epitaxial growth direction, resonant cavity, emission direction, and emission profile. Reprinted from [10].

Figure 1.2 shows the VCSEL structure in more detail. Optical confinement forms the coherent electric field (modes) inside the cavity volume. In a VCSEL, the longitudinal mode confinement (normal to substrate) is achieved by the top and bottom DBRs. Whether the VCSEL is a single- or a multi-longitudinal mode device is determined by the effective cavity length. The effective cavity length approximates the actual cavity length of a VCSEL. It considers the effect of the modal penetration depth into both DBRs plus the thickness of the p-side, active region, and the n-side of the device. One important criterion that needs to be met for a VCSEL is the alignment of the longitudinal mode peak to the center of the active region. This ensures proper coupling of the electric field with the multiple quantum-wells (MQWs), maximizing the gain enhancement factor and thereby increasing the total confinement factor. The transverse-mode (radially outward) confinement can be achieved in a number of ways, such as ion implantation, dielectric step, air-gap, recessed steps, etc. The size of the aperture and the index difference between the central core and outer cladding region determines the number of transverse-modes that can exist within the aperture. These modes can vary in wavelength as well as in the near-field and far-field emission patterns. Figure 1.2 shows the lowest order fundamental linearly-polarized mode $LP_{0,1}$, where 0 is the azimuthal modal index l and 1 is the radial modal

index m. Factors like current spreading profiles and self-heating also govern the mode profile shape to some extent. Whether the VCSEL is top-emitting or bottom-emitting is determined by the mirror reflectances of the DBRs. Here, in Fig. 1.2, the device is a top-emitting device due to the top DBR reflectance being lower than the bottom DBR reflectance ($R_{top} < R_{bottom}$). The peak DBR reflectance is generally controlled by the refractive index difference between the layers in the DBR and the number of pairs used to form the DBR structure.

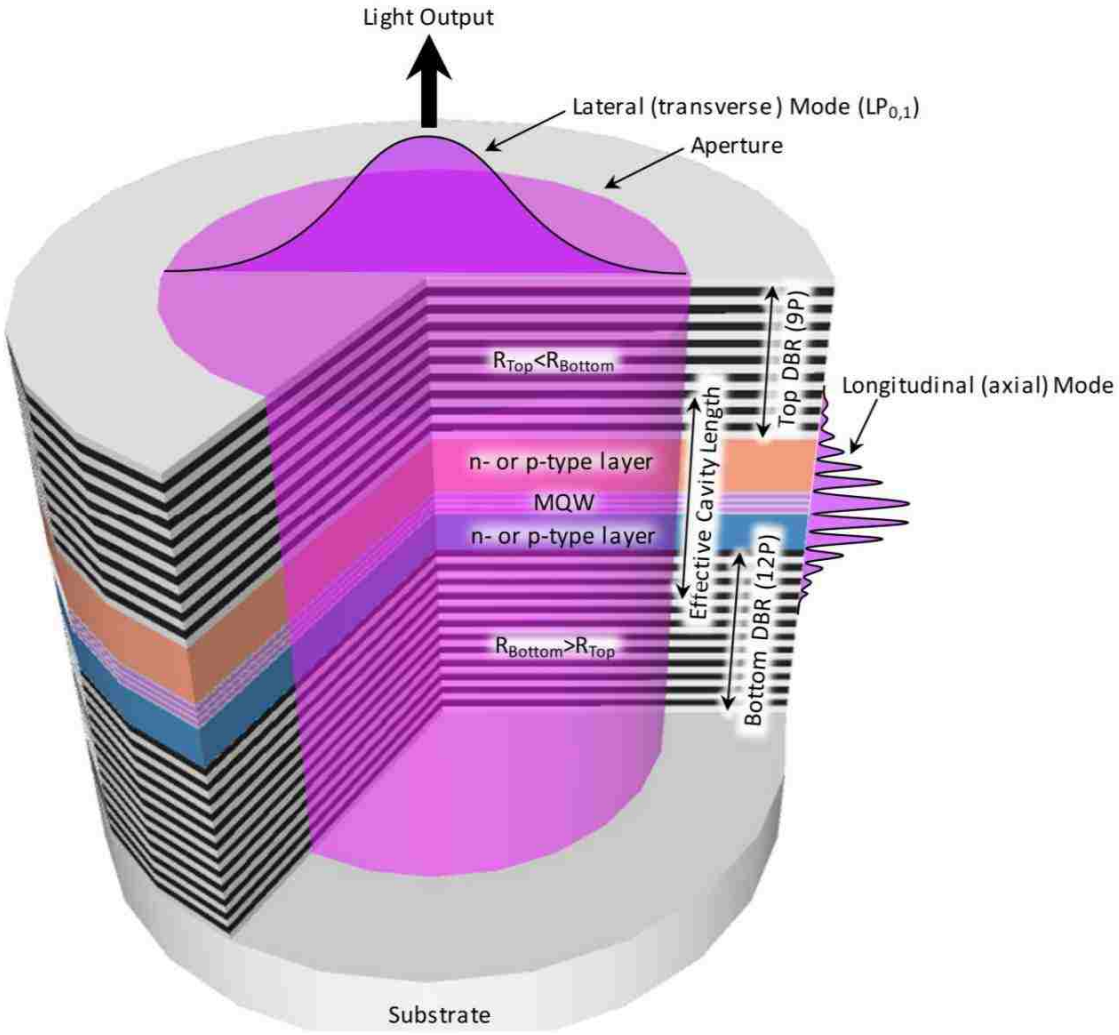

Figure 1.2. Cross-sectional schematic of a VCSEL, showing the longitudinal and transverse mode profiles within the cavity volume. Reprinted from [11].

The following section will investigate some of the fundamental laser equations and the internal parameters in a VCSEL. Transmission Matrix Method (TMM) is an invaluable tool used to determine these parameters. It is a simple 1-D analysis which describes the interaction of electromagnetic waves with matter. The TMM analysis program Vertical™ was used to simulate the standing-wave profile of the cavity and the DBR reflectance spectra to calculate the relevant VCSEL parameters.

TMM works by defining the interaction of propagating electric fields with the bulk of the layers and the interfaces between them [9,11]. The transmission matrix of the field through a bulk layer is given by

$$T_{bulk} = \begin{pmatrix} e^{i\beta L} & 0 \\ 0 & e^{-i\beta L} \end{pmatrix}, \tag{1.1}$$

where L is the layer thickness and β is the propagation constant defined as

$$\beta = \frac{2\pi\bar{n}}{\lambda}. \tag{1.2}$$

Here, λ is the wavelength of interest and $\bar{n}$ is the complex refractive index of the mode. $\bar{n}$ is given as

$$\bar{n} = n - ik, \tag{1.3}$$

where n is the real refractive index and k is the extinction coefficient related to the layer absorption coefficient α by

$$\alpha = \frac{4\pi k}{\lambda}. \tag{1.4}$$

Now, considering two adjacent layers, the transmission matrix for a field travelling through the interface from layer 1 to layer 2 is defined as

$$T_{12} = \frac{1}{r_{12}} \begin{pmatrix} 1 & r_{12} \\ r_{12} & t_{12}^2 + r_{12} r_{12}^* \end{pmatrix} \tag{1.5}$$

where t_{12} is the interface transmissivity and r_{12} is the interface reflectivity with *complex* conjugate r_{12}^*. The reflectivity is given as

$$r_{12} = \frac{n_2 - n_1}{n_2 + n_1}, \tag{1.6}$$

where n_1 and n_2 are the *complex* refractive indices of layer 1 and layer 2, respectively. Similarly, the transmissivity is defined as

$$t_{12} = \sqrt{1 - \left(\frac{n_2 - n_1}{n_2 + n_1}\right)\left(\frac{n_2 - n_1}{n_2 + n_1}\right)^*}. \tag{1.7}$$

Building the entire VCSEL cavity and applying TMM analysis, one can easily obtain threshold parameters such as the round-trip gain, round-trip loss, top and bottom per-pass transmission, and the gain enhancement factor. The 1-D TMM simulations are performed using a program called Vertical^{TM}. Figure 1.3 shows a screenshot of the TMM simulations of a typical GaN-based VCSEL.

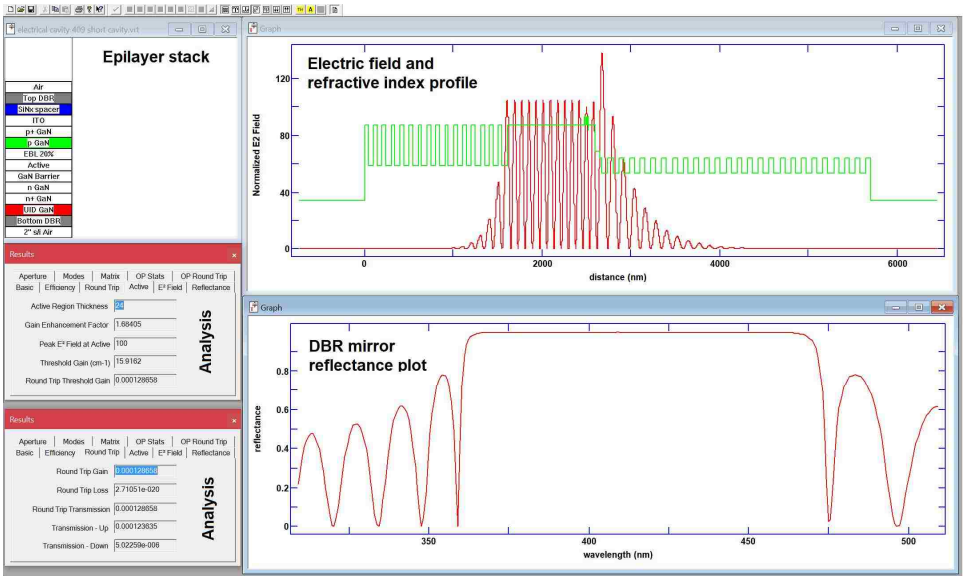

Figure 1.3. Screenshot of Vertical^{TM} with TMM analysis.

Some important device parameters are as follows.

1.1.1. Threshold modal gain

The threshold modal gain, Γg_{th}, is defined as

$$\Gamma g_{th} = \Gamma_{enh}\Gamma_{fill}\Gamma_{xy} g_{th} = \langle \alpha_i \rangle + \alpha_s + \alpha_m \tag{1.8}$$

where Γ is the total cavity confinement factor, g_{th} is the material gain at threshold, Γ_{enh} is the gain enhancement factor, Γ_{fill} is the cavity fill-factor, Γ_{xy} is the transverse mode confinement factor, $\langle \alpha_i \rangle$ is the modal internal loss, α_s is the scattering loss, and α_m is the mirror loss from both laser facets. Eqn. (1.8) describes that the total gain in the active region must be equal to the total losses inside the cavity for a laser to reach threshold. The amount of gain coupled into the mode is calculated by multiplying the material gain at threshold g_{th} with the total confinement factor Γ. The total confinement factor is divided in the three components, Γ_{enh}, Γ_{fill}, and Γ_{xy}. The enhancement factor defines the overlap of the cavity mode with the active region [9]. The value of Γ_{enh} can be a maximum of 2 if a standing wave peak is aligned perfectly with the center of a thin active region. The cavity fill-factor can easily be determined using

$$\Gamma_{fill} = \frac{N_{qw} L_a}{L_{eff}} \tag{1.9}$$

where N_{qw} is the number of quantum wells (QWs) in the active region and L_a is the thickness of a single QW. Calculating the transverse confinement factor Γ_{xy} is trickier due to the existence of transverse mode profiles with complicated shapes. It can be numerically calculated using finite element method (FEM) software programs like Lumerical™ to

model a simple 2-D core-cladding model. Typically for the fundamental mode in a wide enough aperture diameter, the value of Γ_{xy} is very close to 1 and can be ignored.

Now considering the loss parameters in Eqn. (1.8), the internal loss $\langle \alpha_i \rangle$ accounts for the numerous absorbing layers from materials inside the cavity including free-carrier absorption from doping. It is co-related directly with the extinction coefficient k of materials and can be calculated experimentally using Eqn. (1.4). The scattering loss α_s becomes prevalent when the surface roughness at interfaces or the device surface becomes significant [12]. The scattering loss term is often dropped because device is generally grown with very little surface roughness. The final loss term is the mirror loss α_m which is given as

$$\alpha_m = \frac{1}{L_{eff}} ln\left(\frac{1}{r_{top} r_{bottom}}\right) \tag{1.10}$$

where L_{eff}, r_{top}, and r_{bottom} are the effective cavity length, and top and bottom DBR reflectivity, respectively. The mirror loss determines how much of the light will escape the cavity and contribute to the total light output power. As explained earlier, the mirror reflectance of the top and bottom DBR will determine which facet the light will predominantly escape from. However, a trade-off exists as a high α_m would imply high output power but also increase the gain required at threshold. Hence, the mirror loss plays a very important role for the subsequent parameters.

1.1.2. Gain curves

Gain curves establish the relationship between the threshold modal gain Γg_{th} and the threshold current density J_{th}. The most common approximation for describing this

relationship is a three-parameter logarithmic equation obtained from empirical trends [9,13]. The gain curve equation is given as

$$\Gamma g(J_{th}) \approx N_{qw}\Gamma_{qw} g_0 ln\left(\frac{J_{th}+J_s}{N_{qw}J_{tr}+J_s}\right) \tag{1.11}$$

where N_{qw} is the number of QWs, Γ_{qw} is the average confinement factor per well, g_0 is the empirical gain coefficient, J_{tr} is the transparency current density per well, and J_s is a linearity parameter. Eqn. (1.11) shows that the modal gain increases with current density for a given number of QWs. Using this we can calculate the internal loss $\langle \alpha_i \rangle$ of a VCSEL at a given threshold current density with known mirror loss.

1.1.3. Differential efficiency

The differential efficiency is a measure of the percentage of light-output which is defined as

$$\eta_d = F\eta_i \frac{\alpha_m}{\Gamma g_{th}}. \tag{1.12}$$

Here, α_m and Γg_{th} are the mirror loss and the threshold modal gain explained in Section 1.1.1, respectively. η_i is the injection efficiency which is the fraction of terminal current that generates carriers in the active region for radiative recombination. The term F is called the F-factor which is a measure of the amount of power delivered from a particular facet relative to the total coupled light out of the cavity by the mirrors [9]. For either side of VCSEL, the F-factor is defined as,

$$F_{top} = \frac{1-r_{top}^2}{\left(1-r_{top}^2\right)+\frac{r_{top}}{r_{bottom}}\left(1-r_{bottom}^2\right)} \tag{1.13}$$

$$F_{bottom} = \frac{(1-r_{bottom}^2)e^{-\alpha L}}{(1-r_{bottom}^2)+\frac{r_{bottom}}{r_{top}}(1-r_{top}^2)} \tag{1.14}$$

where, r_{top}, and r_{bottom} are the top and bottom DBR mirror reflectivity similar to Eqn. (1.10), and the term $e^{-\alpha L}$ denotes the substrate absorption loss α for a thickness L. As an example, if $r_{top} < r_{bottom}$ then $F_{top} \gg F_{bottom}$ meaning that the VCSEL is a top-emitting device. Depending on the type of VCSEL being designed, either F-factors can be used to determine the differential efficiency.

1.1.4. DBR reflectance and cavity length

We have already established that due to the very thin axial gain region, the mirror reflectance of the DBRs needs to be very high (>99%) to increase the per-pass gain. DBRs are fundamentally 1-dimensional photonic crystals comprising of two layers of different refractive indices with $n_1 < n_2$. The two layers are alternated for a certain number of pairs M to form the DBR structure. The layers are required to have a thickness of

$$d_{1,2} = \frac{\lambda_B}{4n_{1,2}} \tag{1.15}$$

to enable phase matched partial reflection at each interface of the pairs [14]. Here, λ_B is the Bragg wavelength and the peak reflectance is given as

$$R_{top,bottom} = \left(\frac{1-b_{top,bottom}}{1+b_{top,bottom}}\right)^2 \tag{1.16}$$

with

$$b_{top} = \frac{n_s}{n_0}\left(\frac{n_1}{n_2}\right)^{2M_{top}} \quad \text{and} \quad b_{bottom} = \frac{n_1^2}{n_0 n_s}\left(\frac{n_1}{n_2}\right)^{2M_{bottom}}. \tag{1.17}$$

Here, n_0 and n_s are the incident and terminating medium refractive indices, respectively. From Eqn. (1.16) and Eqn. (1.17), generally high values of *R* can be achieved with a small number of *M* provided the difference between n_2 and n_1 is large (Δn). The stopband of the DBR is also directly proportional to the index difference Δn [8,9]. The stopband of a DBR is the spectral width over which a DBR has a mirror reflectance >99%. It is estimated as

$$\Delta\lambda_{stop} \approx \frac{2\lambda_B \Delta n}{\pi\langle\bar{n}_{gr}\rangle} \tag{1.18}$$

where $\langle\bar{n}_{gr}\rangle$ is the spatially averaged group index given by

$$\bar{n}_{gr} = \bar{n} - \lambda\frac{d\bar{n}}{d\lambda}. \tag{1.19}$$

A portion of both the top and bottom DBRs is considered a part of the total cavity length as the mode decays to zero along a finite penetration depth into the DBRs which also depends on the index contrast of the layers. This cavity length is called the effective cavity length defined as

$$L_{eff} = l_{bottom}^{DBR} + l_{cav} + l_{top}^{DBR} \tag{1.20}$$

where l_{bottom}^{DBR} and l_{top}^{DBR} are the thicknesses of the field penetration depth into the bottom and top DBRs, and l_{cav} is the optical thickness of the cavity sandwiched between the DBRs. Now, $l_{top,bottom}^{DBR}$ is defined as

$$l_{top,bottom}^{DBR} = \frac{1}{2} m_{top,bottom}^{eff} \Lambda \left[\frac{1}{1+r^2} - \frac{1}{2m_{top,bottom}^{eff}}\right] \tag{1.21}$$

with effective number of mirror periods as

$$m_{top,bottom}^{eff} = \frac{tanh\left[M_{top,bottom}\ln(n_2/n_1)\right]}{ta \quad [\ln(n_2/n_1)]}, \tag{1.22}$$

$$\Lambda = \frac{\lambda_B}{4}\left(\frac{n_1+n_2}{n_1 n_2}\right), \tag{1.23}$$

and

$$r = \frac{n_2-n_1}{n_2+n_1}. \tag{1.24}$$

Similarly, the total optical thickness of the effective cavity length can be given as

$$\chi = \frac{L_{eff} n_{eff}}{\lambda_B} \tag{1.25}$$

where n_{eff} is the effective cavity refractive index in the core region obtained from TMM simulations. Naturally, a large l_{cav} means that the effect of the DBRs on the calculation of L_{eff} would be negligible and vice versa. L_{eff} governs the number of longitudinal modes that can exist inside the cavity. The Fabry-Perot mode spacing is defined by the equation

$$d\lambda = \frac{\lambda^2}{2n_{g,eff}L_{eff}}, \tag{1.26}$$

where λ is the lasing wavelength (ideally same as λ_B) and $n_{g,eff}$ is the effective group index. Based on this Eqn. (1.26), a small L_{eff} will result in large mode spacings and allow a single-longitudinal mode to exist within the gain bandwidth.

1.1.5. Output power

In Section 1.1.2, we discussed the percentage of light being coupled out of the cavity using differential efficiency. We will now consider the actual output power from the VCSEL which is defined by the equation

$$P_o = \eta_d \frac{h\nu}{q}(I - I_{th}) \tag{1.27}$$

where η_d is the differential efficiency given in Eqn. (1.12), $h\nu/q$ is the term used for converting rate of flow of carriers into the VCSEL into photons, and $(I - I_{th})$ is the drive current above threshold [9]. Note that output power from each facet of the VCSEL can be determined in Eqn. (1.27) through the F-factor in Eqn. (1.12). Unlike EELDs, where the cavity length can be varied, it is quite difficult to determine the injection efficiency η_i to calculate the differential efficiency η_d in a VCSEL cavity. However, one can easily calculate η_d from the slope efficiency η_s of the output power vs. current plot above threshold.

$$\eta_d = \left[\frac{q}{h\nu}\right]\eta_s = \left[\frac{q}{h\nu}\right]\frac{dP_o}{dI} \qquad (I > I_{th}) \tag{1.28}$$

1.1.6. Thermal resistance

The output power of a device can be significantly hindered due to thermal roll-over. This happens when internal temperatures of the device reaches a point where non-radiative recombinations dominate over radiative recombination and the elevated temperatures red-shifts the gain spectrum relative to the cavity mode. As a result, the output power decreases with increasing current density. To quantify the thermal properties of a certain device architecture, the thermal resistance (Z_t) of the device is evaluated using

$$Z_t = \frac{\Delta T}{\Delta P_{diss}} = \frac{\delta\lambda/\delta P_{diss}}{\delta\lambda/\delta T_{hs}} \tag{1.29}$$

with

$$\Delta P_{diss} = IV - P_o. \tag{1.30}$$

Here, ΔT is the change in internal temperature of the device given in K, ΔP_{diss} is the dissipated power of the laser in mW, $\delta\lambda/\delta P_{diss}$ is the rate of change in the emission

wavelength with respect to the dissipated power, $\delta\lambda/\delta T_{hs}$ is the rate of change in the emission wavelength with respect to the stage or heatsink temperature, IV is the input power, and P_o is the light output power. It should be noted that the calculation of Z_t from Eqn. (1.29) is applicable only when the VCSEL operates under continuous-wave (CW) mode. The thermal resistance can also be numerically estimated using FEM techniques in programs like COMSOL^{TM} when CW operation is not feasible.

From just these few parameters we see that all equations responsible for controlling the device performance are interlinked with one another. Therefore, careful considerations are necessary when optimizing a design.

1.2. III-nitride material system

Group III-nitrides are ideal for the fabrication of optoelectronic devices. Not only are they direct bandgap materials, which are the most efficient for radiative recombination, their bandgaps are wide enough to span across the entire visible range of the spectrum and can reach up to the deep-UV. Bandgap tuning also allows access to the infra-red spectral regions. Most arsenide, phosphide, and antimonide based systems emit in the red and far infra-red spectral regions with many alloy compositions having indirect bandgaps. Figure 1.4 plots the various material systems as a function of the bandgap energy (and wavelength) vs. the alloy lattice constant. It can also be seen that the crystal structure of the nitride systems (whether zinc-blende or wurtzite) allows sufficient flexibility in terms of the lattice constant to suit the required applications.

This section will cover the unique material properties of group III-nitrides that influence the design of GaN-based VCSELs.

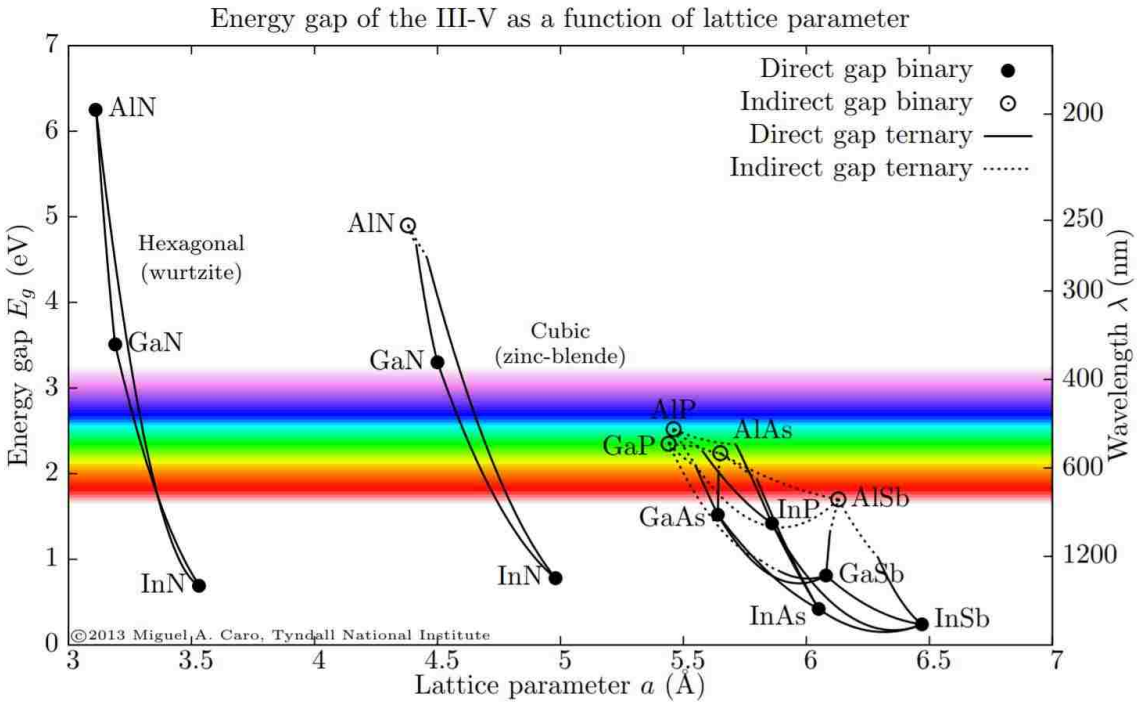

Figure 1.4. Common semiconductor materials plotted as a function of bandgap energy and wavelength vs. lattice constant. The solid and the hollow points are direct and indirect bandgap binary compound, respectively. The lines connecting the binary compounds represent the ternary compounds with the solid indicating direct bandgap and the dashed lines indicating the indirect bandgap. Reprinted from [15].

1.2.1. Wurtzite crystal orientations

Nitrides are predominantly grown in the hexagonal (wurtzite) crystal structure, although a metastable cubic (zinc-blende) structure can also be grown under certain conditions. As such, this thesis will only consider the growth of hexagonal GaN. In the hexagonal structure, each Ga atom is surrounded by four N atoms in a tetrahedral orientation, and vice versa. As a result, the alternating parallel planes along the (0001) direction are either heavily Ga-polar or N-polar, causing a strong dipole in the III-V bond [16]. This gives rise to spontaneous polarization (P_{sp}) across the lattice, particularly on the polar *c*-plane. Figure 1.5 shows the schematics of various crystal planes in the wurtzite structure characterized by the inclination angles (θ) relative to the basal *c*-plane [0001]. The inclination angle is from the Miller indices of an (*hkl*) plane using [17]

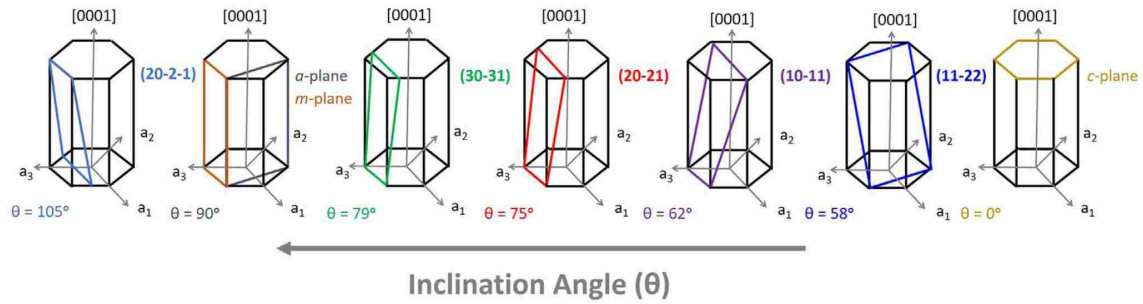

Figure 1.5. Schematics of selected crystal planes in a wurtzite GaN lattice characterized by different inclination angles (θ). Reprinted from [18], with permission from John Wiley and Sons.

$$\theta = cos^{-1}\left(\frac{\sqrt{3}al}{\sqrt{4c^2(h^2+k^2+hk)+3a^2l^2}}\right). \tag{1.31}$$

where a and c are the in-plane and out-of-plane lattice parameters, respectively. The spontaneous polarization is lowered in the asymmetric crystal planes ($0^o < \theta < 90^o$ and $90^o < \theta < 180^o$) where the ratio of total number of N atoms to Ga atoms approaches unity. These planes are called the semipolar planes. In the nonpolar plane (m-plane), where the total number of N and Ga atoms are equal, the spontaneous polarization is completely removed. As we will see in the following sections, built-in polarization has detrimental effects on the device performance and the nonpolar orientation which eliminates the polarization-related electric fields is preferred for GaN-based VCSEL applications.

1.2.2. Strain and polarization

Apart from the spontaneous polarization P_{sp}, the strain in GaN epilayer (tensile in AlGaN or compressive in InGaN) adds another component of internal polarization called piezoelectric polarization (P_{pz}) [19,20]. The direction of P_{pz} is typically in the opposite direction to P_{sp}, with the strength depending profoundly on the alloy material composition. The piezoelectric polarization can be quantified using the strain tensor in a spherical coordinate system [21]. Figure 1.6 plots the total polarization for InGaN/GaN and

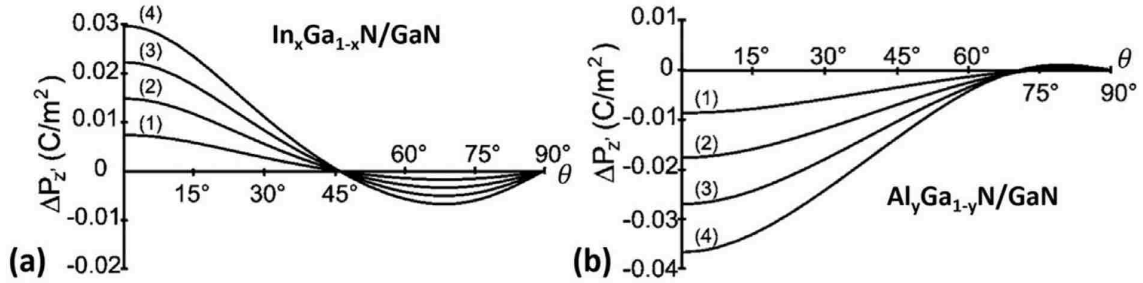

Figure 1.6. Piezoeletric polarization as a function of inclination angle (θ) with respect to *c*-plane for (a) $In_xGa_{1-x}N/GaN$ and (b) $Al_yGa_{1-y}N/GaN$ with compositions: x = (1) 0.05, (2) 0.1, (3) 0.15, (4) 0.2, and y = (1) 0.1, (2) 0.2, (3) 0.3, and (4) 0.4. Reprinted from [21], with the permission of AIP Publishing.

AlGaN/GaN QWs with different composition of In and Al as a function of the inclination angle with respect to *c*-plane. In the nonpolar planes when θ = 90º, the polarization is zero regardless of the alloy composition. However, for the polar planes when θ = 0º, polarization has a strong dependence on the alloy content for both InGaN and AlGaN. InGaN layers are used to form the QWs in the active region and AlGaN with relatively high Al content is used to form the electron-blocking layers (EBL) in the VCSEL epilayers. Hence, it is beneficial to utilize this polarization cancelling property of the nonpolar orientation.

1.2.3. Wavefunction overlap

Figure 1.6 can be misleading as one can assume that the polarization related electric fields have disappeared in *m*-plane where in reality they are simply reoriented in the plane of the QWs. This is depicted in Fig. 1.7 (a) which shows the band diagram of an InGaN/GaN QW on *c*-plane (0001) and *m*-plane $(10\bar{1}0)$ with field directions, surface charges, and the crystallographic phases. The polarized electric field in the *c*-plane QWs gives rise to a phenomenon called Quantum Confined Stark Effect (QCSE). QCSE causes

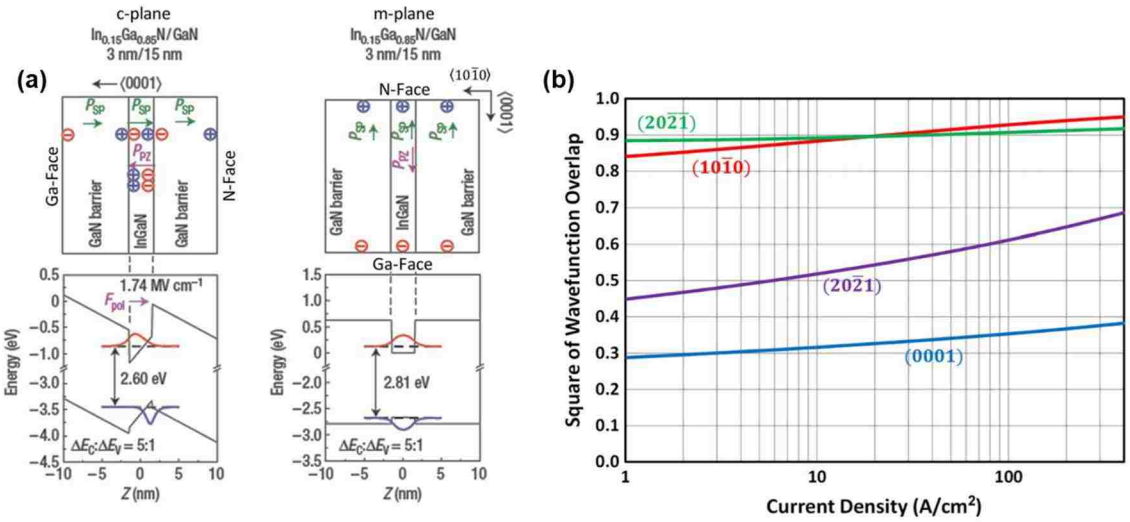

Figure 1.7 (a) [Top] Schematic the direction of polarization fields and the surface charges positions for *c*-plane and *m*-plane QWs. [Bottom] Corresponding band structures for the *c*-plane and *m*-plane QWs. (b) Simulation of the wavefunction overlap for *c*-plane (0001), *m*-plane $(10\bar{1}0)$, and semipolar plane $(20\bar{2}1)(20\bar{2}\bar{1})$ QWs vs. current density. Reprinted with permission from [7,19].

the band-bending in the QWs resulting in the spatial separation of the electron and hole wavefunctions. The reduced overlap integral between the wavefunctions decreases the overall radiative recombination rate [9] in the QWs, which in turn lowers the internal quantum efficiency. In contrast, the bands in *m*-plane remain flat resulting in a near perfect overlap of the wavefunctions. Square of the wavefunction overlap vs. the current density is plotted in Fig. 1.7 (b) for the polar *c*-plane, nonpolar *m*-planes, and two semipolar planes. QCSE also lowers the transition energy in the *c*-plane compared to *m*-plane QWs [7]. The nonpolar orientation mitigates the adverse effects of QCSE, offering wavelength-stable emissions with increasing current injection [19,22].

1.2.4. Gain and anisotropic emission

The in-plane asymmetry which arises from the increase in crystal inclination angle toward *m*-plane results in an anisotropic strain in the QWs [23,24]. The biaxial strain defines the band structure in k-space and exhibit anisotropic characteristics in the valence

band. Figure 1.8 (a) shows the valence band structures for *c*-plane and *m*-plane in two k-space orientations $k_x^{|}$ and $k_y^{|}$. The topmost A1 and B1 subbands contribute the most for carrier recombination and will be the basis of the discussion. Here, the isotropic strain on *c*-plane causes the bands to be symmetrical about the Γ-point and contrarily, the anisotropic strain causes asymmetric bands on *m*-plane. In *m*-plane, the increase in the band curvature towards $k_y^{|}$ (parallel to the *a*-direction on *m*-plane) leads to a reduction in the effective average hole mass [25,26]. The quasi-Fermi level separation increases as a consequence of the reduced hole mass which results in high material gain in *m*-plane. This characteristic property of the nonpolar plane has been thoroughly researched and is well established within the III-nitride community [27–31].

An important parameter to note is the position of the Γ-point in energy scale. The top part of Fig. 1.8 (b) plots the Γ-point energy and the separation in the A1 and B1 subbands ($\Delta E_{A1/B1}$) with inclination angle. The energy level of the subbands are lowest in *m*-plane implying a larger bandgap hence a shorter emission wavelength is to be expected (Section 1.2.3). Furthermore, the increase in $\Delta E_{A1/B1}$ mean that both A1 and B1 are separated further apart in energy for which emission from the topmost A1 subband will dominate over the lower B1 subband. Now, the bottom part of Fig. 1.8 (b) shows the increase in polarization of the transition matrix element $|M|^2$ for the A1 and B1 subbands going from *c*-plane to *m*-plane. The transition matrix element essentially defines the transition strength (probability) for a given valence subband, meaning a high value is favorable for radiative recombination [24]. There is no polarization behavior present in *c*-plane whereas for *m*-plane each subband is completely polarized. Emission from the A1 subband is polarized parallel to the *a*-direction ($y^{|}$) while the B1 subband is polarized parallel to the *c*-direction

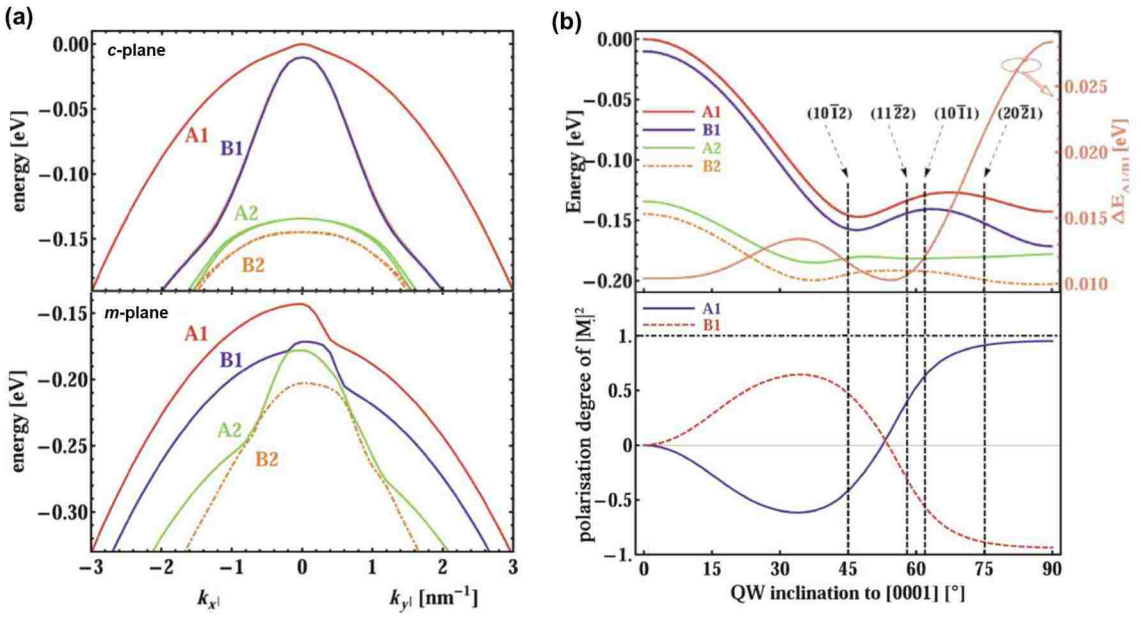

Figure 1.8 (a) The valence band structure for *c*-plane and *m*-plane in k-space. (b) [Top] Development of A1, B1, A2, and B2 valence subbands at the Γ-point vs. QW inclination, also showing the energy separation of the top two subbands. [Bottom] Polarization ratio of the transition matrix elements vs. inclination angle. P_m=1 represents total $y^|$-polarization and P_m=-1 corresponds to total $x^|$ polarization. Reprinted by permission from John Wiley and Sons [24].

($x^|$) [29,32]. Again, since A1 will contribute more toward the total emission compared to B1, stimulated emission from *m*-plane will always be polarized in the *a*-direction with a high polarization ratios. It is worth mentioning that emission from *c*-plane lasers would also be polarized, but the lack of gain anisotropy (circular symmetric valence bands) in *c*-plane would result in random polarizations from device-to-device. In contrast, the in-plane gain anisotropy in *m*-plane will allow polarization-pinned emissions in the *a*-direction for all devices.

1.3. GaN-based VCSEL applications

Now that we have established the working principles and the material characteristics of III-nitride VCSELs, this section will state some of the potential applications for GaN-based VCSELs. It should be noted that most of the mentioned applications are future

technologies as GaN-based VCSELs are still in early developmental stages. Looking at the current industrial trend in mature GaAs and InP-based VCSELs, a huge untapped market exists when GaN-based VCSELs become commercially viable. There may be many more uses of III-nitride VCSELs beyond the potential applications mentioned below.

1.3.1. Lighting and display technology

Notably the biggest driving force behind the development of III-nitride VCSELs is the market for laser illumination and display technologies. With their normal to surface design and the ability to reach peak efficiencies at much higher current densities, VCSELs are

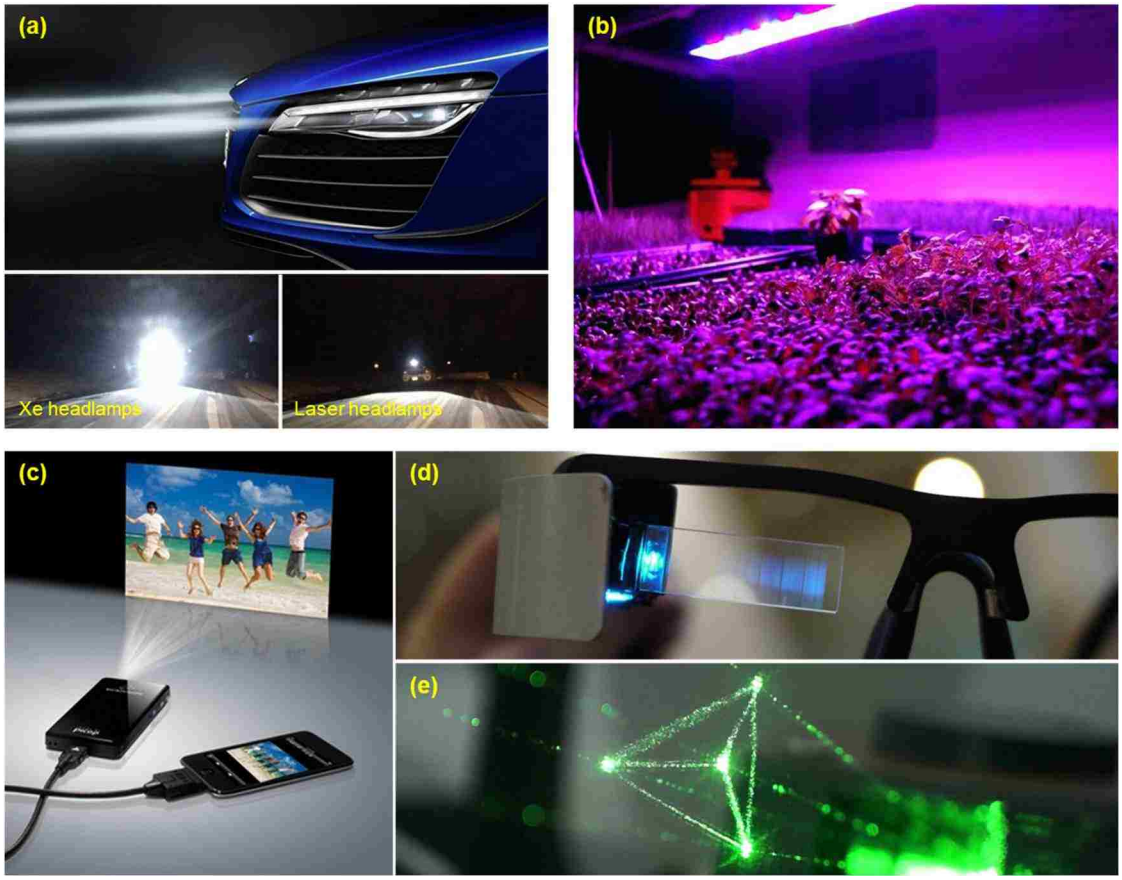

Figure 1.9. VCSEL lighting and display applications. (a) Laser-based lighting being applied to the automobile industry showing reduced glare in laser headlamps as opposed to Xe headlamps. (b) Directional lighting for indoor vertical plant growth. (c) Portable projection systems, (d) Wearable near-eye display screens, and (d) Free-space 3-dimensional holographic projection. [source: Google images]

ideal for integrating to the existing LED infrastructure [33–35]. Examples of lighting applications like laser-based car headlamps and industrial plant growth lighting would benefit from the directionality and the beam steering capabilities of VCSEL arrays. The cost of production per device would significantly be reduced as well in high density arrays. The ability to tune the emission wavelengths make III-nitrides very attractive for display applications as well [36]. Their small form factor would consume less input power and improve battery life, making them suitable candidates for applications like pico-projectors, wearable electronics (near-eye displays), and holographic projections screens.

1.3.2. Visible light communications

In addition to white lighting sources where the III-nitride devices are illuminated through a yellow phosphor [37], VCSELs can also be useful in visible light communication (VLC) which is a component of light-fidelity (LiFi) data transmission. This technology emerged from the ever-growing demand for bandwidth with the current RF wireless resources becoming exhausted day-by-day [38]. The visible spectrum in theory would expand the bandwidth to accommodate future consumer devices. Though LEDs are leading in the field of VLC, the frequency response is significantly limited by long carrier lifetimes associated with the spontaneous emission process [39–42]. Much higher modulation

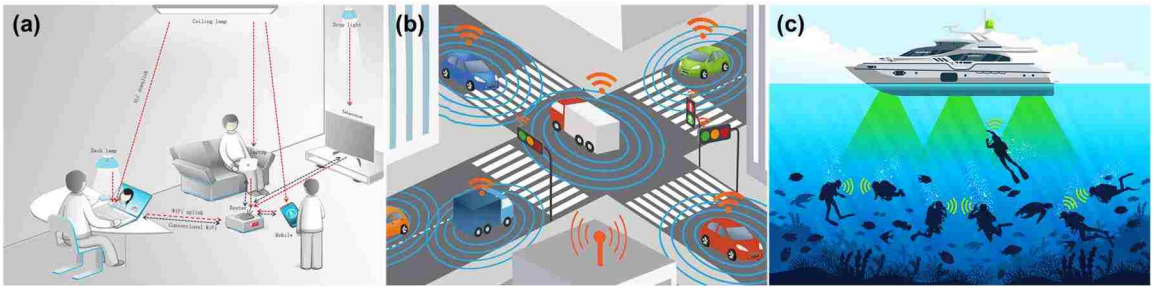

Figure 1.10. Applications of VLC (or LiFi) in (a) indoor, (b) vehicular, and (c) under-water communications. [source: Google images]

bandwidths can be achieved with small active volume VCSELs which can be applied to indoor LiFi systems as well as car-to-car or car-to-environment communications. Similarly, line-of-sight submarine communication is possible since minimal optical loss is incurred by wavelengths around 470 nm and 504 nm under water. Thus, applications in military and deep-sea exploration are linked to GaN-based VCSELs [43].

1.3.3. High-resolution printing

In 2003, Fuji Xerox launched the first VCSEL-based laser printer which used a 2-D 8×4 array of single-mode 780 nm VCSELs. This greatly improved the printer resolution (2400 dpi) and the printing speed (12.5 ppm) in addition to lowered power consumption due to high wall-plug efficiency devices [44–46]. Likewise, even higher printing resolutions can be achieved utilizing GaN-based VCSELs due to the smaller diffraction spot sizes. Additionally, full color printing can be obtained by combining blue and green VCSELs in conjunction to the existing red VCSELs [47,48].

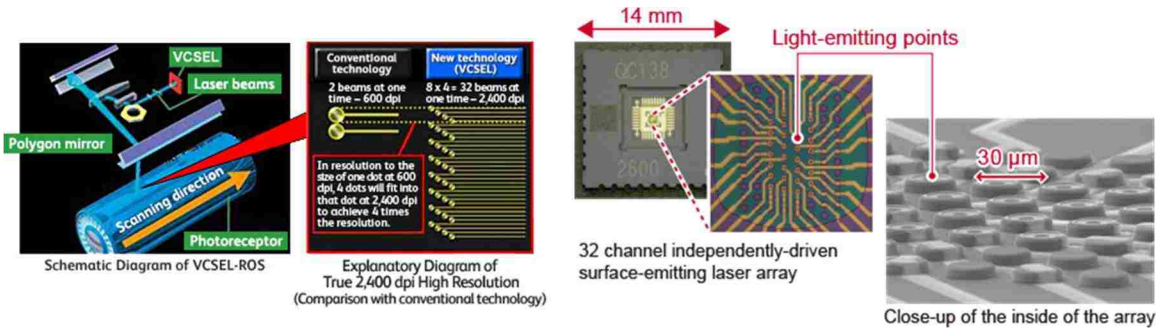

Figure 1.11. VCSELs used in high-resolution printing showing significant improvement in resolution using VCSEL arrays. [source: Fuji Xerox]

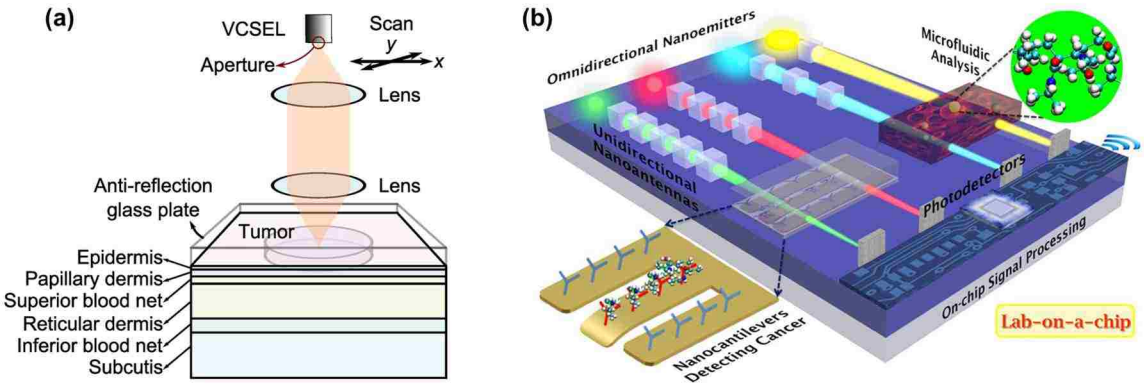

Figure 1.12 (a) VCSEL-based Doppler flowmetry used to quantify tissue perfusion [49]. (b) Multi-wavelength lab-on-chip for probing biochemical tags [50]. [source: Google images]

1.3.4. Sensing and medical applications

Biosensing for medical applications is another important area where GaN-based VCSELs are advantageous for detecting proteins, DNA, antibodies, enzymes, etc. using multi-wavelength fluorescence probing [50]. High-resolution multi-site photo-stimulation of neurons is possible with VCSEL arrays, replacing the more invasive electrical stimulations techniques [51]. GaN-based VCSELs have even been successfully applied in applications for early detection and treatment of different forms of cancer without the need for biopsy [52–54]. The medical field can be the driving influence behind the development of III-nitride VCSELs by the industry.

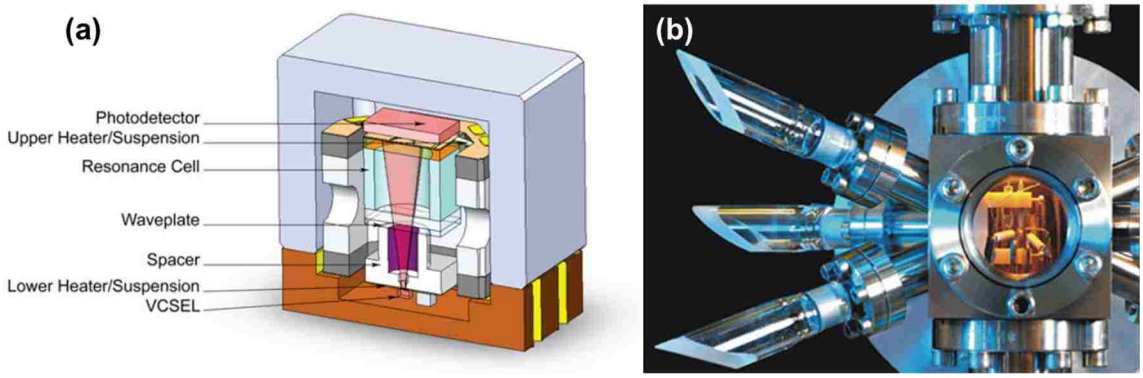

Figure 1.13 (a) Cross-sectional schematic of a chip-scale atomic clock [55]. (b) An ion trap used to study optical frequency standards under low magnetic conditions [56]. [source: Google images]

1.3.5. Miniature atomic clocks

Atomic clocks are highly precise time keepers which are essential for navigation systems used in satellites, space crafts, and defense applications [57,58]. Chip-scale atomic clocks, therefore, need to be miniaturized to reduce weight and lower power consumption. Optical atomic clocks can be integrated into circuit boards unlike the RF-based atomic clocks that are much larger in size. Optical atomic clocks work by the VCSEL excitation of a trapped ion (preferably Yb^+, Sr^+ or Ca^+ for GaN emissions), where the atomic transition is detected as a highly precise time counter [59–61]. Furthermore, the single-longitudinal mode polarization-pinned emission of nonpolar GaN-based VCSELs is imperative to the stability of the instrument.

1.4. VCSEL design considerations

As discussed at the beginning of the chapter, designing a well performing GaN-based VCSEL mandates trade-offs between the optical, electrical, and mechanical properties of the material. Out of all the components in a VCSEL, the bottom DBR is the most crucial in terms of a compromising balance. An ideal DBR should have a high mirror reflectance with wide stopbands to accommodate the gain spectrum and/or growth and process variations. The DBR should be electrically and thermally conductive to facilitate ease of fabrication and proper heat dissipation. The DBR must also be mechanically stable to avoid defect generation and simple growth on existing substrates.

Researchers have developed creative and complex techniques to address the issues faced in the III-nitride VCSEL DBRs. Figure 1.14 depicts a plot of all the electrically injected VCSEL demonstrations from the past 10 years operating under: continuous-wave

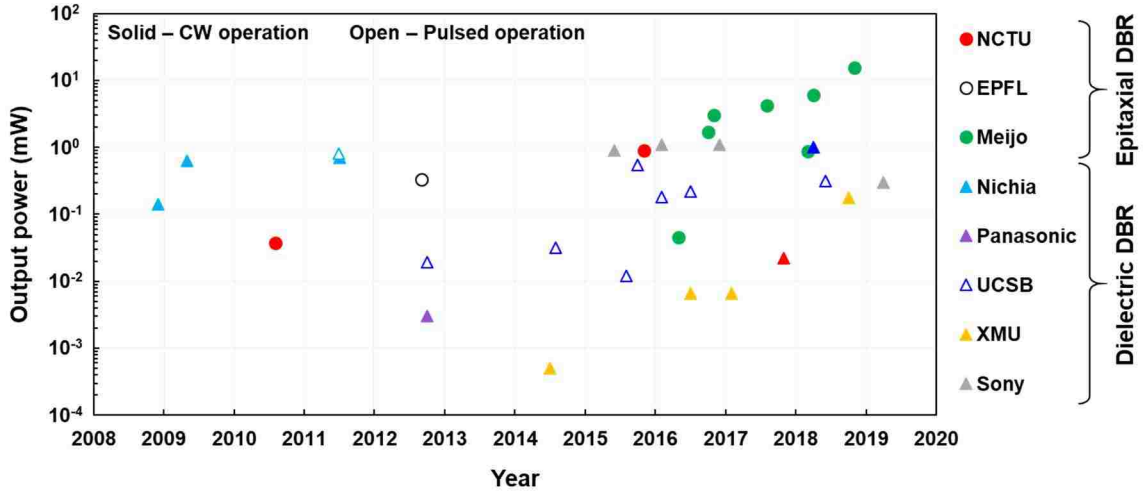

Figure 1.14. Chart showing the history of all electrically injected GaN-based VCSELs with epitaxial [62–71] and dielectric bottom DBRs [72–93].

(CW) [solid] or pulsed [open]. The plot also shows the two primary ways groups have applied the bottom DBR, where they are either epitaxially [circle] grown in metal-organic chemical vapor deposition (MOCVD) or dielectric [triangle] depositions involving some form of flip-chip/overgrowth techniques. Generally, the top mirror is always a dielectric DBR due to the poor conductivity and high absorption loss in the p-type nitrides [94–97], making the VCSEL either a hybrid structure or a double dielectric structure (Fig. 1.15).

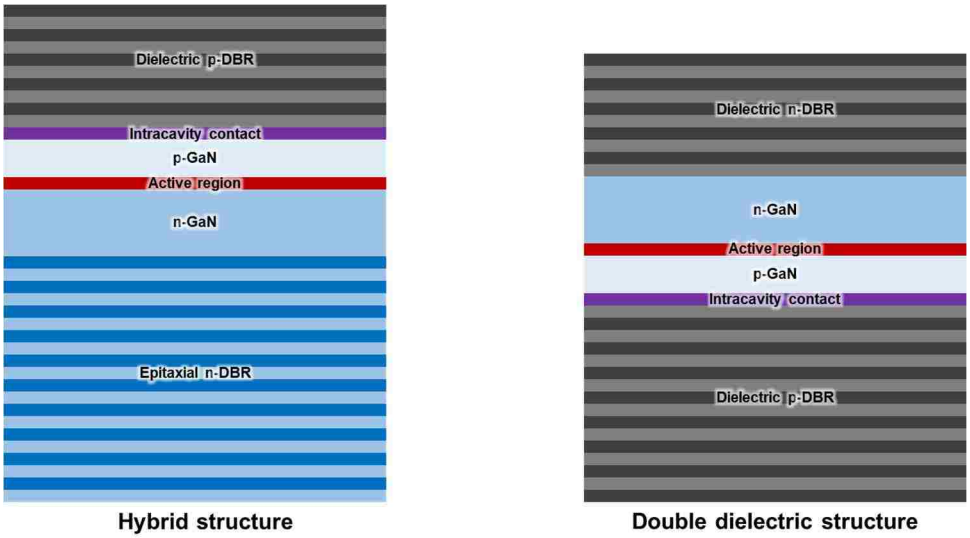

Figure 1.15. Schematic representation of a VCSEL with hybrid structure with bottom epitaxial DBR (left) and a double dielectric flip-chip structure with bottom dielectric DBR (right).

1.4.1. Hybrid structure with epitaxial DBRs

In Fig. 1.14 we see that some of the earlier hybrid design VCSELs by NCTU involved DBRs comprising of AlN/GaN [62,64]. With the refractive index between AlN and GaN being only ~0.3 [98], more than 25 DBR pairs were required to obtain high mirror reflectance. The layers were also under tremendous tensile strain from the large difference in thermal expansion coefficient and lattice mismatch (AlN/GaN - $4.2\times10^{-6}/5.59\times10^{-6}$ /K & 3.112/3.191 Å) [98,99]. This led to the formation of crack and defects in the DBR stack which ultimately reduced the mirror quality. Figure 1.16 shows a cross-section TEM image of an AlN/GaN DBR with superlattices incorporated after every 5 pairs. Besides the threading dislocations, the presence of V-defects can be clearly observed in the high-magnification TEM image in Fig. 1.16 (b). Although the superlattices help in preventing cracks by strain compensation, the V-defects are an inherent property of *c*-plane orientation on which most GaN-based VCSELs are grown. The local variation in layer thicknesses introduce interface non-uniformity leading to substantial scattering loss [100].

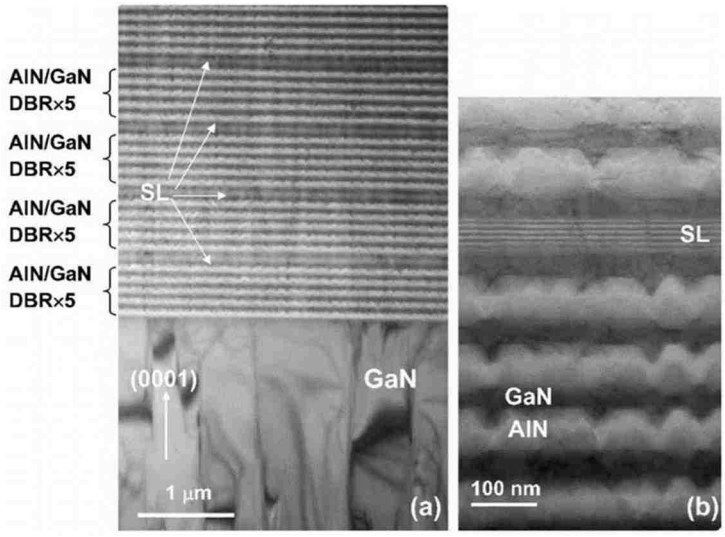

Figure 1.16 (a) Low-magnification cross-sectional TEM image of a AlN/GaN DBR. (b) High-magnification TEM image showing the superlattice layer within the DBR. Reprinted, with permission, from [100].

In contrast, DBRs grown using AlInN/GaN are more appropriate as $Al_{0.82}In_{0.18}N$ is lattice matched to GaN. This material combination has become somewhat of a gold standard in recent years after the demonstration of several electrically injected VCSELs with impressive results. A research group at Meijo University in collaboration with Stanley Electric Co. recently demonstrated a *c*-plane GaN-based VCSEL with a record high output power of 15.7 mW [71]! Up until this point, almost all electrically injected GaN-based VCSELs had output powers limited to ~1 mW. The DBRs could also be made electrically conductive using bulk or modulation doping, however, in most cases it is avoided to minimize free-carrier absorption by using intracavity contacts.

Nevertheless, $Al_{0.82}In_{0.18}N$/GaN DBRs are notoriously difficult to grow in MOCVD because of the growth parameters involved with AlN [101] and InN [102] as an alloy and only a few groups have successfully shown a working VCSEL using this material combination. The optimal growth temperature and pressure required for AlN and InN are remarkably different, with 1300°C and ~75 torrs for AlN, and 700°C and ~750 torr for InN. This makes maintaining the composition of Al- to In- in AlInN very tricky. Additionally, the low growth temperature (~800°C) used to grow the $Al_{0.82}In_{0.18}N$ would yield poor quality material due to the surface migration of the Al-species. A low growth rate of 0.2 μm/hr [103] is often used to counter this problem, but it is not practical since the growth of the $Al_{0.82}In_{0.18}N$/GaN DBRs require more than 40 pairs. Researchers at Meijo Uni. and Stanley Co. have optimized the growth of AlInN where they can now grow at a rate of 0.5 μm/hr, which is still very low, requiring about 12 hours to grow a DBR with reflectance greater than 99% [66–68].

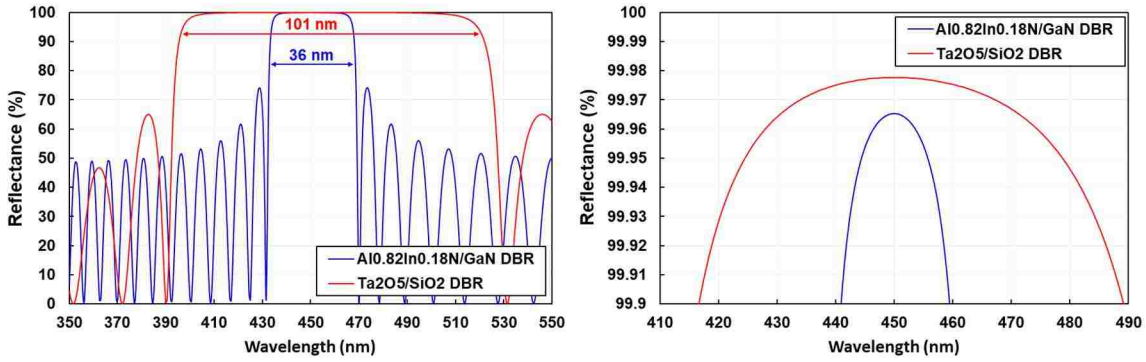

Figure 1.17. 1-D TMM simulation of the DBR spectra of a 42 pair $Al_{0.82}In_{0.18}N$/GaN epitaxial DBR and a 12 pair Ta_2O_5/GaN dielectric DBR design at 450 nm [11,104,105].

Another issue associated with epitaxial DBRs is the small refractive index difference between the ¼-λ layers. From Eqn. (1.16) and Eqn. (1.18) in Section 1.1.4, we see that the refractive index difference between the two layers of the DBR determine the DBR stopband and the number of pairs determine the total peak reflectance at the Bragg (design) wavelength. Figure 1.17 shows the TMM simulation of the DBR spectra with a Bragg wavelength of 450 nm for a 42 pair epitaxial $Al_{0.82}In_{0.18}N$/GaN DBR and a 12 pair dielectric Ta_2O_5/SiO_2 DBR. Even with 42 pairs, the peak reflectance for the epitaxial DBR is less than the dielectric DBR. The lower reflectance can be overcome by further increasing the number of pairs at the expense of increased growth time, but the stopband is still fundamentally narrower in $Al_{0.82}In_{0.18}N$/GaN compared to Ta_2O_5/SiO_2 due to the lower refractive index contrast in epitaxial DBRs. This may become as problem during the fabrication of the VCSEL as there is little room for error beyond the Bragg wavelength with sufficiently high reflectance when unintentional detuning of the cavity resonance occurs.

1.4.2. Double dielectric structure with dielectric DBRs

To circumvent the difficulties faced in epitaxial DBRs, several research groups have adopted the double dielectric (bottom dielectric) VCSEL design [72–93]. Apart from the large refractive index and wide stopband (Fig 1.12), dielectric DBRs are attractive for their relatively ease of deposition and the wide assortment of different materials available. Table 1.1 lists some of the commonly used materials in DBRs and their corresponding refractive indices at 450 nm. Deposition techniques such as plasma-enhanced chemical vapor deposition (PECVD), magnetron sputtering systems, ion-beam deposition (IBD), e-beam evaporation, etc. can be used to deposit the DBRs which are much more reproducible and cost effective than a MOCVD or MBE grown epitaxial DBR. There is no concern for defects or cracks in the films deposited using these techniques because they are amorphous/polycrystalline in nature. However, in systems where plasma damage can occur during deposition, care must be taken to avoid direct exposure of the epilayer surface to the high energy plasma.

The limitation of the double dielectric DBR design is that it adds significant complexity during the fabrication steps of the VCSEL. In order to get access to the backside of the cavity to deposit the n-side DBR, substrate removal and flip-chip processes like bonding, laser lift-off (LLO) [72,77,87,88], chemical mechanical polishing (CMP) [73,75,84,91], and photoelectrochemical etching (PEC) [78,83,89,90] are necessary. Often, these back-end processing techniques result in a reduced device yield. Problems concerning device transfer, cavity length control, and/or damage during fabrication can easily occur. Similarly, regrowth techniques like epitaxial lateral overgrowth (ELO) [79,82,86] mandate precise knowledge of the growth conditions to control the growth morphology. In ELO,

Table 1.1 List of some dielectric materials used in DBRs [106].

Dielectric	Refractive index
SiO_2	1.4656
Si_3N_4	2.0786
Ta_2O_5	2.1610
Nb_2O_5	2.4516
HfO_2	2.1420
ZrO_2	2.1966
TiO_2	2.6143

the crystals grow out space between DBRs and coalesce with an adjacent crystal. This is particularly difficult to achieve due to the low lateral-to-vertical growth rate ratio. Hence, the cavity control is poor due to a thick bulk layer between the DBR and the MQWs. Furthermore, the coalescence can cause grain boundaries and difference in vertical profiles inside the cavity. Figure 1.18 shows scanning electron microscope (SEM) images of some of the difficulties faced during the fabrication of a flip-chip VCSEL and the ELO on *m*-plane substrates.

With dielectric DBRs being electrically insulating, current injection into the aperture of the VCSEL becomes problematic. Conventionally, intracavity current spreading layers are used to inject carriers into the VCSEL. This allows metal contact pads to be located away from the aperture (preventing light blocking) and the carriers are transported into the MQWs through an underlying spreading layer. For the p-side, the intracavity contact is usually a transparent conductive oxide such as indium-tin oxide (ITO) [74,88] or a nitride-based tunnel junction (TJ) [81,89], whereas for the n-side they are the highly doped bulk GaN layers. The current spreading layers tend to be highly absorbing due to the amorphous nature (for ITO) or the high doping concentrations (for n-GaN) which is why they should be place at the standing-wave nulls when designing the cavity. Intracavity spreading layers will be further discussed in detail in Chapter 4.

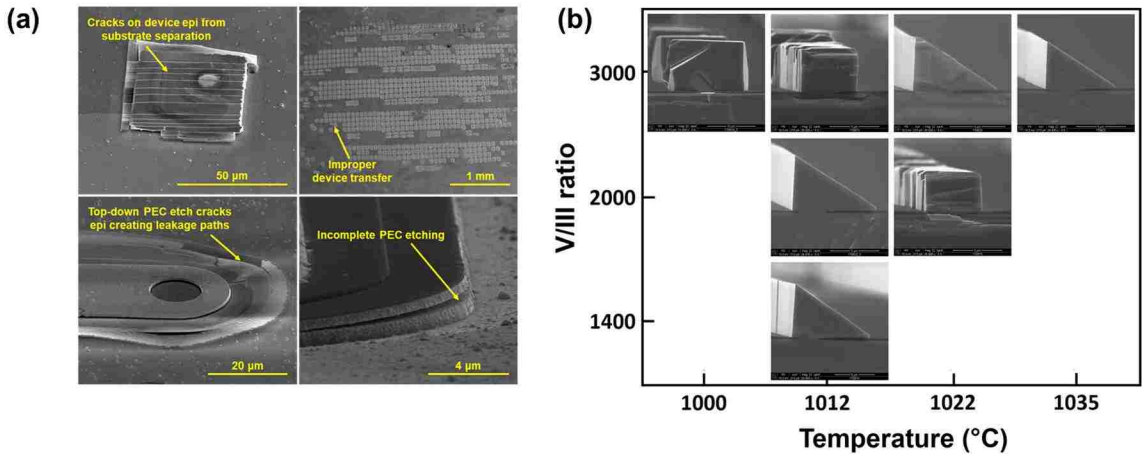

Figure 1.18. SEM images showing (a) processing issues during flip-chip using PEC etching resulting in poor device yield, and (b) non-uniform morphology evolution during ELO regrowth with various V/III ratio and temperature combinations [107,108].

The thermal conductivity of the dielectric DBRs is of great concern. Compared to the III-nitride alloys used in epitaxial DBRs which have thermal conductivities around ~100 W/mK, dielectric materials are very thermally insulating with thermal conductivity values ranging between 1-15 W/mK [109–113]. Additionally, enhanced phonon scattering by the thermal boundary resistance at the interfaces of stacked layers further worsens the thermal conductivity [114]. Therefore, a dielectric DBR below the active region essentially traps the generated heat from dissipating into the heatsink/substrate. Self-heating in VCSELs is related to early roll-over of the output power at high current densities. Non-radiative carrier losses become dominant at elevated temperatures in addition to the misalignment of the peak gain wavelength with the cavity resonance wavelength. This is evident in Fig. 1.14, where the output powers of dielectric DBR VCSELs are limited to less than 1 mW whereas epitaxial DBRs extended beyond 15 mW. To gain insight into the heat dissipation characteristics of a double dielectric DBR VCSEL, Fig. 1.19 shows the steady-state FEM

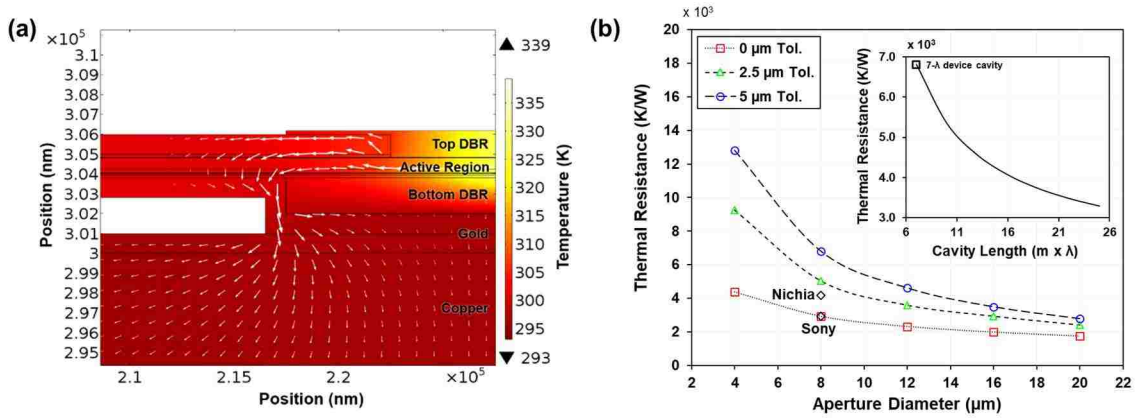

Figure 1.19. Temperature profile and heat propagation (proportional arrows) model from COMSOL™. (b) Thermal resistance vs. aperture diameter for different alignment tolerances. Data points are also shown for two reports of CW GaN-based VCSELs [74,82]. (Inset) Thermal resistance vs. cavity length for an 8 µm diameter aperture design.

2-D thermal analysis of flip-chip VCSELs [115]. From Fig. 1.19 (a), we see that the heat generated in the active region is primarily conducted laterally through the epilayers and into a bottleneck arising from the thin p-side metal connecting to the heatsink. Vertical heat transfer is almost completely obstructed in this device configuration. Ideally, the metal layer should be placed close to the active region without obstructing the cavity resonance so that the heat travels a shorter lateral distance toward the heat sink. This is shown in Fig. 1.19 (b), where reducing the contact lithography alignment tolerances and bringing the metal layers closer reduces the thermal resistance of the device by a factor of three. Although lowering the alignment tolerance provides a relatively simple technique to reduce thermal resistance, self-aligned or 0-µm-tolerance lithography poses significant fabrication challenges. Typically, a ~5 µm tolerance can be easily achieved with conventional contact lithography processes, while tolerances below ~1 µm can be achieved only with more expensive projection-based stepper lithography. The inset in Fig. 1.19 (b) shows the effect of the VCSEL cavity length on the thermal resistance. Here, the thermal resistance values similar to self-aligned designs can be obtained on 5 µm tolerances with thicker cavities. A

larger cavity volume enables the heat to disperse throughout the structure rather than being concentrated near the active region. It is no wonder that companies like Sony and Nichia have adopted cavity lengths >20-λ. Nevertheless, the thermal resistance is still significantly higher for flip-chip dielectric DBR design compared to recently reported epitaxial DBR GaN VCSELs (~300 K/W) [71].

1.5. Summary

To summarize this chapter, GaN-based VCSELs emitting in the UV-blue spectral region are key components for potential applications in the consumer market, military, medical field, etc. Although the arsenide and phosphide-based systems have been successfully commercialized in the IR-region, GaN-based VCSELs are still in their infancy and have been the subject of development in recent years. The III-nitride material system poses unique and difficult challenges, none more so than the lack of high quality epitaxial DBRs that can be reproduced relatively easily at lower costs. Researchers and companies have relied on dielectric DBRs with complex device architectures to counter this problem. A solution combining the advantages of both epitaxial and dielectric bottom DBRs while mitigating the shortcomings is still missing.

This thesis presents an alternative approach where air-voids are selectively incorporated in GaN layers to obtain a lattice-matched DBR with high reflectance. Thus, high refractive index contrast can be achieved requiring fewer pairs to form the DBR. This method also simplifies the device architecture while avoiding the tedious growth monitoring. Air-gap DBRs have traditionally been applied to LEDs to enhance extraction as they operate at lower current densities [116–120]. VCSELs, on the other hand, operate at much higher current densities and the non-conducting nature of air-gap DBRs is

unfavorable to the structural rigidity and heat extraction of the device. Hence, there are no reports of an electrically injected VCSEL employing full air-gap DBRs.

We utilize a compromising solution of using porous layers (nanopores) to replace the air-gaps in the DBRs. Losing some of the index contrast between the layers allows tunability of the electrical, optical, and mechanical properties of the DBR. Chapter 2 will explain the details regarding the growth and fabrication of the nanoporous DBR. Then in Chapter 3, an optically pumped hybrid cavity nonpolar VCSEL is demonstrated with a nanoporous bottom DBR and a dielectric top DBR. There are only two other groups who have successfully demonstrated optically pumped nanoporous VCSELs, with no reports of any electrically injected devices as of yet. Finally, in Chapter 4, we show the first ever electrically injected demonstration of a nonpolar GaN-based VCSEL using nanoporous bottom DBRs and investigate the device characteristics. To conclude, Chapter 5 will mention some of the design related issues to further improve the device performance.

2. The Nanoporous DBR

Nanoporous GaN DBRs cleverly allow the formation of high reflectance mirrors with wide stopband while eliminating the need for strained or lattice-matched ternary alloys in the DBR. The DBR structure consists of alternating layers of doped and undoped GaN followed by a processing step of anodic electrochemical (EC) etching to selectively "porosifies" the n-doped GaN. The nanoporous layers have a reduced effective refractive index relative to the surrounding non-porous (bulk) GaN layers. Figure 2.1 shows the refractive index, stress, and resistivity plot of some candidates for DBR material pairs. Here we see that arsenide material systems have decent index differences with virtually no mismatched stresses and very low resistivities. Similarly, dielectric DBR pairs can have very high index contrast with no stress but are non-conductive. AlN-based ternary materials with GaN, despite having modest index contrast, suffer from tremendous stress and an increasing degree of resistivity with increasing Al composition. The nanoporous DBR approach has relatively high refractive index contrast with the same material lattice constant of GaN while enabling tunability of the Bragg wavelength in the DBR.

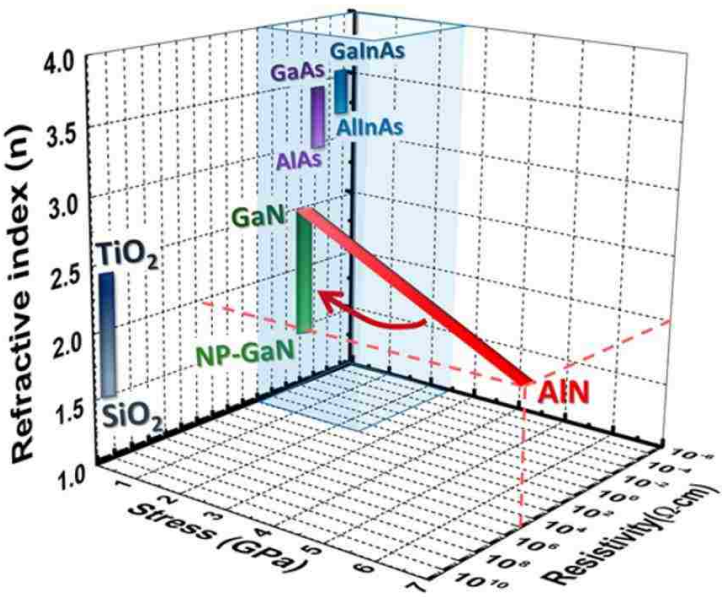

Figure 2.1. 3-D parameter plot showing the stress (GPa), resistivity (Ω-cm), and refractive index of some DBR material pairs. Reprinted with permission from [121], Copyright 2015 American Chemical Society.

The majority of past work using nanoporous GaN for DBRs particularly focused on the polar *c*-plane materials and devices [121–132]. Among these, instrumental work on was performed by Prof. Jung Han's research group at Yale university [121,131–136], where they investigated the dynamics of pore generation and pore evolution in *c*-plane GaN grown on sapphire substrates. Figure 2.2 (a) illustrates the map of pore size and pore density as a function of the layer doping concentration and applied bias during EC etching. For given doping concentrations, we see that porosification occurs only at a narrow window of the applied bias. Below this bias there is no etching, and beyond this bias the doped layer is completely etched away (electro-polishing). This complete removal of the layer is useful for applications where thin-film or membrane separation is essential [137]. As a general trend, the pore sizes increase with applied bias due to enhanced etching, but the density of pores is determined by the doping concentration. Thus, a highly doped layer will electropolish earlier compared to a low doped layer with respect to the EC etch bias.

Note that the porosity, which is defined as the ratio of the volume of air to the total layer volume, can be identical for a layer with highly dense small pores to a layer with less densely packed larger pores. The group at Yale reports a peak reflectance of >99.5% and stopband of 70 nm. An SEM image of a nanoporous DBR on *c*-plane with peak 70% porosity with ~30 nm pore size is shown in Fig. 2.2 (b). A distinct interface can be observed between undoped GaN layers and the porous doped layers which is essential to minimize scattering loss. Scattering loss is a common concern whenever randomly arranged porous layers are involved. The randomness may cause the beam profile to change after reflection. This was qualitatively examined by the far-field pattern of a 652 nm red laser after reflection from the nanoporous DBRs. The results are depicted in Fig 2.2 (c). It was observed that the initial laser spot before reflection was nearly identical to the spot after reflection from a reference Al mirror and the nanoporous DBR. Negligible variations in the speckle patterns indicated the preservation of the phase coherence. Furthermore, it was shown that the DBRs with the same layer thicknesses could be adjusted up to 30 nm simply by altering the layer porosity [Fig. 2.2(d)]. This adjustability is a very useful aspect of nanoporous DBRs should the cavity mode be misaligned with the gain peak. Finally, the electrical property of the DBR was also verified using Hall measurements shown in Fig. 2.2(e). Obviously, as the porosity increases the doping concentration is expected to fall as more and more material is etched away. However, what is interesting is that the carrier mobility remains fairly constant around 80 $cm^2V^{-1}s^{-1}$ yielding a low resistivity of ~0.04 Ω-cm even at 55% porosity. These attributes make the nanoporous DBR very attractive for VCSEL applications.

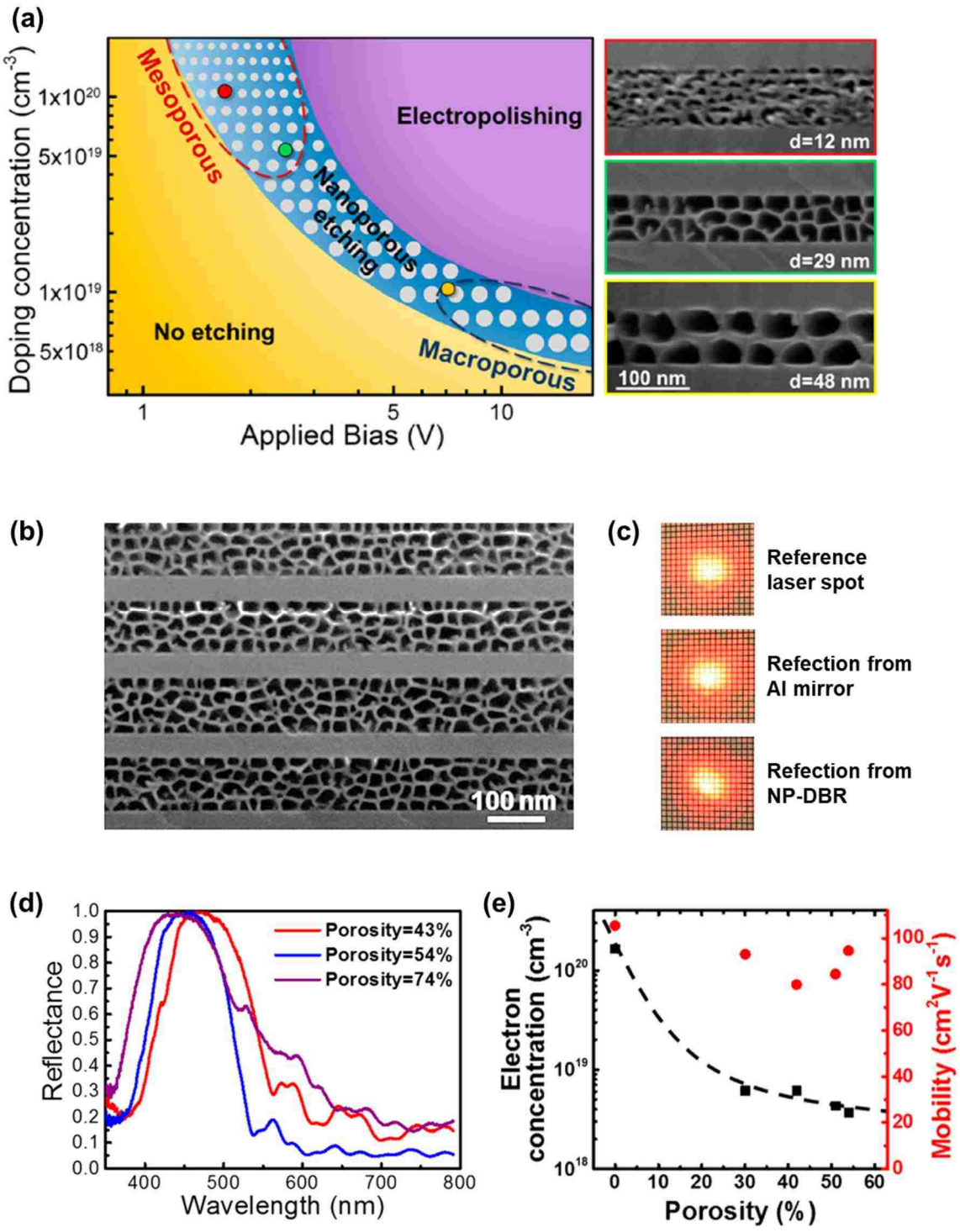

Figure 2.2 (a) Map of pore size and density as function of the doping concentration and EC bias voltage. SEM images show the pore characteristics of the corresponding data point red, green, and yellow. (b) SEM image of a *c*-plane nanoporous DBR. (c) Photographs of far-field patterns of a laser before and after reflection from a reference Al mirror and the DBR. (d) Reflectance spectra showing the Bragg wavelength tunability by varying the layer porosity. (e) Plot showing the electron concentration and mobility vs. the layer porosity. Reprinted with permission from [121], Copyright 2015 American Chemical Society.

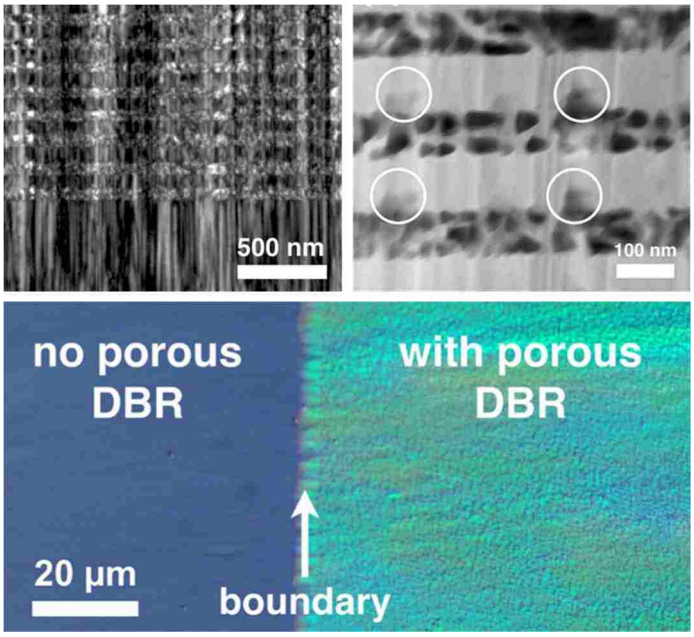

Figure 2.3. (Top) TEM images showing threading dislocations propagating into the nanoporous DBR. The white circles indicate the locations where EC etch proceeded vertically toward the bulk layers. (Bottom) Nomarski microscope image showing EC etch fronts and a non-uniform surface reflectance. Reprinted with permission from [138].

A single demonstration of a nanoporous DBRs using nonpolar *a*-plane GaN heteroepitaxially grown on *r*-plane sapphire has been reported by a group at the University of Cambridge [138]. Here, the EC etch was simplified by removing the fabrication steps and applying a one-step process. Instead, the etch is initiated using defect assisted etching where the etchant seeps in through the defects and etches laterally in the n-doped GaN layers. This process reduces the etch time substantially to only 30 minutes. The cross-section transmission electron microscope (TEM) images in Fig. 2.3 reveal a high density of dislocations (~4×10^{9} cm^{-2}) originating from the non-native substrate and going through the DBR. Although, the defects are vital for EC etching in this case, the growth of a VCSEL cavity on top of such high defect density DBR would severely degrade the device with leakage paths and non-radiative recombination centers. Moreover, the threading dislocations also cause the etch to proceed vertically in some locations porosifying the non-

porous layers. This would result in local variations in the cavity length across the sample with regions of different Bragg wavelengths. The non-uniformity in the wavelength can be observed in the Nomarski optical microscope image in Fig. 2.3 where the colors change from yellow to green and blue. It also shows a rather rough surface morphology which may contribute to scattering loss.

Most GaN-based lasers are produced homoepitaxially on GaN substrates for high reliability. This chapter will demonstrate the nanoporous DBRs on free-standing nonpolar *m*-plane GaN substrates. The effects of the n-type doping concentrations and the EC bias voltages will be studied for the *m*-plane which exhibited anisotropic etch properties. The mirror reflectance will also be characterized in addition to verifying the polarization sustainability of the nanoporous DBRs upon reflection. The *m*-plane nonpolar orientation is of interest because of its improved per-pass gain, lower transparency carrier density, and in-plane gain anisotropy for highly polarization-pinned emission along the *a*-direction (See Chapter 1 Section 1.2).

2.1. MOCVD growth of *m*-plane GaN

Before explaining the details regarding the EC porosification process, one must understand the growth of *m*-plane GaN in MOCVD. This section will highlight the growth considerations unique to *m*-plane GaN. All growths were performed on free-standing *m*-plane GaN substrates manufactured by Mitsubishi Chemical Corporation (MCC) [139,140]. Due to the unavailability of native nonpolar substrates for mass production, initially sapphire substrates are used to grow in *c*-plane using hydride-vapor phase epitaxy (HVPE). HVPE offers a very high growth rate of GaN in the *c*-direction allowing bulk layer to be grown up to ~6 mm. The bulk GaN layer is then diced and

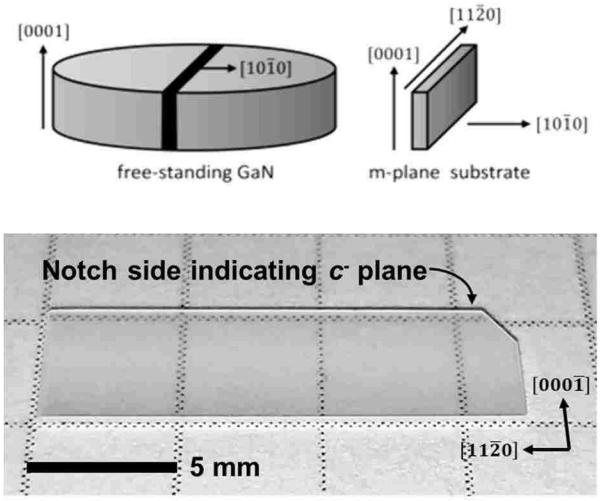

Figure 2.4. (Top) Schematic of *m*-plane substrates processed from HVPE grown bulk GaN. (Bottom) Photograph of an *m*-plane substrate with a miscut of 0.95° in the $[000\bar{1}]$ direction purchased from Mitsubishi Chemical Corporation.

polished along the *m*-plane to fabricate the *m*-plane substrate, where the thickness of the HVPE grown bulk GaN becomes the width of the *m*-plane GaN substrates. Thus, *m*-plane substrates are relatively small and more expensive compared to conventional *c*-plane GaN substrates due to low yield. Figure 2.4 shows a schematic of the preparation of *m*-plane substrates from HVPE grown bulk GaN and a photograph of a full *m*-plane substrate measuring only 5 mm by 17 mm by 0.3 mm. The substrates have a nominal n-type doping concentration ~10^{17} cm^{-3} and low defect density of ~10^{5} cm^{-2}.

Growing on *m*-plane substrates using MOCVD comes with its own set of challenges for which typical *c*-plane growth conditions cannot easily be translated. Early work on on-axis (no miscut) *m*-plane epitaxy showed evidence of the sample surface covered by pyramidal hillocks [141–143]. Naturally, a rough surface is not preferred from a VCSEL stand point, but the crystal facets in the hillocks cause variations in the growth rate, alloy composition, and doping concentration. The pyramidal hillocks were proven to originate from the spiral propagation of a threading dislocation with a screw component [144].

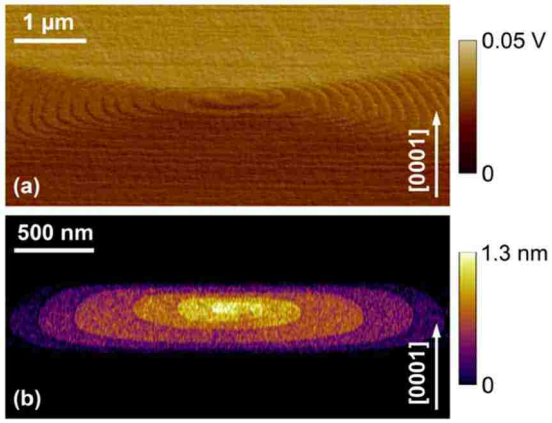

Figure 2.5 (a) Large-area low-resolution AFM image of the pyramidal hillock. (b) Small-area high-resolution AFM height image near the apex of a pyramidal hillock. Reprinted from [145].

Figure 2.5 illustrates a low and high-resolution atomic force microscopy (AFM) image of a pyramidal hillock showing the apex and the spiral atomic steps forming the pyramid.

To suppress the formation of the pyramidal hillocks and improve surface roughness, growth of *m*-plane GaN on misoriented (miscut) substrates with H_2 and N_2 as carrier gases was investigated [145]. The results are shown in the microscope images in Fig. 2.6. Firstly, the on-axis substrates exhibited a high density of hillocks irrespective of the carrier gas. With increasing miscut angle from the c^- plane in H_2 ambient, the pyramidal hillocks consistently appeared with dimensions ranging from 100 to 500 µm. Also, the surface morphology showed severe faceting and undulations beyond a misorientation angle 0.5°. In contrast, for films grown in N_2 ambience, the size of pyramidal hillocks dramatically reduced to around 5 to 25 µm. At the same time, around miscut angles ~1°, the hillocks disappeared completely, and optically smooth surfaces could be obtained. The improvement in surface morphology can be attributed to the decomposition rate of GaN in MOCVD [146]. Under typical growth temperature and pressure, the decomposition rate is almost ten times lower for films grown in N_2 ambient than in H_2 ambient. This stabilizes the surface morphology reducing the striations seen in Fig 2.6.

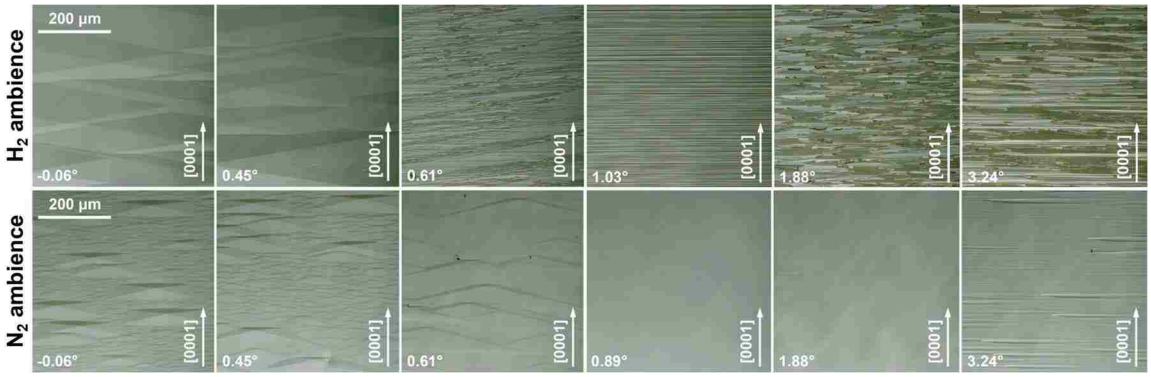

Figure 2.6. Optical micrographs GaN films grown on substrates with different miscut angles from the *c*- plane under H_2 and N_2 ambience (carrier gas). Reprinted from [145].

All epilayer growths mentioned in this thesis were carried out on a Veeco P-75 turbo-disc MOCVD reactor. The chemicals and gases used in the system are: ammonia (NH_3) as the N precursor in the growth of all III-nitrides; trimethylgallium (TMG) as the Ga precursor when high growth rates are required for bulk layers (~2 µm/hr); triethylgallium (TEG) as another Ga precursor with much slower growth rate (~1.5 nm/min) used during the growth of QWs; trimethyindium (TMI) as In precursor used for the growth of InGaN QWs; trimethyaluminum (TMA) as Al precursor for the growth of AlGaN EBL; bis(cyclopentadienyl) magnesium (Cp_2Mg) used for p-type doping with Mg; and lastly silane (SiH_4) which is used for n-type doping with Si in III-nitrides. The growth temperature and pressure for bulk GaN is ~960°C and 500 torr, respectively. The V/III ratio used in the system is typically >2000 and can change depending on the layer. Note that these are ballpark numbers based on the current conditioning and are subject to change according to the health of the reactor. The growth rate is monitored in-situ through a viewport using a compensated pyrometry setup. Compared to the 2-inch *c*-plane GaN substrates, *m*-plane substrates are much smaller in size (Fig. 2.4), hence the pyrometry measurement of the growth rate may be inaccurate as the laser can miss hitting the sample as it rotates at high rpm. As we will see in Chapter 4, thickness calibration using PEC and

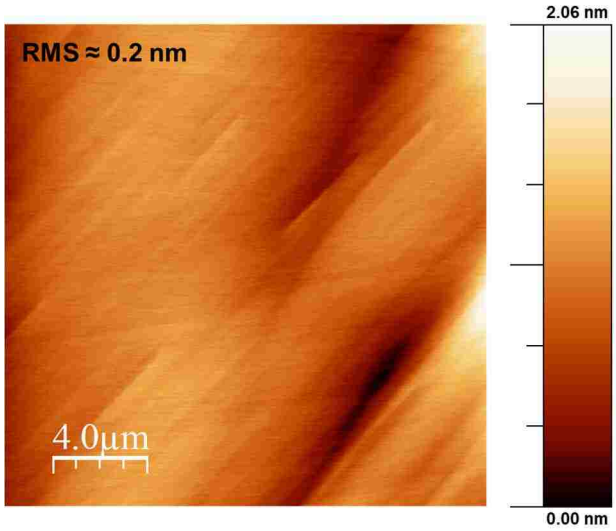

Figure 2.7. AFM scan of *m*-plane GaN on a 20 μm×20 μm window showing an RMS surface roughness of ~0.2 nm.

EC etching will be developed. Details regarding the growth of the MQWs, EBL, and contact layer will be also provided in the following chapters (See Appendix A.1 for growth recipe log).

Before the growth of the VCSEL structure, a 3 μm thick n-GaN template is grown to ensure a smooth surface morphology with Si concentration ~7×10^{17} cm^{-3}. The surface roughness was measured to have an RMS value of ~0.2 nm on a 20 μm-by-20 μm AFM scan (Fig. 2.7). Most reports of surface roughness use smaller scan windows (1 μm-by-1 μm or 5 μm-by-5 μm) which often underestimates the measurement ignoring features that are spaced far apart.

2.2. Electrochemical etching

This section will explain the mechanism and electrochemistry involved in the anodic porosification process, followed by the etching characteristics of *m*-plane n-GaN under different acids, doping concentrations, and bias voltages.

2.2.1. EC etching mechanism

The EC etch process (porosification) can be simplified to a sequential repetition of four important steps: (i) hole generation at the semiconductor/etchant interface, (ii) oxidation of the exposed semiconductor surface, (iii) oxide dissolution by the etchant, and (iv) transport of reaction byproducts away from the surface [147]. Out of these four steps, the hole generation step is what mainly governs the porosification process, where the holes are created by either Zener tunneling or avalanche breakdown. The dominating mechanism is determined by the doping concentration of the n-type GaN layer. For a highly doped layer, the space charge region (SCR) in GaN is very narrow such that electrons can easily tunnel through from the valence band to the conduction band. Meanwhile, the SCR is comparatively wider for low doped layers. In the presence of an electric field, electrons accelerate and gain sufficient kinetic energy to knock-off bound electrons thereby causing an avalanche breakdown. This phenomenon is illustrated in Fig. 2.8. The upward band bending at the GaN/acid interface accumulates holes at the surface and reacts to form etch pits with the doping concentration controlling the density of etch pits. The curvature of the etch pits causes shallower SCR at the apex, further enhancing hole generation by Zener tunneling [148]. Eventually the pits size widens to form the pores and adjacent SCRs overlap to create a large region that is completely devoid of carriers. Overlapping of nearby SCRs is important to inhibit the lateral etching of the pore sidewalls [134,136]. Now, the holes accumulate only near the tip of the pores, forcing the pores to propagate in a singular direction perpendicular to the initial exposed semiconductor surface. Note that if the etch pits were further apart, as in the case of low doped layers, random lateral branching of pores is to be expected due to the absence of SCR overlap [133].

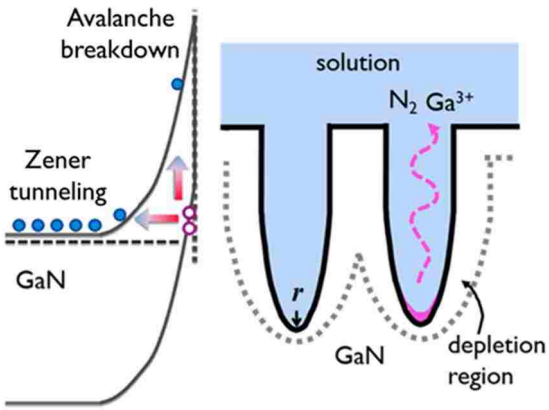

Figure 2.8. Band diagram of a GaN/etchant interface showing hole generation mechanisms. It also shows a schematic of pore formation through the tips and removal of etch byproducts. Adapted with permission from [147], Copyright 2014 American Chemical Society.

At the tip of the pores (GaN/acid interface), the holes participate in an oxidation reaction to form $Ga(OH)_3$ which dissolves in the acid to form Ga^{3+} ions that is swept away in the solution. Water oxidation also occur with H_2 gas bubbling off from the cathode. The reaction equations are as follows:

$$[\text{GaN oxidation}] \quad GaN + 3H_2O + 3h^+ \rightarrow Ga(OH)_3 + \tfrac{1}{2}N_2 + 3H^+ \tag{2.1}$$

$$[Ga(OH)_3 \text{ dissolution}] \quad Ga(OH)_3 + 3H^+ \rightarrow Ga^{3+} + 3H_2O \tag{2.2}$$

$$[H_2O \text{ oxidation}] \quad H_2O + 2h^+ \rightarrow \tfrac{1}{2}O_2 + 2H^+ \tag{2.3}$$

2.2.2. Dopant and bias study on m-plane GaN

To study the behavior of nanopores in *m*-plane GaN, the samples first need to be processed to expose the buried n-doped layer. The samples are first coated with a thin layer (~100 nm) of SiO_2 to prevent roughening or defect-selective etching from the top surface. Next, mesas of 50-µm-wide stripe mesas with a separation of 8 µm were patterned by standard contact lithography and etched using reactive ion etching (RIE) and inductively coupled plasma (ICP) through the SiO_2 and the epilayers down to the GaN template. The

etch exposes the sidewalls of the n-doped GaN layers, creating access for the solution during the EC etching. Then an indium contact is soldered at the corner of the sample (anode) which is submerged in the etchant (acids) and stirred, ensuring that the contact does not touch the solution. A separate platinum wire mesh is also placed alongside the sample in the solution as the cathode, and the two electrodes are connected to a DC source. No other component of the setup (contact clips, cables, etc.) should touch the surface of the etchant. Otherwise, a leakage path will be created, restricting the current flow through the sample but rather etching the setup components and contaminating the solution. The current flowing through the electrolytic cell can be used to monitor the etch progression where a rise in current after an initial drop signifies complete porosification [136]. This current is typically on the order of milliamps which was much smaller than the measurable limit of our ammeter. Instead, the lateral etch rate for a known doping concentration and EC bias voltage was measured to calculate the total time needed complete porosification. Once the etch is complete, the SiO_2 layer was stripped using buffer HF and rinsed in deionized water. Figure 2.9 shows the schematic of a basic EC etch setup and the processing steps used to the fabricate test samples [149].

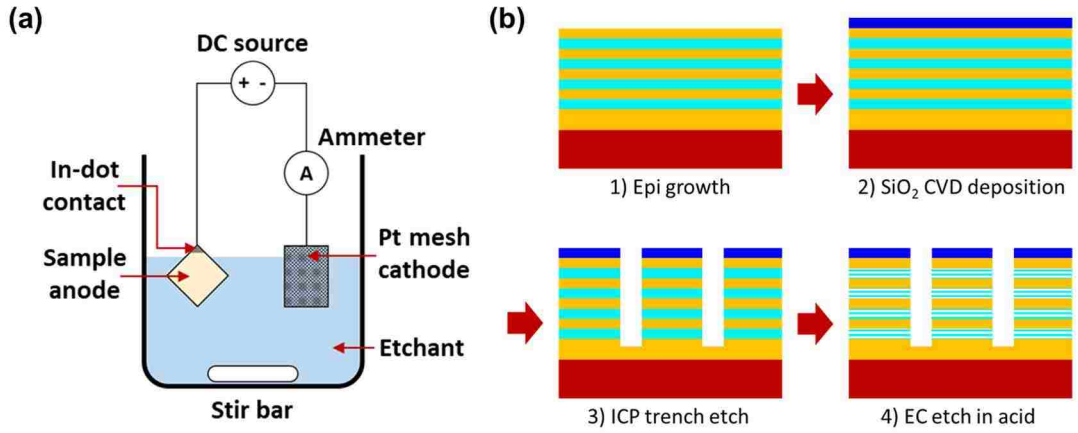

Figure 2.9 (a) Schematic of the EC etch setup. (b) Processing steps showing the fabrication of test *m*-plane samples.

Aspects such as pore size, lateral etch rate, and pore uniformity can heavily depend on the type of acid used as the etchant. The effect of three different acids: 49% HF, 70% HNO_3, and 0.3 M $C_2H_2O_4$, was explored on a sample with a single n-type GaN layer of Si doping concentration ~10^{18} cm^{-3}. The EC etch was performed for 3 hours at a bias voltage of 30 V. The results are shown in the optical microscope and SEM images of Fig. 2.10. Each acid has a unique lateral etch rate with HF being the lowest at 2.1 µm/hr and HNO_3 being the highest at 5.5 µm/hr. The lower etch rate can be explained by the very small surface pores restricting the diffusion of etchant to the pore tips. Both HF and HNO_3 showed regions of non-uniform pore sizes as the etching progressed, evidenced by the color variations in the microscope images. However, oxalic acid yielded better pore uniformity due to the etch almost reaching electropolishing, indicating room for pore size tuning by lowering the bias voltage. Furthermore, etching with HF is very hazardous particularly when one must reach into the container to submerge the sample, and gases given off when using HNO_3 corroded the clips holding the electrodes. From this point onward, all EC etches were performed in 0.3 M oxalic acid.

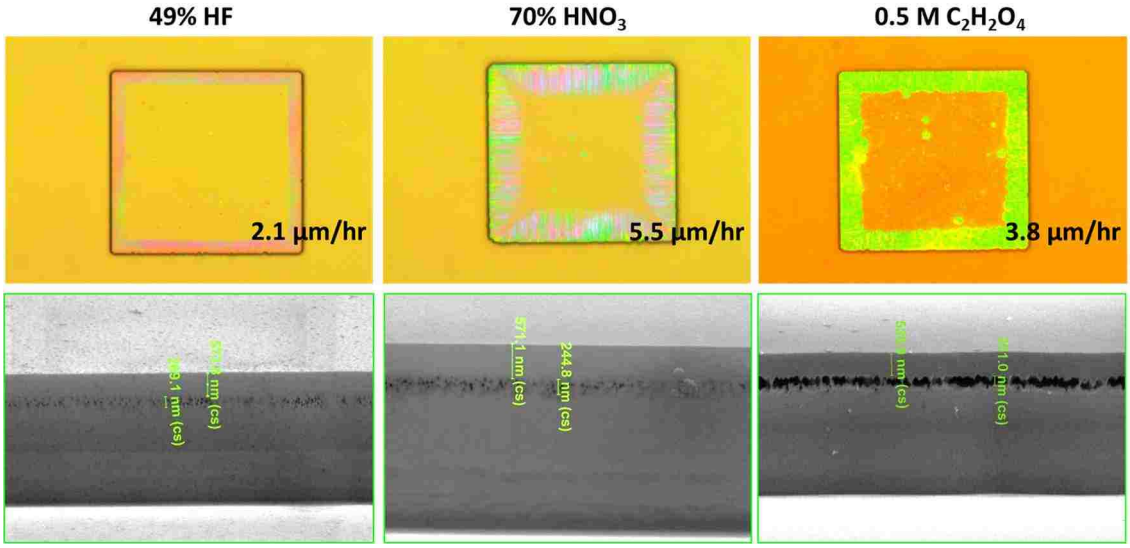

Figure 2.10. EC etch of n-GaN (~10^{18} cm^{-3}) in etchants: HF, HNO_3, and $C_2H_2O_4$.

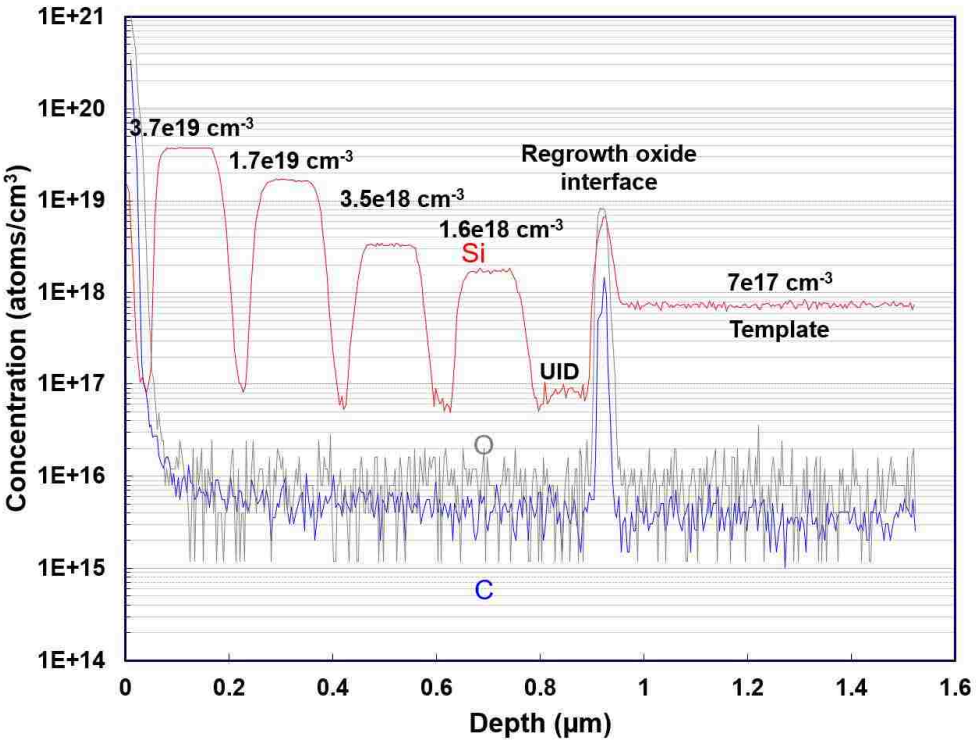

Figure 2.11. SIMS measurement by EAG for determining Si doping level in GaN. Background levels of carbon and oxygen are also shown. The spike in background doping originates from the atmospheric oxidation of template surface before regrowth.

Dependence of pore diameter and density on the layer doping concentration and bias voltage was studied next. A sample was grown consisting of four different n-doped GaN layers, separated by undoped GaN layers. Each layer had a thickness of ~80 nm and the doping concentrations were 1.6×10^{18} cm^{-3}, 3.5×10^{18} cm^{-3}, 1.7×10^{19} cm^{-3}, and 3.7×10^{19} cm^{-3}, as confirmed by secondary ion mass spectroscopy (SIMS) measurement, shown in Fig. 2.11, performed by Evans Analytical Group (EAG). The spike in the carbon and oxygen levels at the interface between the template and regrowth layers is a consequence of atmospheric oxidation from the break in growth. Using the current growth conditions, doping levels higher than the ones stated resulted in non-uniform island growths.

The sample was then cleaved into smaller pieces and each piece was EC etched under a different bias voltage for 3 hours. Figure 2.12 (a) shows the cross-sectional SEM images

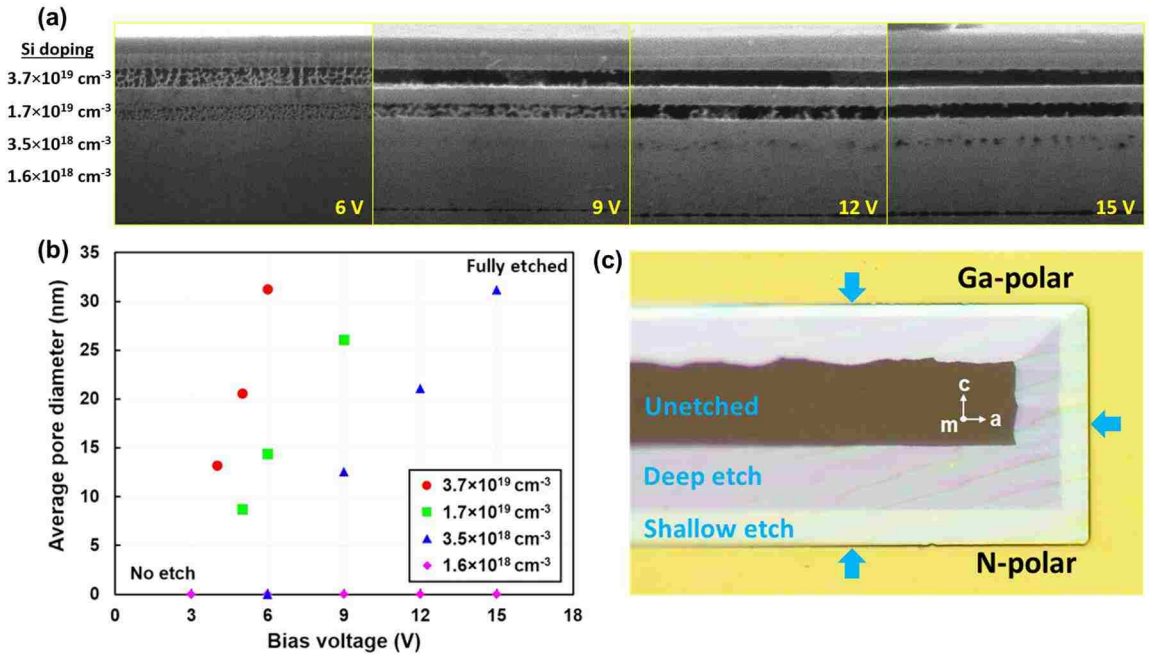

Figure 2.12 (a) Cross-sectional SEM images of a sample with four different layers of Si-doping under four different bias voltages. (b) Average pore diameter vs. EC etch bias voltage for different doping concentrations. (c) Microscope image of 6 V bias sample showing lateral etch depths.

of the samples under four different bias voltages. It was observed that the top two doped layers remained porous until 6 V and 9 V, respectively. The layers were completely etched beyond these voltage limits. The more highly doped layers exhibit higher pore densities, leading to complete etching at lower bias voltages. When the doping level is lowered to 3.5×10^{18} cm^{-3}, the pores slowly emerge with increasing bias at a significantly reduced pore density. The layer doped at 1.6×10^{18} cm^{-3} did not etch under any of the applied bias voltages. The average pore size for each doping level and bias voltage was quantified using the cross-sectional SEM images in Fig. 2.12 (a), where several pore diameters were averaged for each independent layer. The results are plotted in Fig. 2.12 (b). As a general trend for all studied doping levels, the average pore size increases almost linearly with the bias voltage until complete etching occurs [149]. Also, the rate at which the pore size increases with bias voltage [i.e., slope in Fig. 2.12 (b)] reduces with decreasing doping.

This trend is consistent with *c*-plane EC etching of GaN reported in [121,133,135,136]. Note, it is difficult to accurately quantify the pore density from Fig. 2.12 (a) since densely packed pores tend to agglomerate to form less densely packed larger pores at higher biases. The pore density should remain constant for a given doping concentration, irrespective of the EC bias voltage.

Depending on the crystallographic orientation of the exposed sidewall of the mesas, anisotropic lateral etch rates were also observed. The lateral etch depth varied proportionally with the doping concentration. Figure 2.12 (c) shows an optical microscope image of the sample etched under 6 V bias. The arrows indicate the direction of the lateral etch fronts with section labeled "shallow etch" shows the etch depth of the 1.7×10^{19} cm^{-3} doped layer, and the section labeled "deep etch" shows the etch depth of the overlying 3.7×10^{19} cm^{-3} doped layer. Finally, the section labeled "unetched" shows that a section remains where none of the doped layers were etched due to inadequate etch time. The *a*-direction facets exhibit similar etch depths in both directions (not shown), while the *c*-direction facets show different etch depths, with the Ga-face etching slower than the N-face. The anisotropic etch rate of the exposed *c*-facets is attributed to the higher chemical stability of the Ga-face compared to the N-face due to the built-in polarization fields sweeping the holes to the N-face of *m*-plane GaN [150].

2.3. Nonpolar nanoporous DBRs

Now that we have established the porosification characteristics in *m*-plane GaN, we will now move to the design and fabrication of the nanoporous DBR. Knowing the accurate refractive indices of the nanoporous layers is crucial for designing the $\lambda/(4n)$-thickness condition. The effective index of the nanoporous layers can be calculated using a Volume

Average Theory (VAT) [151]. The VAT states that beyond a certain layer thickness, the effective refractive index of a porous volume can be estimated as a function of the porosity, regardless of the pore shape, size, spatial distribution, layer thickness, or the wavelength. This approximation is defined as:

$$n_{por} = [(1-\varphi)n_{GaN}^2 + \varphi n_{air}^2]^{\frac{1}{2}} \tag{2.4}$$

$$\chi = \frac{\pi D}{\lambda_B} \ll 1 \tag{2.5}$$

where, n_{por} is the effective refractive index of the porous GaN layer, φ is the layer porosity, n_{GaN} and n_{air} are the GaN and air refractive indices, respectively. χ is a term called as the scattering factor which is a function of the average pore diameter D and the Bragg wavelength λ_B. The average pore diameter is ~15 nm to 20 nm for 5 V etch bias, and assuming the wavelength of interest is 450 nm, χ is held at ~0.1 in an effort to minimize scattering. The porosity φ is defined as the ratio of air-to-GaN in a surface area assuming the pores propagate in a straight trajectory. Thus, φ can be easily evaluated by digitizing the SEM images in Fig. 2.12 (a) and calculating the ratio of dark pixels to the total number of pixels in the layer [See Appendix A.5 for MATLAB code]. An example of the image digitization program is given in Fig. 2.13 (a), where the layer with Si doping concentration $3.7\text{x}10^{19}$ cm^{-3} etched under 6 V bias is digitized to extract a porosity of ~0.51. The SEM image is first transformed into grayscale followed by a color equalization step, then finally the binary conversion. Using the dispersion data presented in Fig. 2.13 (b) to find n_{GaN} at 450 nm (peak signifying the band-edge emission wavelength of GaN), Eqn. (2.4) can be used to plot the effective refractive index of the porous layers versus the porosity shown in Fig. 2.13 (c). A porosity of 0.51 yields n_{por} of ~1.88. Then using the value of n_{GaN} and

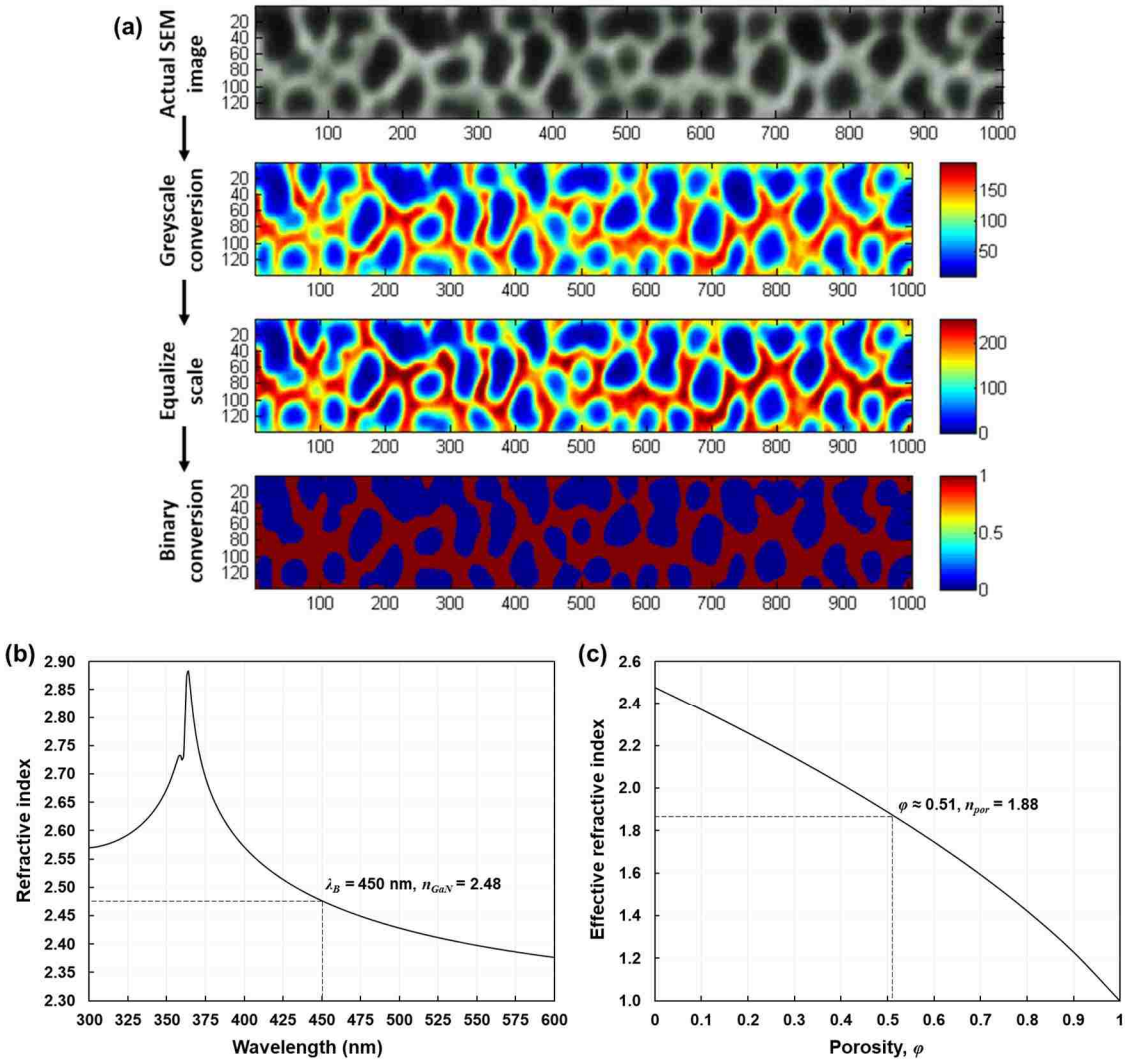

Figure 2.13 (a) Digitization of SEM image to extract the layer porosity. (b) Refractive index dispersion data for GaN [105]. (c) Calculation of the effective refractive index as a function of the porosity.

n_{por} in Eqn. (1.16) and Eqn. (1.17), we can evaluate the number of DBR pairs required to obtain the desired reflectance. From this analysis, it was found that 15 pair would be sufficient for a peak reflectance >99.9%.

To form the DBR, the λ/(4*n*)-thicknesses of the doped and undoped layers must be ~60 nm and ~45 nm, respectively. A DBR sample was then grown with 15 pairs on an *m*-plane template. The mesas stripes were orientated along the *c*-direction to leverage the uniform EC etching across both facets of the sidewall in the *a*-direction. EC etching was

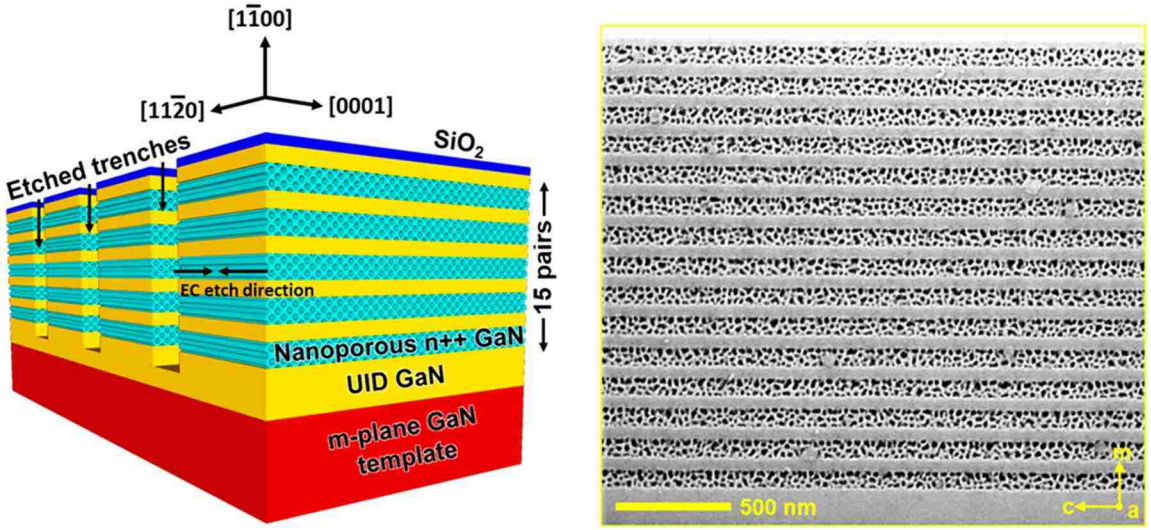

Figure 2.14. Schematic and cross-sectional SEM image of the 15-pair nanoporous m-plane GaN DBR.

then carried out for 5 hours to ensure complete lateral etching across the mesa at biases of 4 V, 5 V, and 6 V in order to vary the degree of porosity. Figure 2.14 shows the schematic and a cross-sectional SEM image of the 15-pair nanoporous *m*-plane GaN DBR etched with a 6 V bias.

2.4. Optical characterization

The optical characterization of the nanoporous DBR will be described in this section. The first part will provide detail on the reflectance measurements and the second part will highlight the polarization sustainability of the nanoporous DBRs.

2.4.1. Reflectance measurement

Reflectance measurements of the fabricated DBRs were carried out using a μ-reflectance setup with a broadband light source at normal incidence. A photograph of the μ-reflectance setup is shown in Fig. 2.15. Light from the broadband source is focused on

the surface of the DBR sample through an objective. The reflected light from the DBR is then transmitted to a spectrometer. Also, a beam splitter allows imaging of the sample surface using a CCD camera. The reflectance spectra are determined from the measured intensity spectra after reflection using,

$$R_{DBR} = \frac{I_{DBR}}{I_{ref}} R_{ref} \tag{2.6}$$

where R_{DBR}, I_{DBR}, R_{ref}, and I_{ref} are the reflectance and the spectrum intensity of the DBR and reference mirror, respectively. A commercially available dielectric mirror with a near

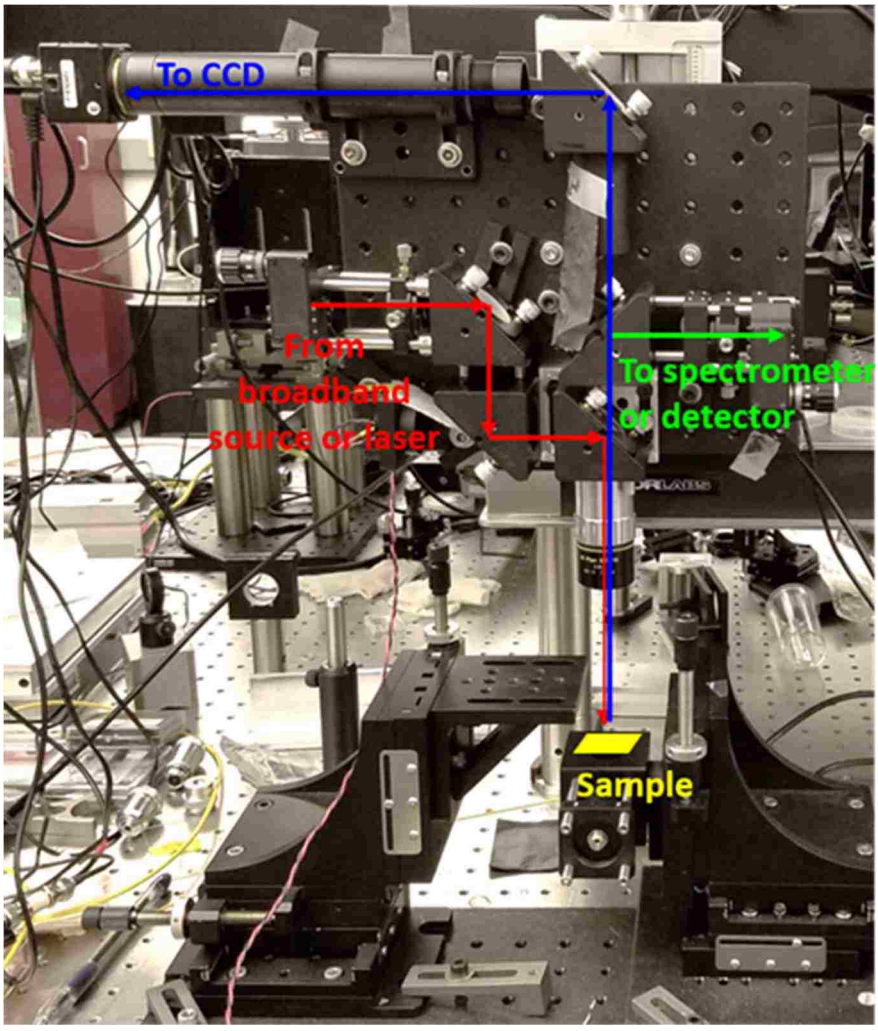

Figure 2.15. Photograph of the μ-reflectance measurement setup at CINT.

unity flat-band reflectance from 300 nm to 600 nm was used as the reference. It is worth mentioning that the true reflectance of a DBR mirror may be different from the measured reflectance. Slight variations in the reference mirror calibration can either underestimate or overestimate the measurement. Ideally, the setup should focus on the mirrors surface as precisely as possible using features or small scratch marks as a guide.

The measured reflectance spectra for DBRs fabricated at the three different bias conditions are shown in Fig. 2.16. The Bragg wavelength redshifts from 450 nm to 520 nm as the applied bias decreases. Furthermore, the DBR stopband width and the peak reflectance also decrease with decreasing bias, with $\Delta\lambda_{stop}$ and R_{DBR} being ~72 nm and 98.67%, ~64 nm and 93.04%, and ~40 nm and 83.52% for the 6 V, 5 V, and 4 V DBRs, respectively. The side SEM images (i) in Fig. 2.16 show that the porosity of the doped layers drops for lower bias, which causes the refractive index difference between the pairs to decrease, resulting in lower $\Delta\lambda_{stop}$ and R_{DBR} and red shifted Bragg wavelength. Cross-section SEM images of the DBRs were digitized and examples of the digitized sections are shown in black/white (GaN/air) in image (ii) of Fig. 2.16. The VAT approximation model was then applied to the digitized images which yielded the index of refraction and porosity for the 4V, 5V, and 6 V samples as 2.10 and 29%, 1.92 and 46%, and 1.86 and 53%, respectively. To verify these numbers, a 1-D semi-empirical TMM simulation was applied to obtain the ideal reflectance spectra for each DBR, using the measured thicknesses of the bulk (SEM) and porous GaN layers and the refractive index of bulk GaN (ellipsometry). The refractive index of the porous layer was used as the fitting parameter, with the starting point being the refractive index obtained from the VAT. Figure 2.16 shows that the calculated plots are in excellent agreement with the measured reflectance spectra. The

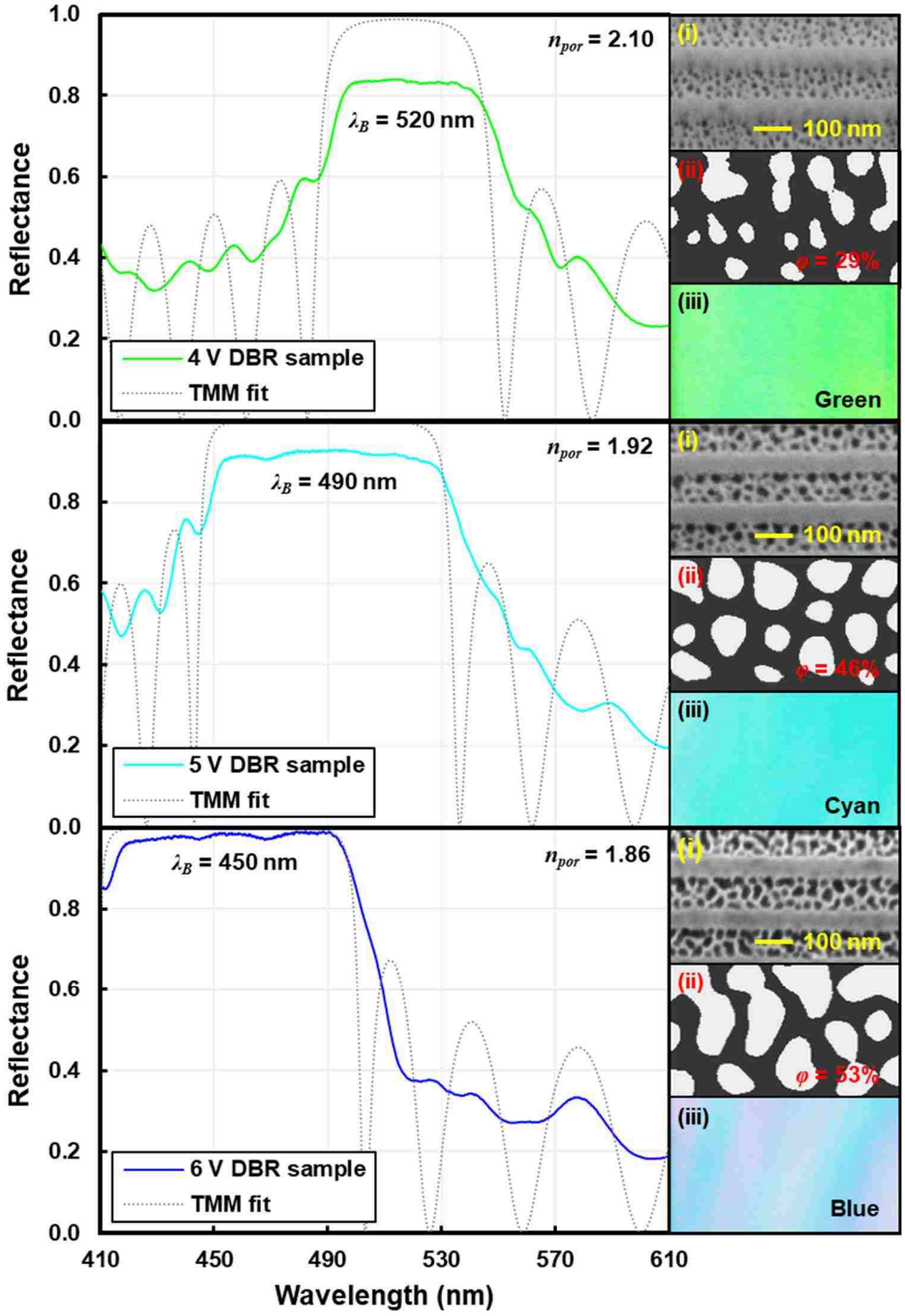

Figure 2.16. Reflectance spectra of the nanoporous DBRs fabricated using three different bias voltages 4 V (green), 5 V (cyan), and 6 V (blue) with TMM fits using VAT (dashed curves). The side images show the (i) magnified SEM cross-section images, (ii) VAT digitized images, and (iii) top-down microscope images of the corresponding DBR samples.

lower peak reflectance of the fittings for the 4 V and 5 V biases is still the subject of investigation but is likely due to the lower porosity in these samples increasing the total free-carrier absorption from doping, which the TMM does not consider. The figure also shows the topographic optical microscope images (iii) of the three DBRs under the broadband source. The non-uniformity in the 6 V sample is from the larger pore sizes agglomerating to form localized regions of higher porosity with a higher refractive index contrast.

2.4.2. Polarization sustainability

In contrast to most conventional VCSELs, where the polarization of the emission is randomly oriented, the emission from nonpolar *m*-plane VCSELs is polarization-pinned in the *a*-direction. Due to the nature of directionality in the pores, the DBRs may exhibit preferential polarization characteristics [152]. Therefore, we investigated if the nanoporous DBRs can maintain the polarization of an incident polarized light source upon reflection. The polarization ratio is given by

$$\rho = \frac{I_{max} - I_{min}}{I_{max} + I_{min}}, \tag{2.7}$$

where I_{max} and I_{min} are the maximum and minimum intensity detected at different polarization angles. To measure ρ, the μ-reflectance setup was modified by replacing the broadband light source with a diode laser emitting with *s*-polarization at 450 nm. A polarizer was also added in front of the detector to analyze the degree of polarization. The normalized intensity with respect to the polarizer angle after reflection is plotted in Fig. 2.17. It was previously proven that dielectric mirrors maintain the polarization after several passes in a cavity. [76,78] Hence, the dielectric reference mirror was used to obtain the

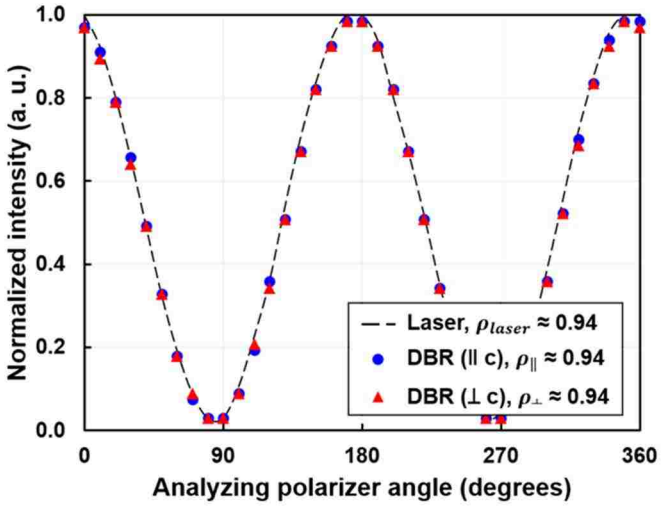

Figure 2.17. Polarization measurement of a laser source before and after reflection of the 6 V DBR sample in two orientations.

polarization ratio of the laser source and system optics, which was ρ_{laser} ~94% after reflection. The initial polarization ratio is not 100% due to a small polarization loss in the beam-splitter component used. The 6 V nanoporous DBRs was then measured at two different orientations, with the laser polarization parallel and perpendicular to the stripe mesa orientation in the *c*-direction (pores aligned in the *a*-direction) to examine if the DBR is isotropic with respect to polarization. Both cases produced polarization ratios ~94% after reflection, suggesting that the polarization of the incident laser is indeed maintained after reflection regardless of the orientation of the EC etch direction.

2.5. Summary

In summary, this chapter explored EC etching in *m*-plane samples, where it was established that the pore diameters depend on the bias voltage while the pore density is determined by the doping concentration of the layer similar to that of *c*-plane. However, the N-polar facet was chemically more reactive than the Ga-polar facet, resulting in a faster lateral etch rates along the *c*+ direction. The VAT was used to extract the porosity and the

effective index of refraction of porous layers fabricated with different bias voltages. Using this, we demonstrated the fabrication of an *m*-plane nanoporous DBR on a free-standing GaN substrate with a peak reflectance more than 98% at 450 nm and a stopband width of 72 nm. Note that there were several instances when the peak mirror reflectance was >99.9%. The ambiguous nature of reflectance measurements influenced the reporting conservative peak values. TMM analysis showed excellent fits to the measured DBR reflectance spectra proving that the VAT is a valuable tool for estimating the reflectance without performing μ-reflectance measurements. The polarization of an incident polarized source after reflection from the DBRs was also preserved ensuring the mirror practicality for the nonpolar orientation.

3. Optically pumped hybrid-cavity nonpolar VCSEL

Optical pumping is commonly used to obtain vital information about the cavity quality and test the emission characteristics before the fabrication of the actual electrical device [121,129,153–157]. Out of these optically pumped demonstrations, only two research groups have successfully shown lasing characteristics from a VCSEL cavity using nanoporous DBRs grown on *c*-plane GaN [121,129].

The VCSEL cavity by Lee *et al*. consisted of a full epitaxial structure using nanoporous DBRs for both the top and bottom mirrors. A single peak stimulated emission was observed at ~413 nm with a threshold pump power density of 7 kW/cm^2 at room temperature (RT) with continuous pumping, shown in Fig. 3.1 (a). Although this was a very impressive design, having a top nanoporous DBR is challenging from an electrically injected device perspective. Dopant diffusion caused by the high temperature required to grow GaN can easily compensate the Mg-doped p-GaN [158]. In addition, the poor conductivity of p-GaN necessitates the use of intracavity current spreading layers like ITO, which would prevent further growth. Nanoporous DBRs can only be grown on top of p-type GaN after the application of a TJ which further adds to the complexity in device fabrication. The nanoporous DBRs often have the tendency to display nonuniform reflectance and aligning to the gain spectrum can be difficult when using two nanoporous mirrors. The resulting stopband of the cavity reflectance is also quite narrow as evident by Fig. 3.1 (a).

Meanwhile, the VCSEL cavity by Zhang *et al*. employed a hybrid design with a top dielectric DBR and a bottom nanoporous DBR. The top dielectric DBR comprised of low-

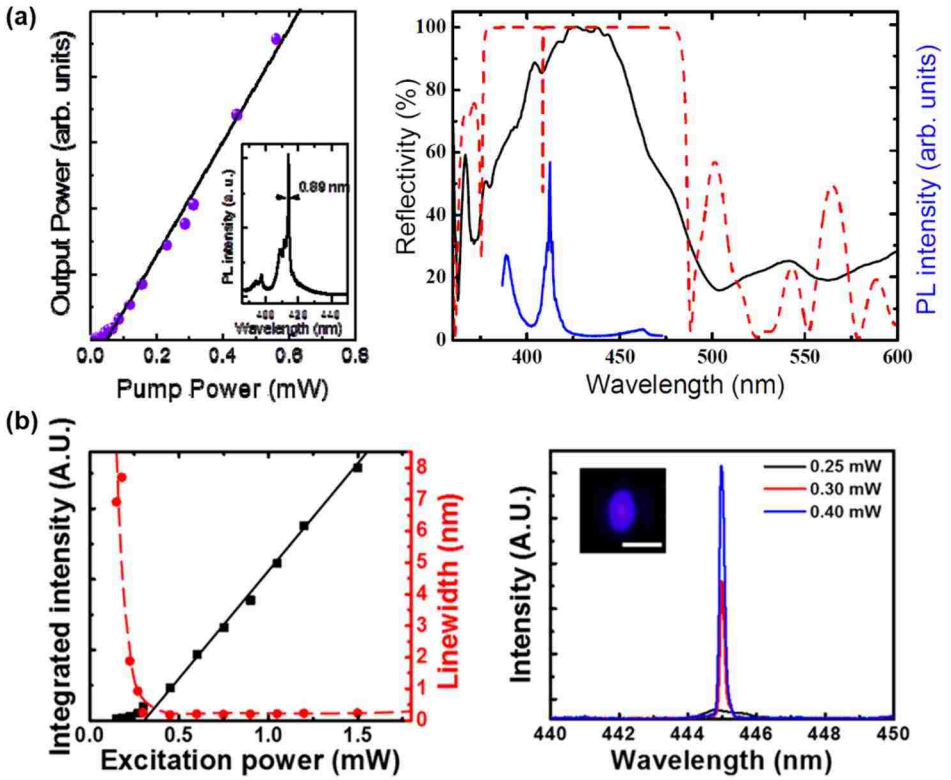

Figure 3.1. *L-L* plot and the spectrum showing the linewidth of an optically pumped *c*-plane VCSEL using nanoporous DBRs from (a) Chonnam National University [129], and (b) Yale university [121]. Plots reprinted with permission.

loss SiO_2/TiO_2 pairs which resulted in a very low threshold pump power density of 1.5 kW/cm^2 as shown in Fig. 3.1 (b). The lasing emission was at 455 nm with a linewidth of ~0.17 nm with a very high Q-factor of ~3000. Such high Q-factors can only be obtained if the mirrors are highly reflective and are well tuned to the gain spectrum. The non-uniformity in the spectrum is reduced in the single nanoporous DBR. The hybrid design also simplifies the fabrication for electrical devices as the post growth deposition of a dielectric DBR allows more room for tunability in both DBRs.

These previous reports have clearly indicated that nanoporous DBRs can indeed be applied to VCSELs and achieve stimulated emission. Moving forward, this chapter will explore whether the nanoporous DBRs can leverage the anisotropic gain properties in *m*-

plane through the optical pumping of a hybrid cavity nonpolar VCSEL [159,160]. The first part of the chapter will discuss the calibration and deposition of the top dielectric DBR. In the second part, the design, growth, and fabrication of the cavity will be provided. Finally, the results from the optical characterization of the VCSEL will be presented showing the nonpolar emission and polarization characteristics.

3.1. Dielectric DBR calibration

The previous chapter described the development of a high reflectance nanoporous DBR on *m*-plane GaN. In order to make the hybrid cavity design for our VCSEL, we must also develop the top dielectric DBR. A Trion PECVD was used to deposit the dielectric materials in which SiN_x and SiO_2 were readily available. According to Table 1.1, a DBR consisting of pairs of SiN_x/SiO_2 should provide adequate index contrast for high reflectance mirrors (>99%) with 15 pairs only [using Eqn. (1.16) and Eqn. (1.17)]. However, reported numbers can vary significantly when compared to the actual material parameters of deposited layers. Determining the exact refractive indices and the deposition rates of SiN_x and SiO_2 are crucial to the fabrication of the DBR. The imaginary part of the refractive index (absorption loss) was assumed to be negligible for our target emission wavelength of 450 nm [161].

To calibrate the deposition rate and the refractive index, two silicon wafer pieces (1 inch by 1 inch) were co-loaded in to the PECVD system to deposit the dielectric material. One of the pieces will blanket deposit the dielectric used for ellipsometry measurements. The other piece was patterned with photoresist (PR) for lift-off to measure the layer thickness using profilometry giving the deposition rate. Films of SiN_x and SiO_2 were then deposited for a fixed amount of time at two different temperatures, 100°C and 350°C.

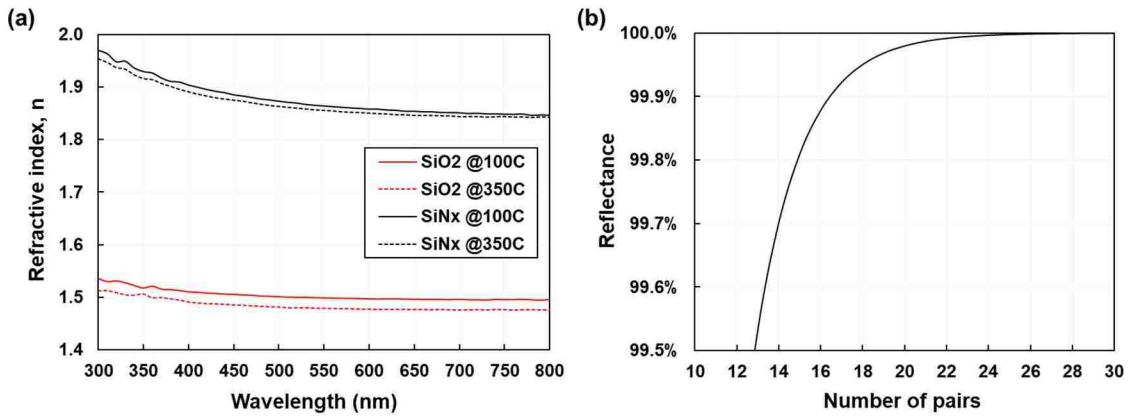

Figure 3.2 (a) Dispersion plot of *n* for SiN_x and SiO_2 at 100°C and 350°C. (b) Calculated plot showing the peak DBR reflectance at 450 nm vs. no. of pairs using films deposited at 100°C.

Typically, high temperatures are preferred for strain relaxation and higher film quality in PECVD dielectrics [162], but a lower temperature would prevent burning of the PR when patterning the DBR structure for future electrical devices. Figure 3.2 (a) shows the dispersion plot for the refractive indices of SiN_x and SiO_2 at the two different deposition temperatures obtained from ellipsometry. No noticeable cracks or considerable changes in the refractive index were observed at either temperature. The measured index of refraction for SiN_x was lower than expected, which could result from the residual oxygen in the chamber forming a composite of SiO_xN_y. Nevertheless, an index difference of 0.38 is achieved (n_{SiO2} = 1.51, n_{SiNx} = 1.89) at 450 nm. Therefore, for the purpose of forming DBR, films were deposited at 100°C but requiring more than 17 pairs to attain a peak reflectance >99.9%, as shown in Fig. 3.2 (b). The patterned sample resulted in a deposition rate of 1.08 nm/sec and 1.93 nm/sec for films of SiO_2 and SiN_x at 100˚C, respectively. The measured profilometer thicknesses (not shown here) also matched with the thickness obtained from ellipsometry mention earlier.

Next, a dummy 20 pair DBR was deposited aiming for λ_B of 450 nm and $\lambda/4n$ thickness of 59.5 nm and 74.5 nm for SiN_x and SiO_2, respectively. The dielectric DBR was

characterized using a UV-Vis Shimadzu spectrophotometer. The measured reflectance spectrum is shown in Fig. 3.3 (a). A peak reflectance of 99.96% was achieved but λ_B blue-shifted by 4 nm to 446 nm and the $\Delta\lambda_{stop}$ was ~55 nm. The blue-shift is a result of slight changes in DBR layer thickness caused by spatial variations in the deposition rate inside the PECVD chamber. It is recommended to place every sample in the exact same location as the calibration samples for accuracy. The exact thicknesses of the layers were measured by cross-sectional SEM imaging [Fig. 3.3 (b)] after dipping a cleaved edge of the DBR in buffer HF for 30 seconds to improve the contrast of the dielectric layers. Here, we see that the average thicknesses of both layers were shorter than the intended design of SiN_x and SiO_2. Overlaying the TMM simulation on top of the newly measured spectrum of the DBR reveal an excellent agreement of the reflectance spectrum in Fig. 3.3 (a). This further verifies the refractive indices and layer thicknesses. Nevertheless, qualitatively comparing the dielectric DBR to a nanoporous DBR design in Fig. 3.3 (c), the color profiles look identical, implying that the two DBR stopbands overlap.

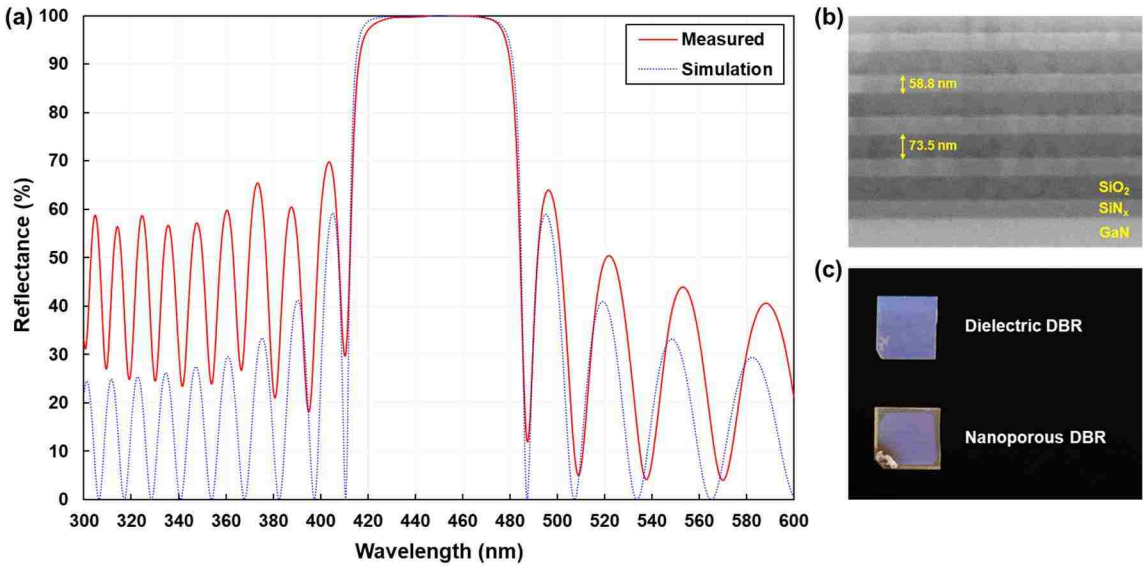

Figure 3.3 (a) Measured and simulated spectra of a PECVD dielectric DBR. (b) Cross-sectional SEM image of the dielectric DBR after buffer HF dip. (c) Photograph of the dielectric DBR and a nanoporous DBR on *m*-plane GaN.

3.2. Design, growth, and fabrication of VCSEL cavity

Gain in a VCSEL cavity is provided by the QWs in the active region. For III-nitride devices emitting in the visible spectral range, the active region is comprised of undoped InGaN QWs with thin GaN barriers. One of the most important requirements for designing a VCSEL cavity is the placement of the active region at the center of a cavity standing-wave peak. This ensures efficient coupling of the gain medium with the cavity mode to maximize the enhancement factor, Γ_{enh}. Thus, 1-D TMM modeling is essential for designing the active region and the VCSEL cavity. TMM simulations require the knowledge of the refractive indices of the layers used in the cavity along with their corresponding internal material losses. These parameters were obtained from ellipsometry measurements of independent films, in addition to reports in literature [96,105,163]. Figure 3.4 shows the dispersion curves for the refractive indices of GaN, $In_xGa_{1-x}N$, and $Al_xGa_{1-x}N$ at various alloy compositions "x", and Table 3.1 lists all the layers used for the TMM analysis. Notice that the QWs in Table 3.1 are lossless which may not be true in the actual devices. This was assumed to simplify the model as we are mostly interested in the trends that arise from design alterations instead of the actual numbers themselves. For an emission wavelength of 450 nm, InGaN of 16% indium was used in the model (not shown in Fig. 3.4).

To optimize the active region design, the thickness (*d*) and the number of QWs (*N*) were varied to minimize the threshold material gain while still maintaining a relatively high enhancement factor. The barrier widths were set to 2 nm to allow room for adjusting *d* and *N*. From an electrical perspective, thin barriers are desirable for the uniform injection of carriers. Uniform injection is not a concern for optically pumped VCSELs since carriers

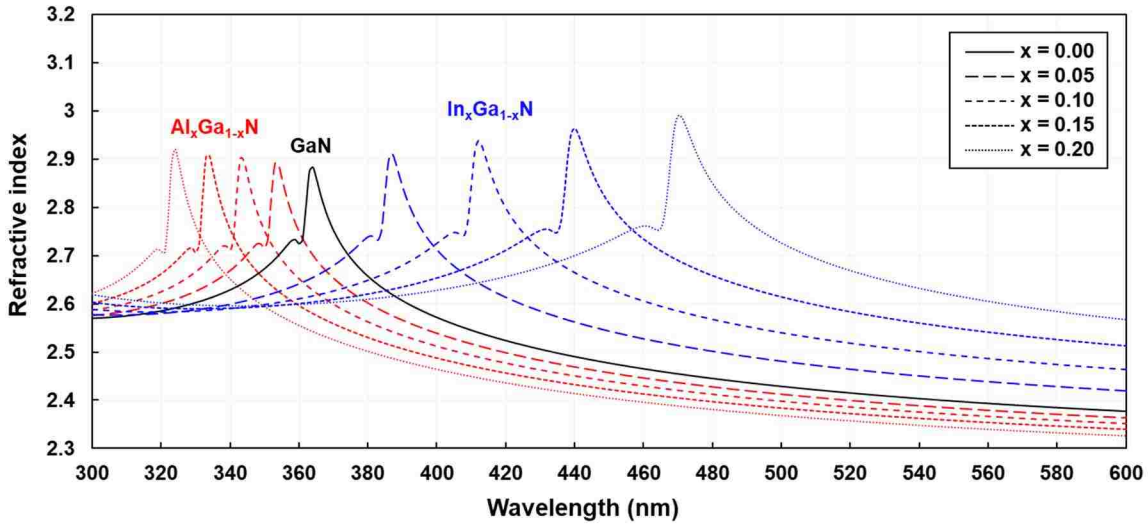

Figure 3.4. Dispersion plot of GaN, $In_xGa_{1-x}N$, and $Al_xGa_{1-x}N$ for x = 0, 0.05, 0.1, 0.15, and 0.2.

Table 3.1 List of all the materials used in the VCSEL cavity for the TMM simulation. The absorption loss values are rough estimates used to determine threshold modal gain [96,163]. Thicknesses will change depending on the active region design. Values provided in the table correspond to the final fabricated VCSEL cavity emitting at 462 nm.

Layer		Thickness (nm)	Refractive index	Absorption loss (cm^{-1})
SiN_x	Top DBR	61	1.89	1000
SiO_2		76	1.51	20
p-clad GaN		72	2.46	5
InGaN QWs	MQWs	5	2.76	
Barrier		2	2.46	5
n-clad GaN		67	2.46	5
Porous GaN	Bottom DBR	59	1.34	6
UID GaN		75	2.46	5

are generated rather than injected, but it will be taken into consideration for the sake of future electrically injected designs. The thicknesses of the n-side and p-side cladding layers were also modified to reflect any changes in the active region design for alignment of the QWs to a standing wave peak. Figure 3.5 (a) shows the plot for Γ_{enh} and g_{th} vs. the QW thickness for a cavity with 3 QWs. A trade-off exists between Γ_{enh} and g_{th} because the enhancement factor should be maximized while minimizing the threshold material gain. Here, both parameters decrease with increasing well widths. This is not surprising, because the optimal overlap of the cavity mode with the active region decreases with increasing

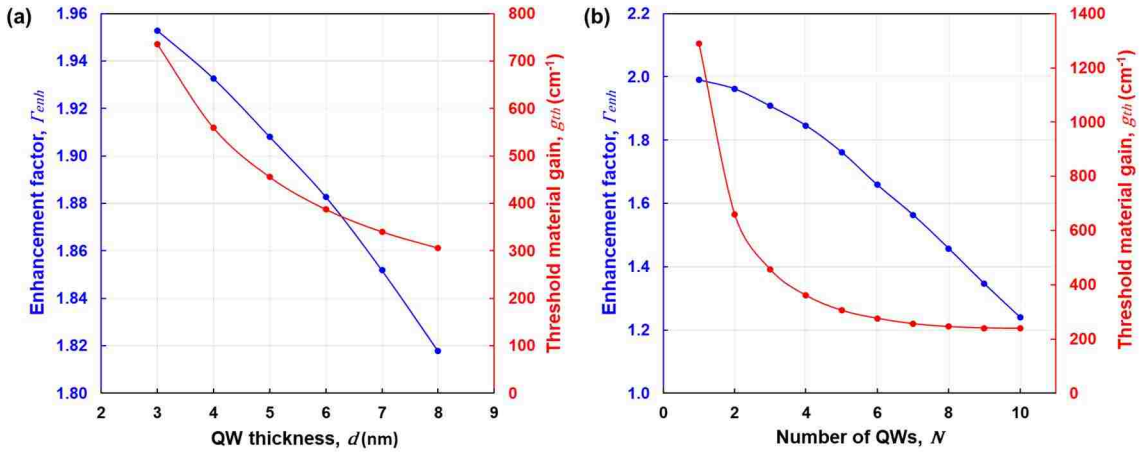

Figure 3.5. Curve of the enhancement factor Γ_{enh} and the threshold material gain g_{th} as a function of the (a) QW thickness d and (b) the number of QWs N. For every data point the p-side and n-side cladding thickness was adjusted to ensure alignment of the active region to a standing-wave peak.

QW width and a wider QW deliver a higher per-pass gain to compensate for the total loss. However, in reality, wide QWs suffer from unconfined carriers due to the shrinking of the subband spacings. As a result, other subbands populate at typical injection levels, degrading the overall QW performance. Similarly, the quantized states are squeezed very close to the barrier levels in narrow QWs. Thermionic carrier leakage becomes an issue at typical injection levels, again compromising the QW performance. Thus, a moderately wide 5 nm QW width was used for the number of QWs study in Fig. 3.5 (b). Figure 3.5 (b) shows similar trends but for a single QW, g_{th} is very high due to the limited gain and drops drastically as the number of QWs increases. Ultimately, g_{th} reaches a saturation point implying that additional QWs do not contribute much in countering the cavity losses while the enhancement factor continues to drop. An active region with a large number of QWs may also suffer from non-uniform carrier injections in the final electrical device. Unpopulated QWs act as highly absorbing passive layers and will likely prevent a VCSEL from reaching stimulated emission. Thus, a conservative 5-pair InGaN/GaN (5 nm/2 nm) MQW design was adopted for the active region and an m-plane sample was grown to the

structure listed in Table 3.1. This produced a minimum threshold modal gain of ~213 cm^{-1} and Γ_{enh} of ~1.8 with an effective cavity length of 2.1-λ ($L_{eff} \times n_{eff} \approx$ 529.5 nm × 1.84). Such a thin cavity is necessary to keep the cavity losses to a minimum and guarantee a single-longitudinal mode emission.

Fabrication of the optical nanoporous VCSEL is very similar to that of the nanoporous DBR. Prior to any of the processing steps described in the previous chapter in Fig. 2.9 (b), a device mesa is ICP etched past the active region and stopping at the n-side cladding layer. The purpose of this mesa was to passivate the active region sidewalls from the EC etch during the porosification process as trapped holes in the MQWs can take part in the wet etching simultaneously. Then after the EC etch and the formation of the 16-pair nanoporous bottom DBR, the protective SiO_2 layer is stripped and the top dielectric DBR consisting of 20 pairs of SiN_x/SiO_2 is blanket deposited to form the hybrid-cavity VCSEL. The cross-sectional schematic of the completed structure is shown in Fig. 3.6.

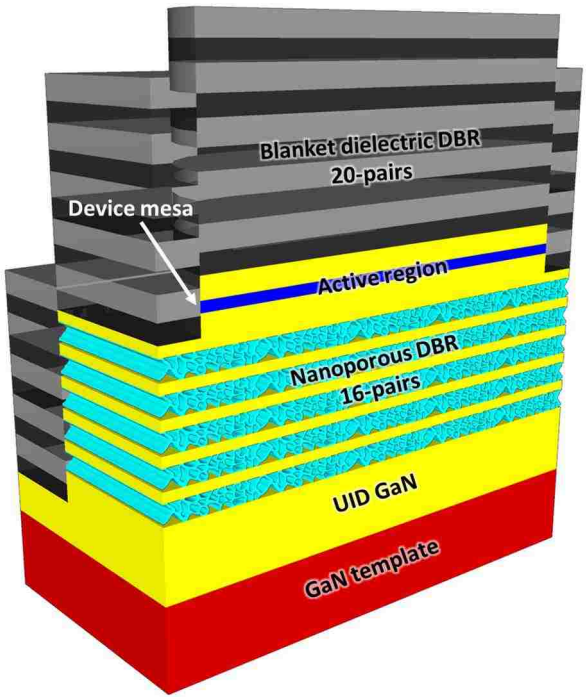

Figure 3.6. Cross-sectional schematic of the hybrid VCSEL structure.

Two major growth discrepancies were observed during the fabrication and characterization of the optical VCSEL. Firstly, as seen from Table 3.1, the nanoporous DBR layer thicknesses do agree with the $\lambda/4n$ condition where the lower index porous layers are smaller in thickness compared to the non-porous GaN layers, shown in the SEM image in Fig. 3.7 (a). Smaller thicknesses correspond to a shorter Bragg wavelength that blue-shifts the DBR stopband and vice versa. Secondly, post growth photoluminescence (PL) characterization revealed that the emission peaked at 470 nm instead of 450 nm. The drift in QW growth temperature resulted in more indium incorporation and red-shifting of the emission wavelength. Figure 3.7 (b) shows PL spectrum of the sample at three different location pumped with a 405 nm laser diode. The emission wavelength was pretty consistent across the entire wafer and the slight change in peak intensity was caused by the spatial variation in light extraction in small wafers. To accommodate the red-shifted gain spectrum and the blue-shifted DBR Bragg wavelength, $\Delta\lambda_{stop}$ must be widened by increasing the refractive index difference in the DBR. Hence, the nanoporous DBR was EC etched with a higher applied bias of 5.5 V with the hopes of lowering the refractive index of the porous layer even further. This was confirmed by the normal incident μ-PL measurement on the fabricated half-cavity (no top dielectric DBR) in Fig. 3.7 (c). The spectrum showed a noticeable improvement in light extraction, with the half-cavity sample with a DBR being greater than 4 times brighter than the sample with an unetched or no DBR. This uniformity in the enhancement of light extraction suggest that the DBR stopband indeed spans across the entire spectrum. The small peaks are artifacts of the air-semiconductor interface causing Fabry-Perot oscillations. Details about the μ-PL setup will be provided in the next section.

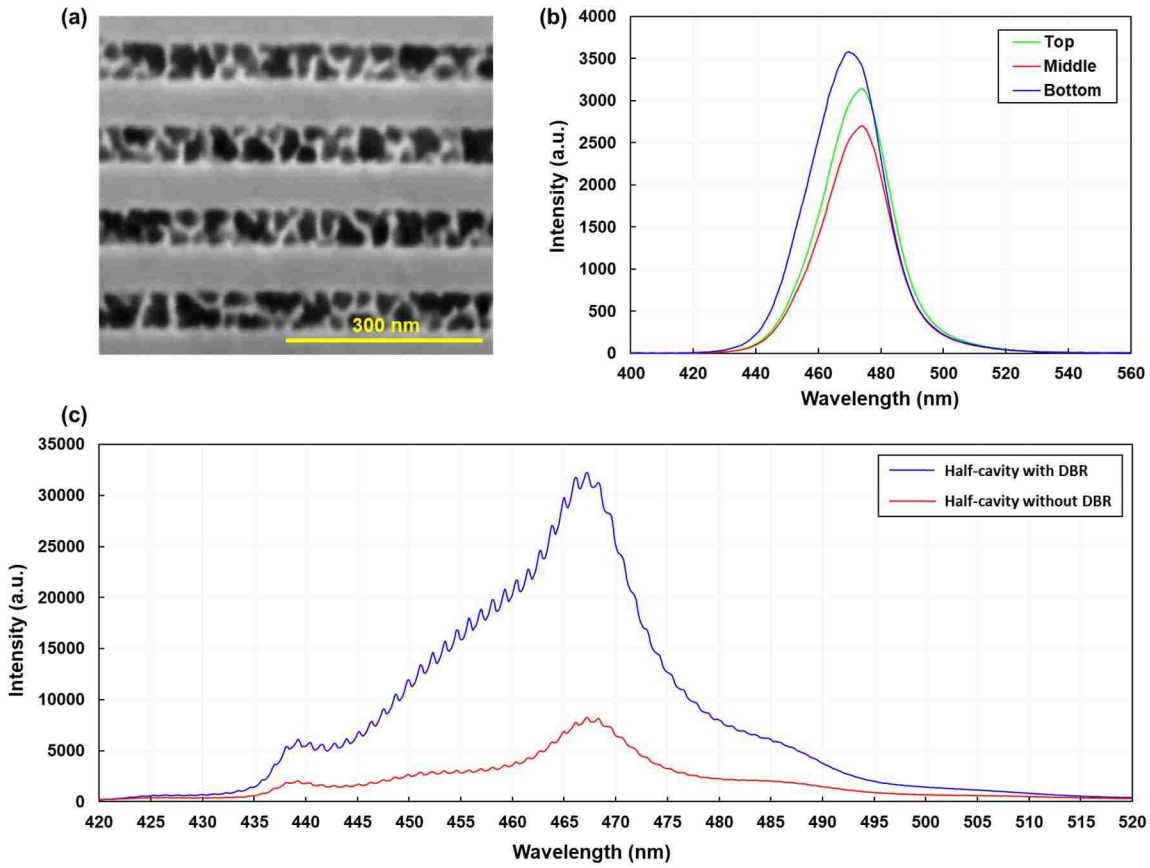

Figure 3.7 (a) Cross-sectional SEM image of the nanoporous DBR, where higher index contrast was required to counter the incorrect epilayer thicknesses. (b) Post growth PL spectrum of the sample before processing. (c) μ-PL spectrum showing 4× improvement in light extraction with the nanoporous DBR uniformly along the entire spectrum.

Setting the peak wavelength from Fig. 3.7 (c) as the Bragg wavelength for the top dielectric DBR, blanket depositions of alternating SiO_2/SiN_x were performed to complete the VCSEL cavity. Spectrophotometer measurement verified the reflectance of the top DBR to be ~99.9%, whereas VAT approximation yielded a reflectance of ~98% for the nanoporous DBR. The completed VCSEL cavity is shown in Fig. 3.8 plotting the refractive index profile and the resulting TMM normalized mode intensity for values mentioned in Table 3.1. The MQWs are positioned at a peak based on the cladding layer thicknesses and the difference in mirror reflectance of the two DBRs essentially make it a bottom emitting VCSEL [159,160].

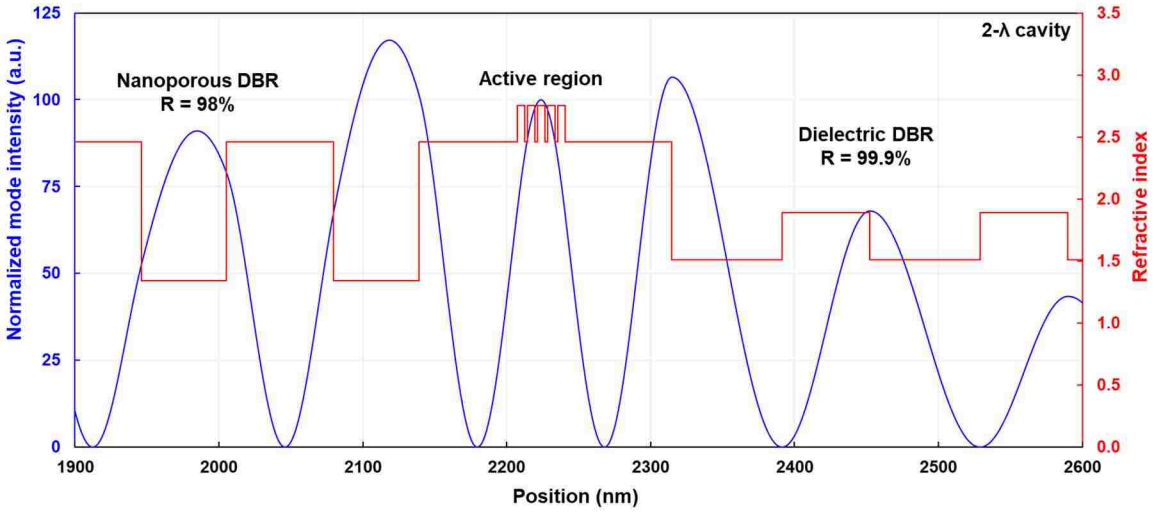

Figure 3.8. 1-D TMM simulation showing the corresponding refractive index profile and the normalized mode intensity of the completed nanoporous VCSEL cavity.

3.3. Optical characterization of nonpolar nanoporous VCSELs

To optically pump the nonpolar nanoporous VCSEL structure, the μ-reflectance setup mentioned in the previous chapter, was converted to a transmission mode μ-PL setup. Optical characterization was done on the backside of the sample since the VCSELs were bottom emitting by viewing through a CCD camera and pumping the devices from the top. The broadband light source was replaced with a 400 mW 405 nm laser diode as the pump source producing a circular profile with a diameter of ~8 μm. Modifications to the setup now included a transparent thermally conductive SiC sample mount to mitigate self-heating, a secondary collection objective on the backside mounted on a polarizer, an 0.2 OD filter to prevent saturation of the spectrometer, and a 405 nm high-pass filter to remove the pump laser signal. Almost all components in the setup were mounted on x/y/z/θ micro-manipulators to focus and align the beam for optimized collection. This allowed quick testing of many devices over a large area simply by moving the sample stage instead of having to realign the optics every time. Figure 3.9 illustrates the schematic of the μ-PL

setup along with a CCD camera image of the pump laser spot size and a photograph of a lasing device [See Appendix A.6 for the actual photo of the setup].

The PL spectrum of the emission at various pump power densities is shown in Fig. 3.10 (a) where a single-mode stimulated emission peak at 462 nm was observed. Translating the spectrum into an integrated PL plot [Fig. 3.10 (b)], a clear non-linear lasing *L-L* plot characteristic was observed with a threshold pump density of ~5 kW/cm^2 with no apparent thermal roll-over. This threshold power density is similar to the optically pumped nanoporous VCSEL reported in [129] but still larger than the nanoporous VCSEL reported

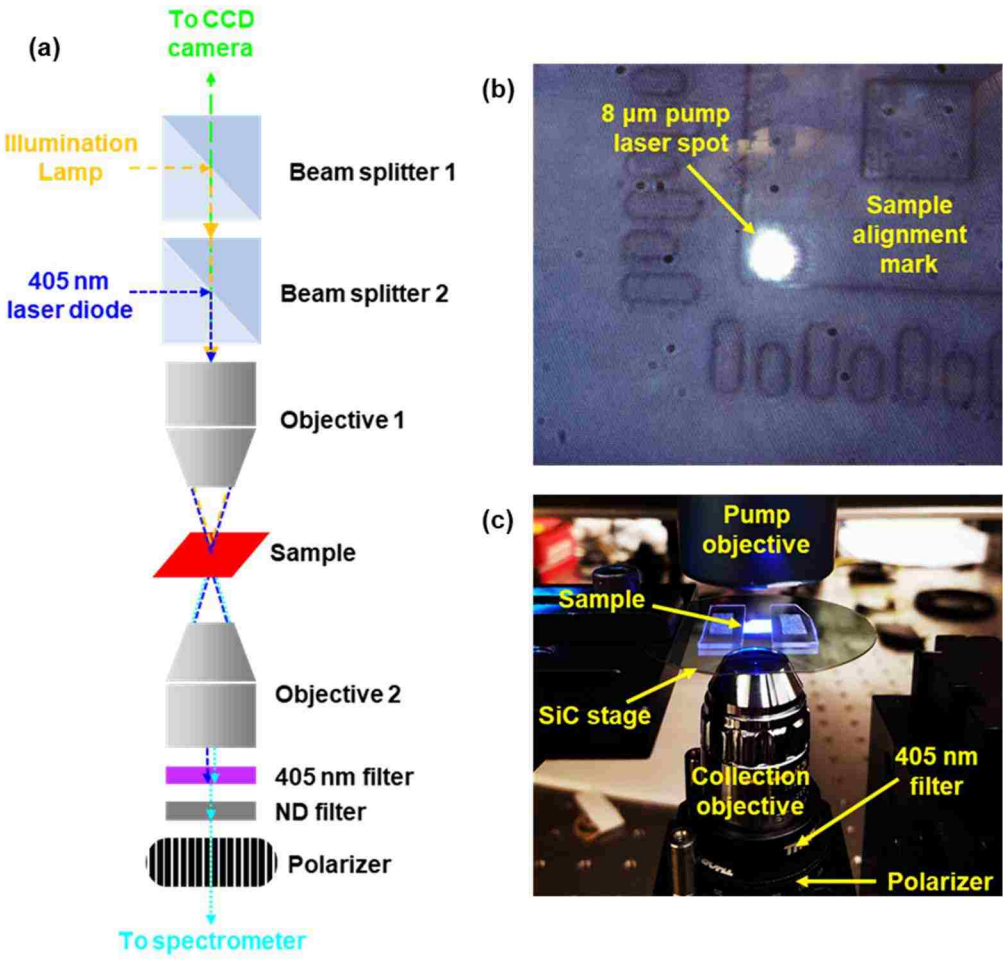

Figure 3.9 (a) *μ*-PL setup where the samples are pumped by a 405 nm laser diode from the top and the emissions are collected from the bottom. (b) CCD camera image showing the pump laser spot diameter relative to a sample alignment mark. (c) Photograph of the optically pumped nanoporous VCSEL.

in [121], due to the incorrect epilayer thicknesses and absorbing dielectric materials. The emission linewidth is also plotted in Fig. 3.10 (b) where the FWHM drops gradually due to the double peaking of the spontaneous emission at 458 nm and 462 nm. Once stimulated emission commences, the mode at 462 nm subdues the 458 nm peak and the FWHM drops to ~0.12 nm, which was close to the resolution of the spectrometer. Note that the maximum output power of the VCSEL was limited by the μ-PL setup itself. The pump laser had already reached its maximum output power at 6.5 kW/cm^2. Additionally, saturation of the spectrometer caused a slight increase in linewidth beyond threshold. The cavity Q-factor was estimated to be ~1871 using

$$Q = \frac{2\pi}{\lambda}\frac{n_g}{\Gamma g_{th}} \tag{3.1}$$

where, λ is the emission wavelength, n_g is the group index and Γg_{th} is the threshold modal gain (2.93 and 212.8 cm^{-1}, obtained from TMM, respectively) [9,164]. The reason Q-factor is calculated this way instead of the more traditional $\lambda/\Delta\lambda$ is that the conventional method neglects the linewidth narrowing at the onset of stimulated emission and greatly overestimates the Q-factor. $\lambda/\Delta\lambda$ is accurate when determining the Q-factor of a cold cavity in the absence of any form of emissions. Here, the high Q-factor is a direct result of the high reflectance in the DBR mirrors. Figure 3.10 (c) shows the polar diagrams of the integrated PL at three different lasing spots on the wafer. The spectrum was recorded after the polarizer was rotated in 10-degree increments and integrated over the entire spectrum (spontaneous and stimulated emission). The polarization ratios for spot 1, spot 2, and spot 3 were 82%, 72%, and 84%, respectively. The relatively smaller polarization ratios compared to a previously published work on m-plane VCSELs are due to the inclusion of

spontaneous emission in the integration of the PL [78]. We note that removing the spontaneous emission and integrating the spectrum across only the stimulated emission region would result in a polarization ratio of ~99%. The relatively high polarization ratio validates the fact that the scattering effects from the nanoporous layers can be assumed negligible. In the previous chapter, it was concluded that the nanoporous DBRs maintain the polarization properties of an incident polarized source regardless of the pore alignment in the *a*- or *c*-directions [149]. Figure 3.10 (c) shows that all lasing spots were polarization-pinned emission in the *a*-direction, further solidifying out claims.

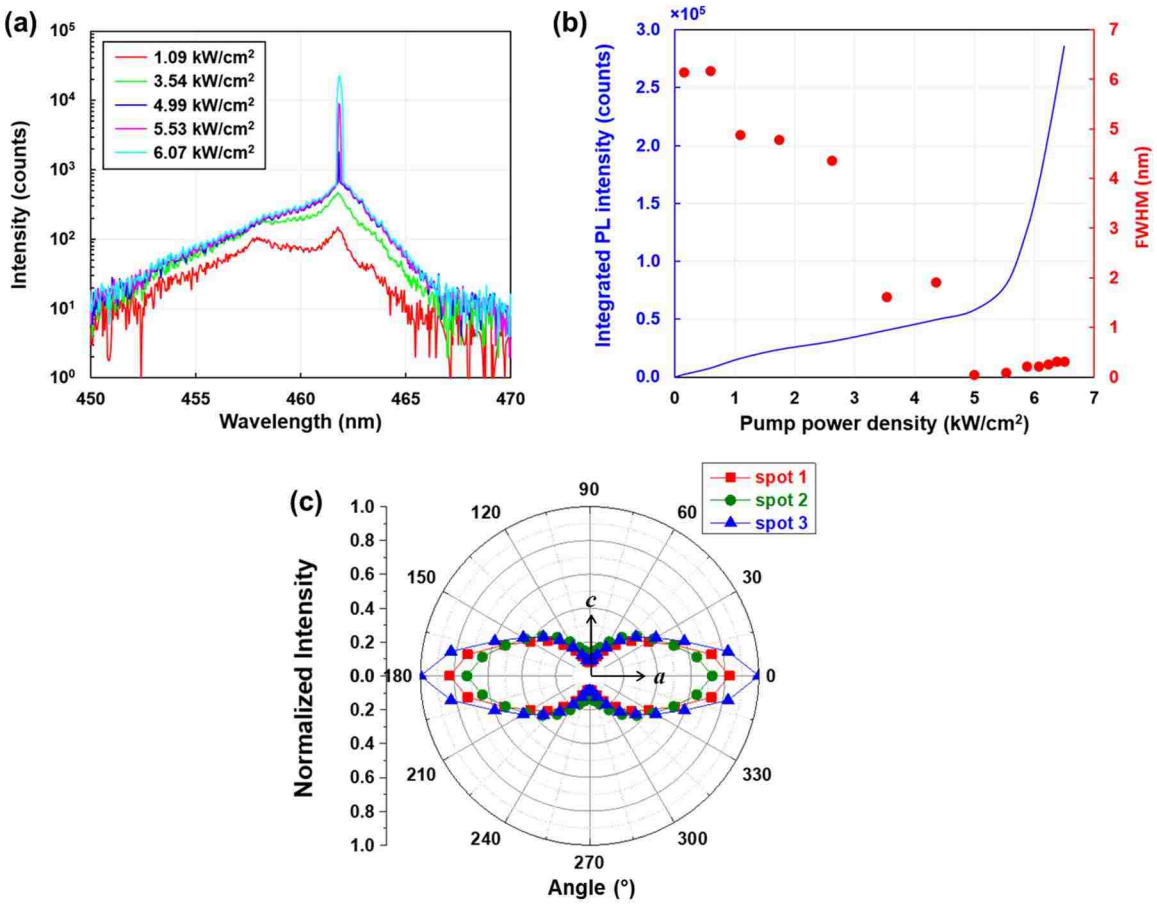

Figure 3.10 (a) *μ*-PL emission spectra of a VCSEL at various pump power densities. (b) Integrated PL and FHWM plot. (c) Polar plot showing polarization-pinned emissions at 3 different lasing spots.

The spontaneous emission factor, β_{sp}, is a useful parameter to evaluate for VCSELs because it expresses how much of the spontaneous emission gets coupled into the cavity. Typically, β_{sp} can be roughly estimated from the difference in intensity before and after the lasing threshold on a normalized log-scale *L-L* plot. The limited output power in the VCSELs restricted this measurement from Fig. 3.10 (b), however, since no thermal roll-over was observed, the data can linearly extrapolated up to 100 kW/cm^2, allowing us to approximate β_{sp}. The log-scale plot is shown in Fig. 3.11, where we obtain β_{sp} of ~2×10^{-2}. To verify this value, we can also calculate β_{sp} from the Purcell factor given as [9,165]

$$F_p = \frac{3}{4\pi^2}\frac{Q}{V_c/(\lambda/n_{eff})^3}, \tag{3.2}$$

$$\beta_{sp} = \frac{F_p}{1+F_p}. \tag{3.3}$$

Here, F_p is the Purcell factor, Q is the cavity Q-factor from Eqn. (3.1), V_c is the optical cavity volume measuring 2.7×10^{-11} cm^3 for an 8 μm aperture diameter and a 529.5 nm effective cavity length, λ is the emission wavelength (462 nm), and n_{eff} is the effective cavity refractive index (1.84). Using Eqn. (3.2) and Eqn. (3.3), the calculated β_{sp} was ~8×10^{-2}, which is within the same order of magnitude as the estimated β_{sp}. Note that β_{sp} is three orders of magnitude greater than that of typical edge-emitting lasers (on the order of 10^{-5}), indicating the enhancement of the spontaneous emission into the lasing mode by the high-Q cavity [166,167].

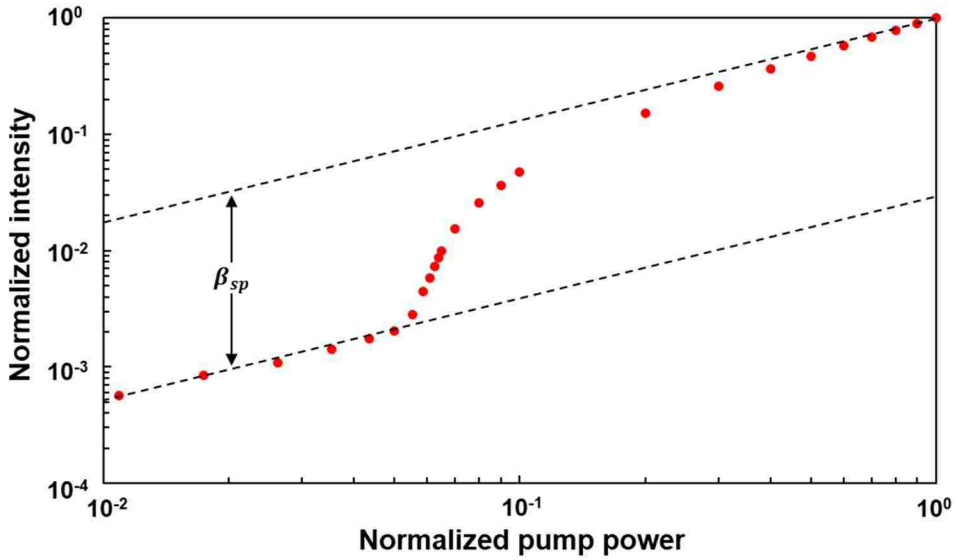

Figure 3.11. Log-scale plot of the normalized pump power vs. the normalized emission intensity.

Several other lasing peaks were also observed at various regions across the sample. Figure 3.12 (a) shows the PL spectrum of four such spots. We believe the variation in emission wavelength was caused by the higher EC etch bias used to compensate for the growth error mentioned in Section 3.2, where the thickness of the nanoporous layers were thinner than the nonporous GaN layers [Fig. 3.7 (a)]. The higher bias resulted in some pores to agglomerate to form even larger pores resulting in very localized areas of lower effective refractive index. As a result, regions of nonuniform effective cavity lengths were generated with varying cavity resonance, producing different lasing peaks throughout the sample. Spatial differences in the cavity length is evident by the colorful streaks in the microscope image in Fig. 3.12 (b) where non-uniform mirror reflectance in the DBR occurs. If the layer thickness were correct, EC etch could be performed at lower bias voltages to achieve much more uniform porosification and hence a uniform cavity resonance.

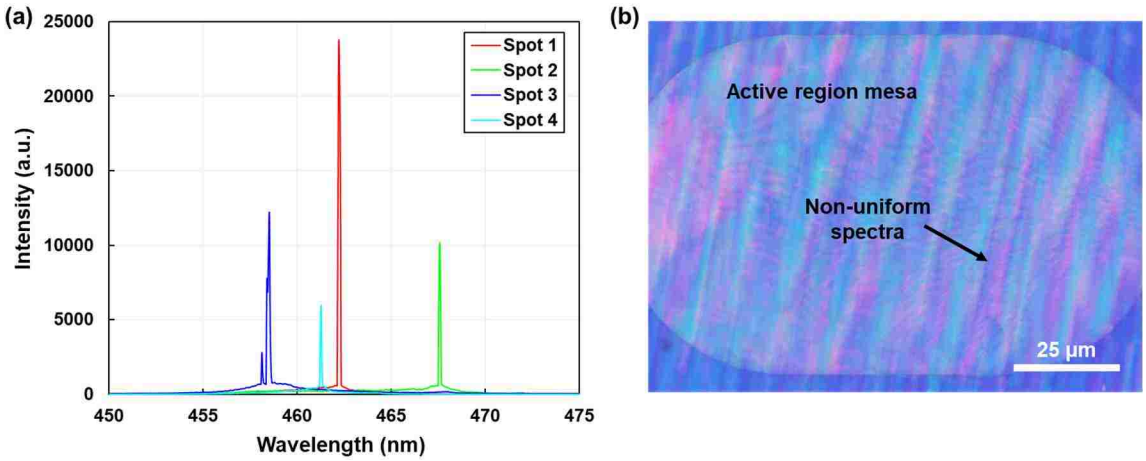

Figure 3.12 (a) Emission spectra of several VCSEL devices showing lasing emission at different wavelengths. (b) Microscope image of a device mesa with non-uniform spectra due to large pores sizes.

3.4. Summary

Extending the work on nonpolar nanoporous DBRs from the previous chapter, this chapter implemented an active region capped by a top dielectric DBR to form a hybrid cavity VCSEL structure. An optically pumped VCSEL was demonstrated with single-mode lasing emission at 462 nm with a narrow linewidth of ~0.12 nm. The stimulated emission threshold was ~5 kW/cm^2 with a measured β_{sp} in the order of 10^{-2}. Several lasing spots were examined for polarization pinning, and all spots were found to be locked in the *a*-direction which is characteristic of *m*-plane nonpolar GaN devices. The uniformity of the lasing peaks can be improved greatly by growing the DBR stacks in their corresponding $\lambda/4n$ thicknesses and forming high density small pores in the doped layers. Overall, these results indicate the versatility of the nanoporous approach even with misaligned cavity mode and gain spectrum, making the nanoporous DBR a strong candidate for solving some of the issues affecting III-nitride VCSELs and for achieving electrically injected devices.

4. Electrically injected nonpolar VCSEL using nanoporous DBRs

In the past, nonpolar VCSELs have been exclusively studied by a research group at the University of California, Santa Barbara [76,78,80,81,83,89,90]. Their device design involves the flip-chip approach using PEC etching for controlling the cavity length and transfer devices to a submount. Figure 4.1 depicts a schematic of a flip-chip nonpolar VCSEL. The design used double dielectric DBR mirrors and they were able to demonstrate the first 100% polarization-pinned emission from a nonpolar VCSEL [78]. Additionally, several other advancements were made, for example replacing the ITO current spreading intracavity contact with a GaN TJ [81], tighter control of the lateral optical confinement using PEC etched apertures [83], and CW lasing at RT using a long cavity design [89].

Nevertheless, the use of an n-side dielectric DBR makes the fabrication process extremely complicated. Not only is the device yield affected by the incomplete PEC etching and improper bonding, the delicate nature of the devices requires a great deal of care during processing steps post flip-chip. This restricts the use of any physical treatments

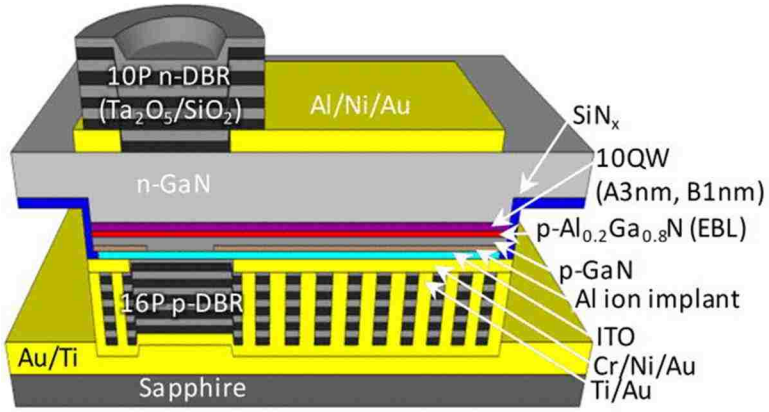

Figure 4.1. Schematic of the flip-chip nonpolar VCSEL with the aperture defined by Al-ion implantation into p-GaN. ITO layers were later replaced with GaN-based TJs. Reprinted from [80], with the permission of AIP Publishing.

like sonication and other cleaning procedures. Also, the output powers were very limited from early thermal-rollover due to the p-side dielectric DBRs insulating the VCSELs, preventing effective heat extraction from the devices. These were common traits observed when we attempted to fabricate a flip-chip nonpolar VCSEL in the UV spectral range here at UNM in collaboration with UCSB.

In this chapter, we demonstrate the first electrically injected nonpolar *m*-plane GaN-based VCSELs with lattice-matched nanoporous bottom DBRs. Before going into the fabrication and characterization of the nanoporous VCSELs, we will first discuss some of the new components and design choices implemented in the VCSEL cavity to enable electrical injection. Next, the issue of incorrect growth thicknesses from the last chapter will be addressed using a combination EC and PEC based growth rate calibration techniques to grow the appropriate layer thicknesses. Finally, the electrical characterization will be done where we explore the device performance along with the optical and thermal characteristics of the VCSELs.

4.1. Design consideration

Optically pumped VCSELs, as demonstrated in the previous chapter, only require the gain (MQWs) medium, cladding layers, and two DBR mirrors for a device to lase with a pump source. The cavity design becomes a little more complicated when attempting an electrically injected VCSEL. New components such as the aperture, current spreading layers, and metal contacts are necessary in addition to the components for optically pumped VCSELs. This section will discuss the aperture definition and the intracavity contact layer to provide an explanation behind the design choices.

4.1.1. Aperture design

The aperture in a VCSEL confines the lateral optical mode inside the gain region while also providing current confinement to attain high current densities necessary for laser operation. Historically, even in the early nonpolar VCSELs, the apertures were defined using a patterned layer of dielectric material (either SiO_2 or SiN_x) on top of p-GaN for its simplicity, creating a step in the surface profile outside the aperture [64,66,74,76,82]. Then in 2013, theoretical studies on planar vs. step profile done by Hashemi *et al.* revealed that a step in the aperture can have detrimental anti-guiding effects in terms of lateral confinement [168]. Figure 4.2 summarizes the results where it shows that a positively guided ($\Delta n_{eff} = n_{eff,core} - n_{eff,clad} > 0$) planar profile exhibited a much lower threshold material gain compared to a negatively guided structure ($\Delta n_{eff} = n_{eff,core} - n_{eff,clad} < 0$). Positive guiding implies a greater overlap between the mode and the gain region and vice versa. The continual increase in Δn_{eff} resulted in a slight increase in threshold gain due to enhanced diffraction loss. In the report, the positive guiding planar structure was obtained by etching the aperture in the p-GaN and depositing the dielectric of the same thickness. This process, however, risks plasma damage of the p-GaN at the periphery of the aperture which could potentially roughened the sidewalls leading to an increased scattering loss.

Alternatively, the planar profile can also be achieved by patterned ion implantation. Noteworthy work on nonpolar GaN VCSELs with Al-ion implanted apertures has been conducted by Leonard *et al.* [80], and the ion implant process was adopted by UNM during the collaboration with UCSB. Basically, the Al-ion passivates p-GaN to create patterned resistive areas outside the aperture, enabling lateral current confinement without

incorporating the step profile seen on dielectric apertures. All ion implantations were performed by a vendor, Leonard Kroko Inc., where Al-ions were implanted with a dose of 10^{15} cm^{-2} at normal incidence. Figure 4.3 (a) plots the current density vs. voltage plot for several implant energies comparing to a recessed PECVD SiN_x aperture. Evidently, the dielectric aperture showed the highest turn-on voltage due to the plasma damage of p-GaN caused by the dielectric deposition. Of the three implant energies tested, there were no observable trends which lead to choosing the implant energy with the lowest turn-on voltage (20 keV). Following this experiment, ellipsometry on a sample before and after ion implantation was performed to determine the change in the lateral refractive index. As seen from Fig. 4.3 (b), there was an approximately 2% reduction in the refractive index of *m*-

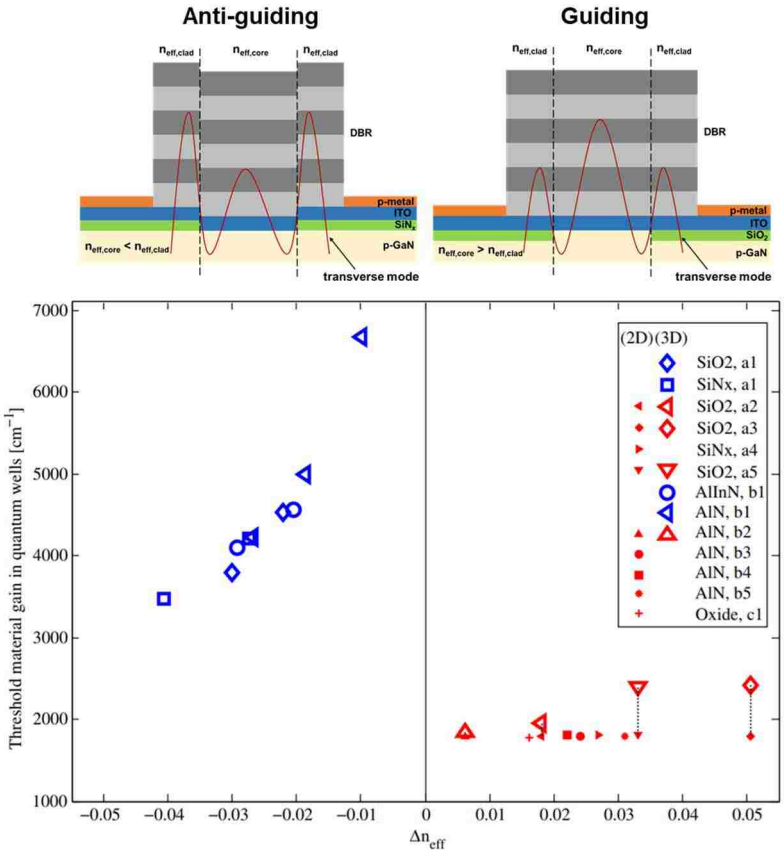

Figure 4.2. Simulation of the threshold material gain vs. effective index contrast. Left side shows the anti-guiding step profile structure with higher threshold gain compared the right side planar guiding structure. Reprinted from [168].

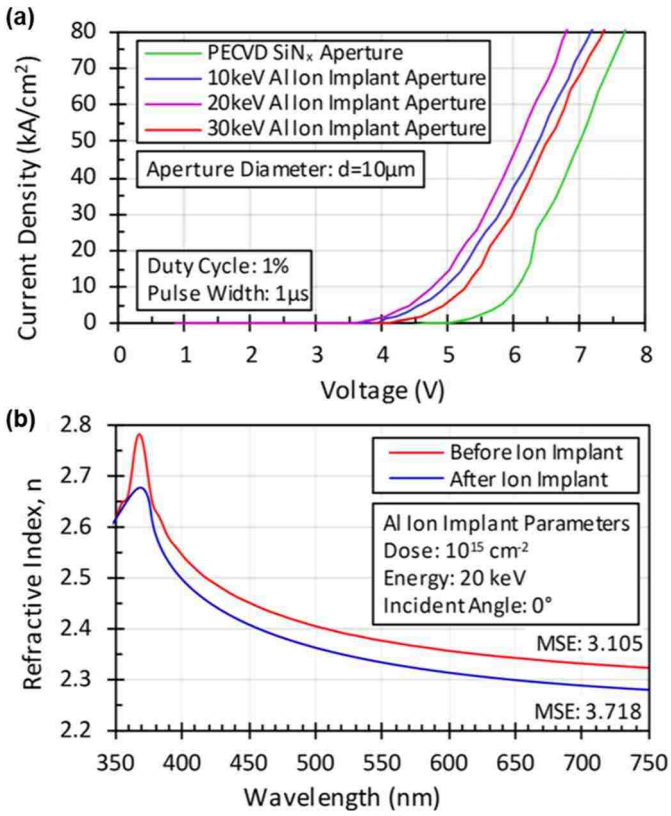

Figure 4.3 (a) *J-V* characteristic for a partially process VCSEL with Al-ion implanted apertures at various energies comparing to a recessed SiN_x aperture. (b) Dispersion plot for the refractive index of *m*-plane GaN before and after Al-ion implantation. Reprinted from [80], with the permission of AIP Publishing.

plane GaN in the visible range of the spectrum after Al implantation. Thus, positive guiding can be achieved with the negative change in the refractive index of GaN.

From our earlier work on the flip-chip nonpolar UV-VCSEL, the actual penetration depth of ions at 20 keV was much greater than the predicted ion range which caused catastrophic damage to the QWs. Using the simulation program called Stopping Range of Ions in Matter (SRIM) the implant depth was estimated. Figure 4.4 (a) shows a screenshot of a simulation result for Al-ions being implanted in GaN at normal incidence with 20 keV energy and 10^{15} cm^{-2} dose. The ion range is the depth at which the ion concentration is the highest and the straggle refers to projection of ion beyond the ion range. To limit the implant depth due to straggle, a layer of SiO_2 was deposited using e-beam on the sample

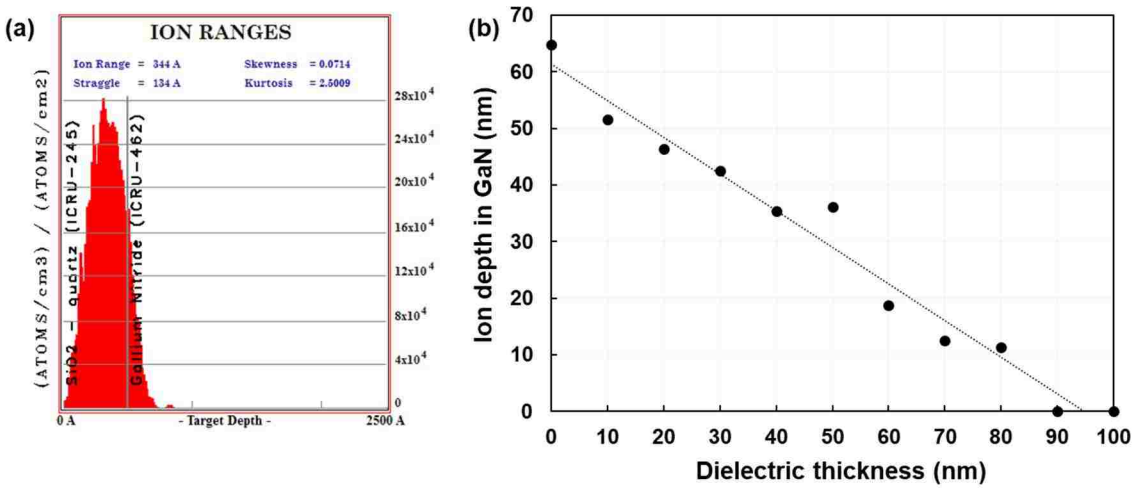

Figure 4.4 (a) SRIM simulation of SiO_2 on GaN showing the Al-ion implant depth at 20 keV with a dose of 10^{15} cm^{-2} in normal incidence. (b) Depth of ion projected in GaN including straggle as a function of the SiO_2 thickness.

to control the dose and trap the ion up to p-GaN. The thickness of SiO_2 was determined using SRIM and the simulation results are shown in Fig. 4.4 (b). Here, the implant depth in GaN (ion range + straggle) decreases linearly with increasing SiO_2 thickness until GaN is no longer implanted with 90 nm of SiO_2. With no dielectric layer to reduce the dose, the implants had a projected range of ~ 65 nm into p-GaN. As we will see in the following sections, the thickness of p-GaN layers in the nonpolar nanoporous VCSELs were sufficiently large to allow ion implantation without the need for the additional SiO_2 layer.

4.1.2. Intracavity current spreading layer and p+/n+contacts

In the past, ITO has been the most commonly used as an intracavity current spreading layer for p-GaN [67,72,76,82,88]. ITO is attractive to both the industry and academic research groups due to its ease of deposition and the cost-effective formation of transparent and conductive films. The best quality ITO films can be obtained through sputtering based deposition techniques which yield transparency ~90% and resistivity between ~10^{-4} to 10^{-3} Ω-cm [169–171]. However, the onset of high-energy plasma damage to p-GaN in

conventional DC or RF sputtering systems eliminates its usefulness for VCSEL applications [172,173]. There are reports of remote-plasma systems like electron-cyclotron resonance (ECR) sputtering which can alleviate the plasma damage [174,175]. But the unavailability of such systems in addition to the logistical restraints to have the deposition performed by a vendor compelled us to rely on e-beam deposition techniques.

Smooth (RMS < 1 nm), low resistivity (~10^{-4} Ω-cm), and transparent (~90% at 405 nm) multilayer ITO films have been demonstrated using e-beam deposition [176]. Smoothness of the films are critical for minimizing scattering loss as a rough ITO layer will inevitably worsen the roughness through the subsequent dielectric DBR deposition. Unlike [176], which only heated the sample during deposition, our e-beam system utilizes an indirect heating mechanism and performing depositions under similar conditions resulted in very rough films. The series of coil heaters at the bottom of the chamber which provided the indirect heating, more than likely degassed materials from the chamber walls causing the high roughness and poor film quality. All depositions beyond this point were performed at RT to avoid degassing during deposition. The ITO pellets used in the system comprised of In_2O_3/SnO_2 (90/10% wt.) and 50 nm ITO films were deposited at a rate of 0.5 Å/s under 10 sccm O_2 flow. The resulting films were initially dark (not fully transparent) but a post-deposition anneal in a rapid thermal annealer (RTA) with N_2 ambient at 550°C for 15 minutes improved the crystallinity of the ITO films and enhanced the transparency [177–179]. Smooth ITO films were obtained as evident by the 20 μm by 20 μm window AFM scan in Fig. 4.5 (a), showing an RMS roughness of ~0.6 nm.

It should be noted that the ITO layer contributes the most to internal loss α_i in the cavity [180,181]. As such, the ITO layer must be positioned at a standing-wave null to

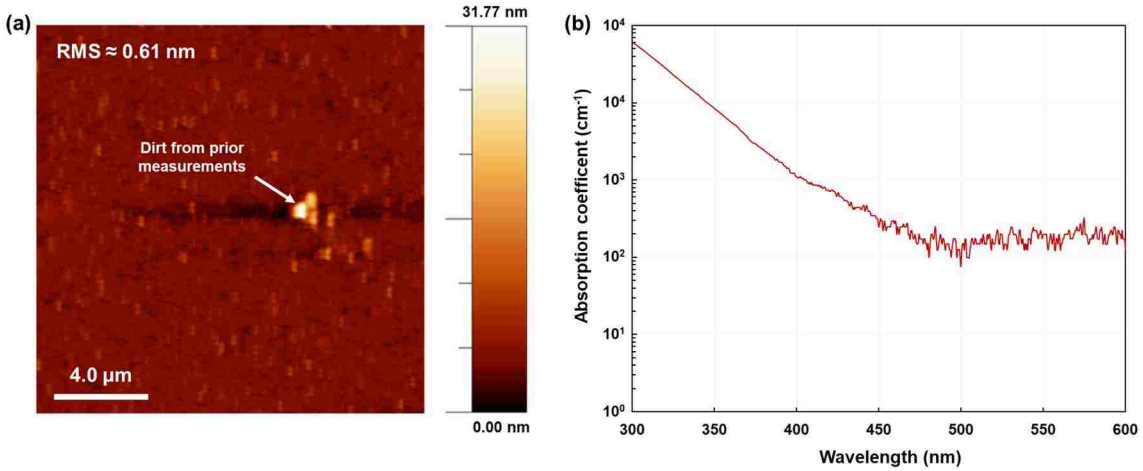

Figure 4.5 (a) 20×20 µm AFM scan of a 50 nm e-beam deposited ITO film after anneal showing an RMS roughness of ~0.6 nm. (b) Absorption coefficient of the same ITO film as a function of wavelength calculated using *R*+*T* measurements.

mitigate the high absorption coefficient. Optical characterizations of ITO involving the use of thick films which can overestimate the absorption coefficient by incorporating the scattering loss associated with increased roughness. The use of thin films rectifies this error and *R*+*T* measurements was performed using a UV-Vis spectrophotometer to determine the absorption coefficient of a 50 nm ITO film on a double-side polished sapphire wafer [182]. The surface reflection and transmission was recorded for the ITO sample along with a bare sapphire wafer to calculate the absorption coefficient of ITO using:

$$A_{ITO} = R_{sap} + T_{sap} - R_{ITO+sap} - T_{ITO+sap} \tag{4.1}$$

$$\alpha_{ITO} = -\frac{ln(1-A_{ITO})}{d_{ITO}} \approx \frac{A_{ITO}}{d_{ITO}} \tag{4.2}$$

where, R_{sap} & $R_{ITO+sap}$ and T_{sap} & $T_{ITO+sap}$ are the percentage reflection and transmission of the bare sapphire wafer and ITO sample. The bare sapphire wafer was necessary for cancelling the light absorption in sapphire. Absorption coefficient of ITO was then calculated by dividing A_{ITO} by the thickness of the ITO film d_{ITO}. Figure 4.5 (b) plots α_{ITO} for a range of different wavelengths. Towards lower wavelengths when

approaching the band-edge absorption of ITO, α_{ITO} increases exponentially and at 450 nm, α_{ITO} is ~250 cm^{-1}.

Before determining the electrical properties of the intracavity ITO, pGaN, and nGaN contact layers, it is important to have an understanding of Circular Transfer Length Method (CTLM) analysis [183–185]. CTLM is a two-probe characterization technique which tracks the changes in total resistance R of an underlying layer as a function of the circular metal pad spacing s. A schematic of the CTLM metal pads are depicted in Fig. 4.6, where the inner and outer circle radius is r_1 and r_2, respectively. CTLM converts the non-linear

R versus s characteristics to a linear fit allowing one to approximate the sheet resistance R_{sh}, contact resistance R_c, specific contact resistance ρ_c, and resistivity ρ of the underlying layer. The linear expression for the resistance is given as

$$R = \frac{R_{sh}}{2\pi r_1}(s + 2L_t) \cdot c \qquad r_1 > s \gg L_t \tag{4.3}$$

$$c = \frac{r_1}{s} ln\left(\frac{r_1+s}{r_1}\right) \tag{4.4}$$

where, L_t is the transfer length and c is the linearity correction factor [183]. The transfer length is a measure of how ohmic the contact is. A non-ohmic contact will have larger L_t than an ohmic contact. Note that this model is only valid when the physical dimensions of the metal pads are much greater than the transfer length of the layer. As evident in Eqn. (4.3), R_{sh} can be calculated from the slope and the y-intercept is equivalent to $2R_c$. The transfer length can be evaluated from the x-intercept which is equal to $2L_t$. Then multiplying R_{sh} with the thickness of the underlying layer gives its resistivity and R_{sh} times L_t estimates the specific contact resistance ρ_c.

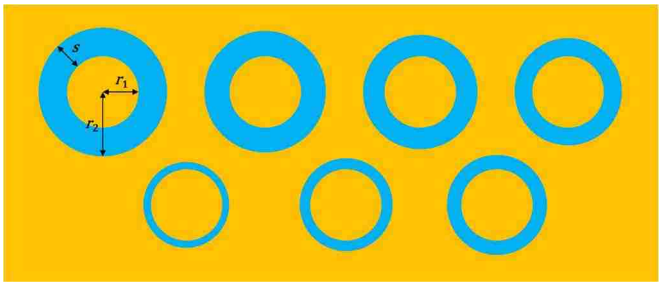

Figure 4.6. CTLM metal pad pattern. The inner circle and the outer rectangular region is probed. The circular pattern prevents the current from one contact spreading into another due to current crowding.

To test the electrical properties of the ITO, n-GaN, and p-GaN contact layers using CTLM, three samples were fabricated as illustrated in Fig. 4.7. For ITO, a 50 nm film was deposited on sapphire (insulating) and annealed followed by the deposition of the Ti/Au metal contacts of thickness 20/300 nm [Fig. 4.7 (a)]. The contacts were ohmic and CTLM estimates a sheet resistance of ~160 Ω/□ and a resistivity of ~1×10^{-3} Ω-cm. To characterize the p-GaN contact layer, a layer of patterned ITO layer was deposited to replicate the VCSEL contact followed by metal contacts deposition to allow current to pass through the p-GaN layers only as per Fig. 4.7 (b). For the n-GaN contact layer, the contact metals were Ti/Al/Ni/Au with thicknesses 20/100/50/300 nm which were deposited on top of n+GaN contact layer used for typical *m*-plane LEDs [Fig 4.7 (c)]. Figure 4.7 (d) plots the *I-V* characteristics of both the p-GaN and n-GaN contacts for a series of CLTM spacings. As expected, p-GaN exhibits non-ohmic characteristics due to the poor efficiency of Mg-acceptor activation, whereas the n-GaN contacts were ohmic with very low series resistance. CTLM approximation is relatively easy for ohmic contacts due to the linear current to voltage relationship giving a constant value for the slope and intercepts in Eqn. (4.3). The calculated R_{sh}, R_c, ρ_c, and ρ for the n-GaN contact layer was ~1100 Ω/□, ~140 Ω, 0.01 Ω-cm^2, and 0.022 Ω-cm, respectively. Note that two probe measurements incorporate probe resistances into R_c when the voltage is measured simultaneously by the

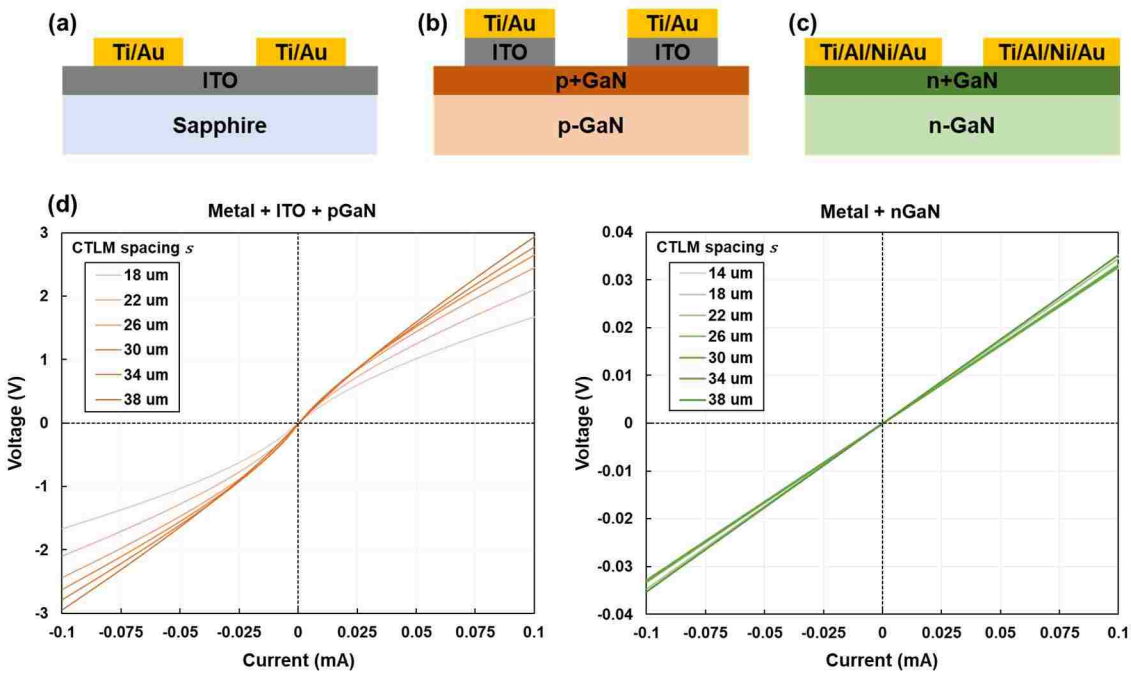

Figure 4.7. Sample schematic for characterizing (a) ITO, (b) p-GaN, and (c) n-GaN. (d) *I-V* characteristics obtained from (b) and (c) for various CTLM spacings.

same probes that drive the current. A four-probe system should be applied for more accurate results, where two probes supply the current and the other two measure the voltage across the contacts.

Performing CTLM analysis on non-ohmic p-GaN layer is more complicated. Firstly, the slope and the intercepts in Eqn. (4.3) are no longer constant which changes the resistance as a function of drive current. This behavior is shown in Figure 4.8 which plots the sheet resistance, contact resistance, specific contact resistivity, and the resistivity of p-GaN contact layers for current range of -0.1 mA to 0.1 mA. Secondly, the condition that validated Eqn. (4.3) and Eqn. (4.4) no longer holds true near 0 mA. At zero current, the transfer length becomes comparable to the individual spacings in the CTLM pattern due to the resistive nature of p-GaN. As a result, all the plots in Fig. 4.8 have distinct peaks at 0 mA where the CTLM breaks down. The breakdown further evident in the resistivity of the

p-GaN layer which should remain constant being a material parameter independent of the drive current. Nevertheless, L_t approaches agreeable values at 0.1 mA and we can roughly evaluate R_{sh}, R_c, ρ_c, and ρ for p-GaN contact layers as ~230 kΩ/□, ~2.7 kΩ, ~0.01 Ω-cm^2, and ~1.8 Ω-cm, respectively. Independent optimization of the p-GaN layers for ohmic contacts is viable by examining the Mg-doping level and the activation/anneal conditions. However, it is much more effective to study the electrical properties after the fabrication of a complete VCSEL structure to incorporate the material changes brought by the processing steps.

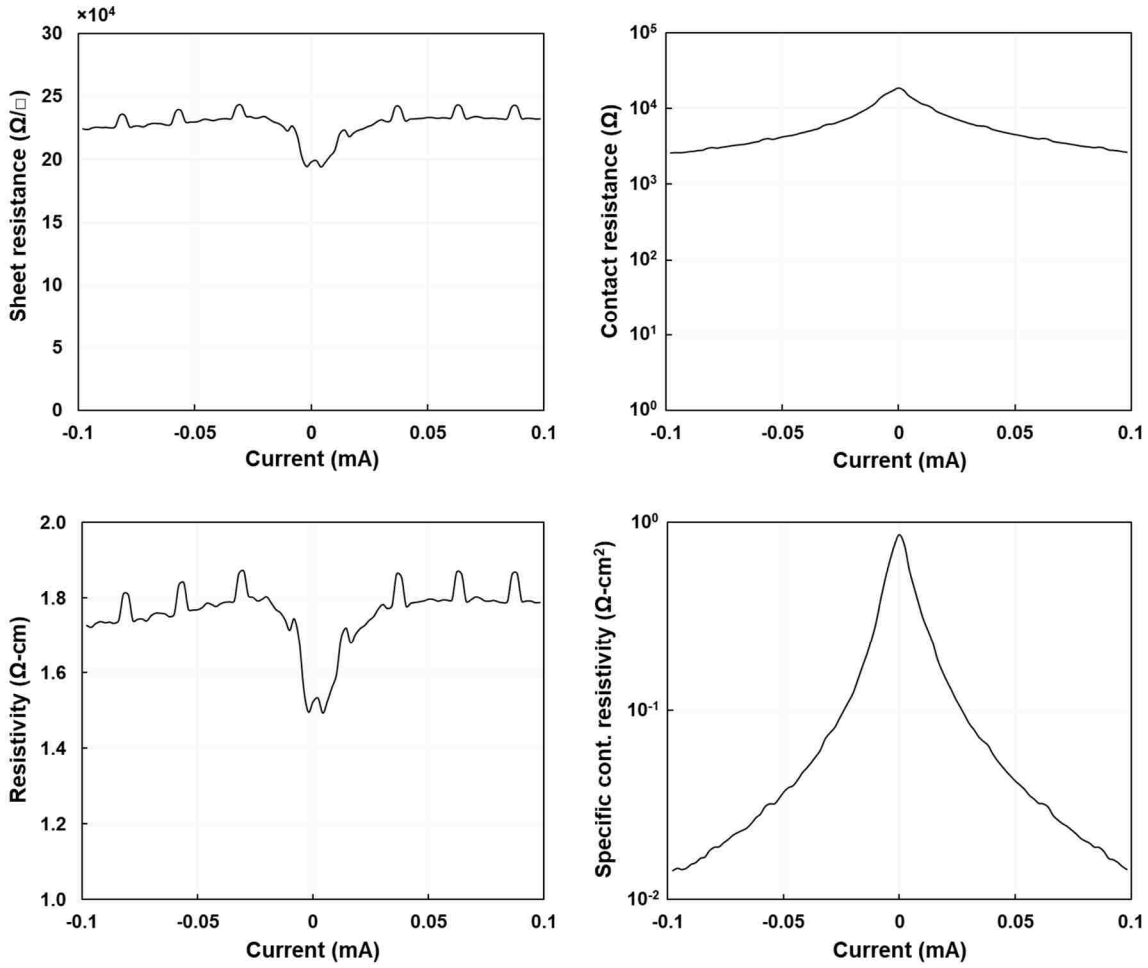

Figure 4.8. Sheet resistance, contact resistance, specific contact resistivity, and the resistivity of p-GaN contact layers vs. current plot extracted from CTLM measurements. The conditions for CTLM break down at low currents resulting in non-constant electrical properties.

4.2. Design and growth of the cavity

For an electrically injected VCSEL, it is necessary to redesign the cavity and the active region to accommodate the losses from the current injection layers. Not only is it important to place the absorbing layers at a longitudinal standing-wave null to lessen the affect cavity absorption, the cavity itself must be enlarged to account for internal heating in the devices. Moreover, it is crucial to verify layer thicknesses prior the VCSEL fabrications particularly since turn-around time is quite long (roughly 1 month).

4.2.1. Thickness calibration

Although the nanoporous DBRs are quite tunable, incorrect layer thickness can severely affect the emission uniformity and reduce the device performance. Hence, before the growth of the actual VCSEL epilayer, the growth rate of almost all layers including the DBRs, QWs, n-GaN, and p-GaN had to be re-calibrated. First, the growth rate of the bulk and nanoporous layers were calibrated using an alternating layer stack with increasing growth times for both layers. The sample was then EC etched using the same process as Section 2.2.2 and imaged using SEM to measure each layer thickness with time. Figure 4.9 (a) shows a cross-sectional SEM image of the calibration sample (Si concentration ~1×10^{19} cm^{-3}) and Fig. 4.9 (b) shows the associated average layer thicknesses with error bar versus growth time. The thicknesses changed linearly with time for both the doped and undoped layers. The growth rate for the nonporous bulk and the porous layer was ~9.4 nm/min and ~8.9 nm/min, respectively. Similarly, the growth rate of the n-GaN contact layer was calibrated which had a slightly different Si-doping concentration (~8×10^{18} cm^{-3}).

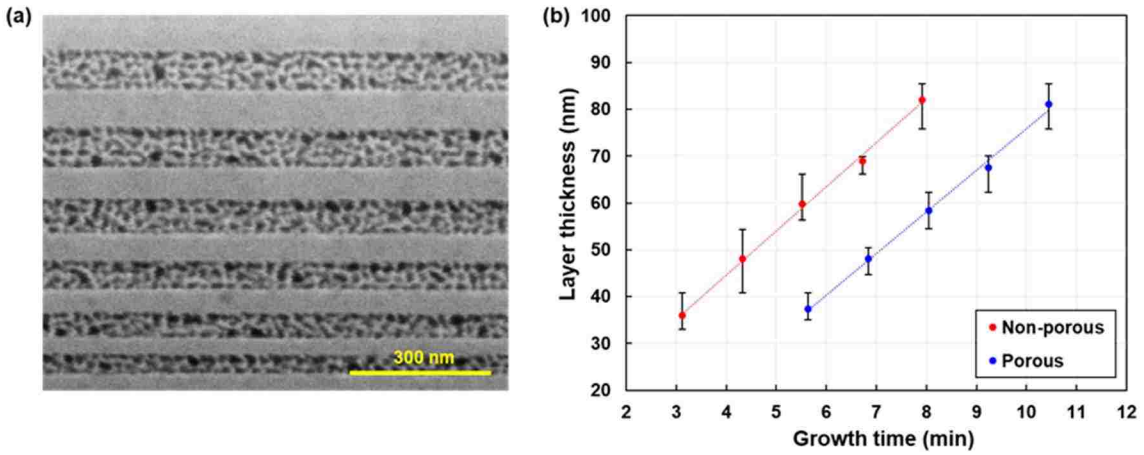

Figure 4.9 (a) Cross-section SEM image of nanoporous DBR sample. (b) Plot for measuring the growth rate of the porous and nonporous layers to correctly grow nanoporous DBR.

The InGaN (QWs) layers and AlGaN (EBL) are usually calibrated using high-resolution X-ray diffraction (XRD) measurements. A triple-axis Rigaku system at CINT enabled us to quantify the alloy composition and thickness by fitting the rocking-curves obtained from the measurement. In order to resolve the satellite peaks in the XRD measurements, separate InGaN and AlGaN XRD sample were prepared containing superlattice structures. The fittings are provided in Appendix A.2. Typically, the reactor conditions do not drift as much to cause significant changes in the material during an operation cycle. However, XRD calibration is compulsory after a maintenance or repair.

Knowing the exact composition of indium in InGaN to assess the emission wavelength is trivial. It is more efficient to perform a combined measurement of the PL and quick-test electroluminescence (EL) to determine the emission wavelength of the QWs. Quick-tests are done by soldering a small indium contact on the top and edge of the sample then probed to capture the emission spectrum. Likewise, the total thickness of the active region along with the p-side layers can be easily measured using PEC etching. The process of PEC etching is very similar to that of EC etching explained in Chapter 2. Instead of carriers

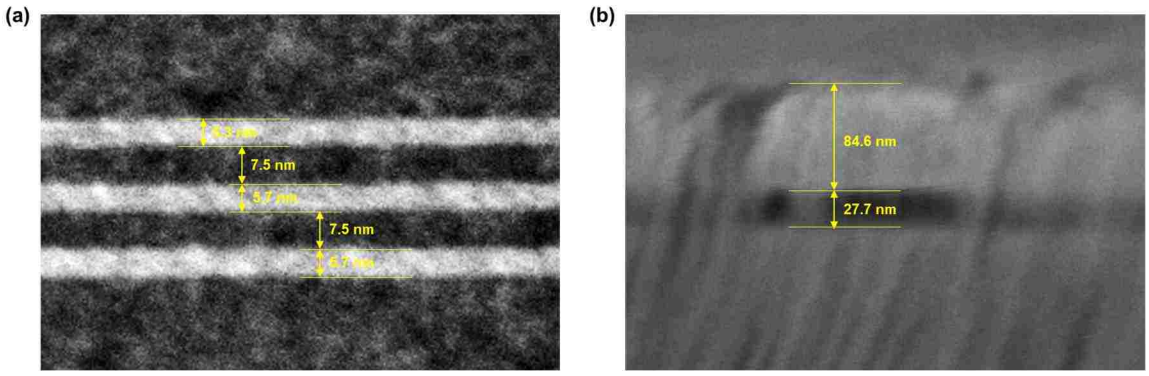

Figure 4.10 (a) TEM image of a calibration *m*-plane sample. (b) SEM image of a sample PEC etched in 1 M KOH for 1 min under a 405 nm laser source. The dark section is the undercut MQWs with a thickness of 27.7 nm and above that are the p-side layers which do not etch revealing a thickness of 84.6 nm.

being injected as in the case of EC etching, PEC etching relies on the generation of electron-hole pairs in selective layers which have a bandgap energy smaller than the energy of an incident light source. In this case, the light source was a 900 mW 405 nm laser diode. The sample is immersed in a solution of 1 M KOH and the upward band bending at the semiconductor/solution interface drives the holes to the surface to take part in an oxidation reaction to undercut InGaN. The advantage of this process is that it only requires a single mesa etch to expose the MQW sidewalls, and the undercut profile can be obtained very quickly with the high-power laser source (~1 min). The undercut itself can be used to measure the thickness of the active region which in-turn can be used to estimate the QW and barrier widths. It also acts as a marker layer to measure the p-side layer thicknesses (p-cladding). Ideally, TEMs should be used to accurately determine the QW and barrier thicknesses [calibration sample shown in Fig. 4.10 (a)], which is more tedious and time consuming. The PEC approach offers a very simple yet effective method to get a quick estimate. Figure 4.10 (b) illustrates an SEM image of a dummy sample with a total active region thickness of ~28 nm and a p-clad thickness of ~85 nm.

4.2.2. Cavity design

As per Eqn. (1.8) in Chapter 1, the gain in the active region must equal the total losses in the cavity for a VCSEL to reach threshold. Now with the advent of the aforementioned lossy layers, the total internal loss in the cavity has increased for which the cavity must be redesigned. Reiterating Section 3.2, not only must the MQWs be located at a standing-wave peak, the total thickness of the active region must be minimized to maximizes the overlap of each QW with the field to increase Γ_{enh}. Thus, the MQW GaN barriers were set to 2 nm which is the minimum limit of our MOCVD reactor. It is worth mentioning that, very thin barrier may result in insufficient carrier confinement in the MQWs leading to a reduced gain per well. However, for a given threshold modal gain, the three-parameter gain curve equation in Eqn. (1.11) is arguably the most important tool for determining the number of QWs to minimize the threshold current density. In principle, the slope of the gain curves (modal gain vs. current density) increases with increasing number of QWs while increasing the transparency current density (x-intercept of gain curves) as more carriers are required to fill up the QWs [9,186]. Thorough analysis of the material gain vs. current density has been performed by Farrell *et al*. using *m*-plane GaN EELDs of various cavity lengths [13,145]. This type of study is not feasible in VCSELs as devices of different cavity length cannot be fabricated on the same chip. We will simply adopt the model provided by Farrell *et al*. and modify it to suite our TMM simulation of the nanoporous VCSEL cavity.

Figure 4.11 (a) plots the gain curves using Eqn. (1.11) for 1-8 QWs with 2 nm barriers. Restating Eqn. (1.11) for convenience, $\Gamma g(J) \approx N_{qw}\Gamma_{qw}g_0 ln\left[(J+J_s)/\left(N_{qw}J_{tr}+J_s\right)\right]$, where N_{qw} is the number of QWs, Γ_{qw} is the average confinement factor per well, g_0 is the

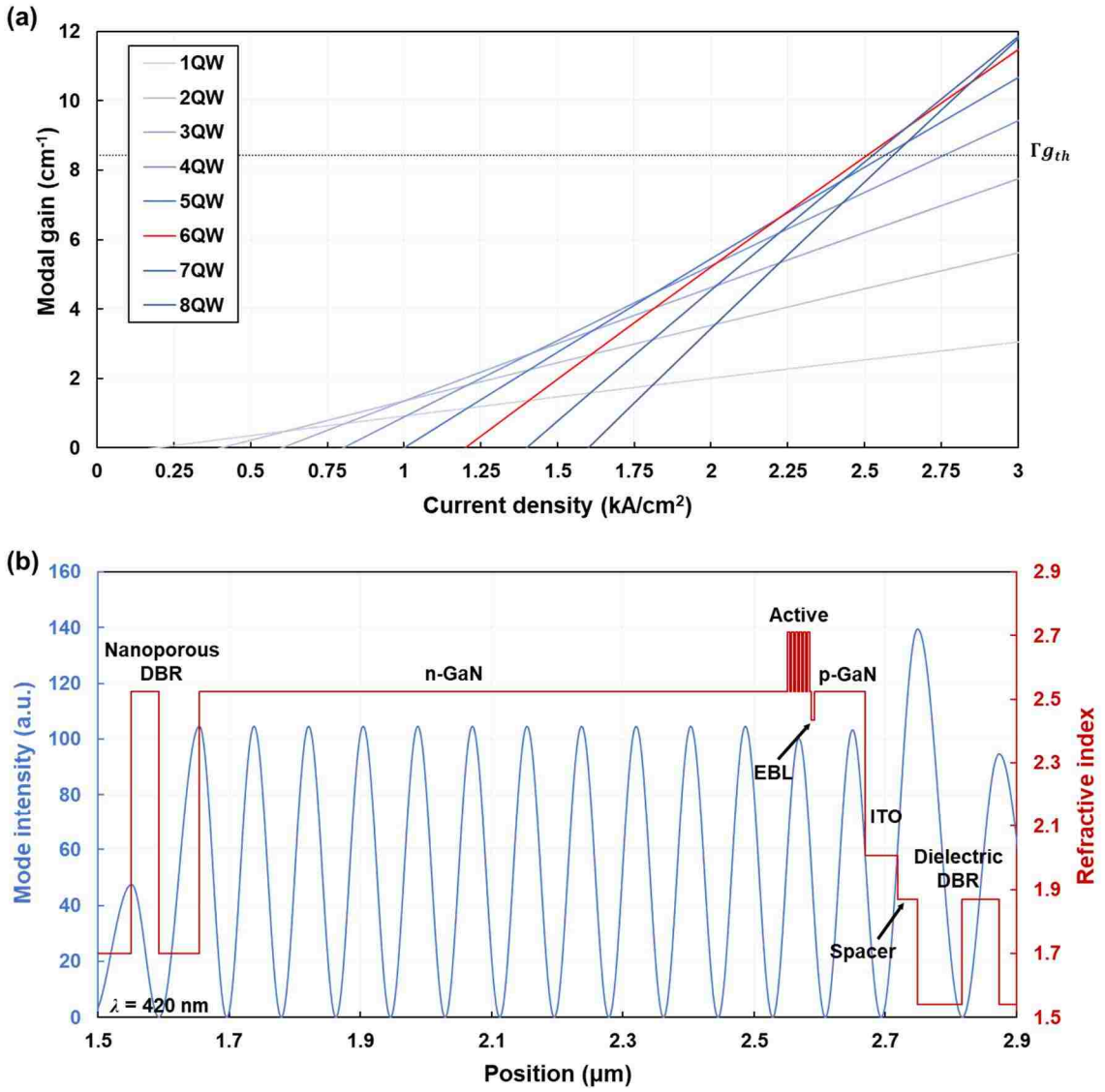

Figure 4.11 (a) Modal gain vs. current density plot for 1QW to 8QWs with a QW thickness of 4 nm and barrier thickness of 2 nm. TMM simulated threshold modal gain is overlaid on the plot to determine which design yields the lowest threshold current density. (b) TMM simulation of the cavity mode intensity and refractive index profile for a 6-QW design.

empirical gain coefficient, J_{tr} is the transparency current density per well, and J_s is a linearity fitting parameter [13]. The standing-wave and the refractive index profile of the cavity with an effective optical thickness of 8-λ ($L_{eff} \times n_{eff} \approx 1453$ nm $\times$ 2.26) is illustrated in Fig. 4.11 (b), with the QWs positioned at a longitudinal mode peak and the ITO at a null to maximize gain and minimize loss. The threshold modal gain of the cavity obtained from the TMM simulation was ~8.4 cm^{-1}. Overlaying this value on top of Fig. 4.11 (a), we see

that the lowest current density for this modal gain can be achieved with 6 QWs highlighted in red. It is important to keep in mind that the TMM analysis relies on literature reported estimates for most of the cavity losses. The actual internal loss of the layers may be much higher where a large number of QWs is favorable for lowering the threshold current density. At the same time, injection of carriers may be an issue for active regions consisting of several QWs. Increasing the number of QWs increases the probability of having one or more QWs to become devoid of carriers. These QWs will possess a negative gain and act as highly absorbing layers since the bandgap energy is the same as those QWs with positive gain. Either way, 6 QWs will be considered for this initial demonstration and future optimization of the active region will be carried out based on the performance of this first demonstration. The EBL layer consisted of a 5 nm p-doped $Al_{0.2}Ga_{0.8}N$ layer similar to previously reported *m*-plane VCSELs [78,80,81]. A thorough study on the EBL material composition and thickness may be quintessential for understanding the carrier injection dynamics in the active region.

An *m*-plane VCSEL sample was then grown with the epilayers consisting of a 3-µm-thick n-GaN template, 16 pairs of alternating undoped/n+GaN (Si-doping concentration ~1×10^{19} cm^{-3}) layers with thicknesses of 42 nm/62 nm for the bottom DBR, 495 nm of UID GaN for thermal spreading, a 200 nm n+GaN contact layer, a 200 nm n-GaN cladding layer, a six-pair $In_{0.1}Ga_{0.9}N$/GaN active region with thicknesses of 4 nm/2 nm emitting at ~407 nm, a 5 nm p-$Al_{0.2}Ga_{0.8}N$ electron blocking layer, a 63 nm p-GaN cladding layer, and a 14 nm p+GaN contact layer. Notice that the total p-clad thickness is 77 nm and the predicted Al-ion implant depth mentioned in Section 4.1.1 is less than 77 nm, so the SiO_2 was disregarded for ion implantation. The EL spectrum and *L-I-V* characteristics of

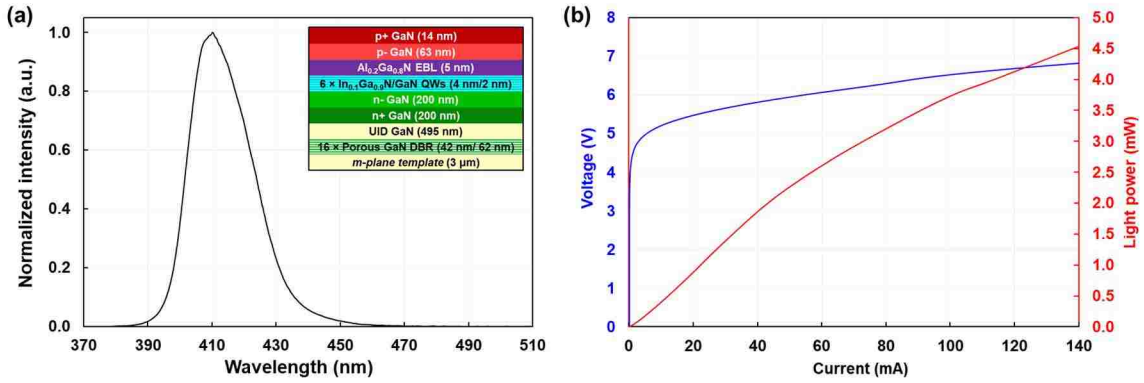

Figure 4.12 (a) EL spectrum of the nanoporous VCSEL sample. [Inset] Epilayer stack of the sample showing the layer thicknesses and the repetitions. (b) Quick-test LIV characteristics of the sample with a turn-on at 4.5 V and a 3.75 mW output power at 100 mA.

the sample is plotted in Fig 4.12 (a) and (b), respectively. The emission peak was at 410 nm caused by a slight rise in temperature during the growth of the QWs. Although this blue-shift is concerning, it can be beneficial in terms of temperature sensitivity of the VCSEL. Intentional detuning of the emission wavelength and/or the cavity have been studied in early VCSELs to attain stable operation [187,188]. The device turn-on was around 4.5 V with a series resistance of ~10 Ω. These values were slightly higher compared to our optimized *m*-plane LEDs, but the output power was much greater signifying higher quality epilayers. Moreover, both the turn-on voltage and series resistance can be improved with the optimization of the EBL and p-GaN layers.

4.3. Device fabrication

Following the growth, the sample was fabricated according the to the process flow depicted in Fig. 4.13 [189]. First, a mesa was etched (Mesa 1) using ICP etching to expose the n+GaN contact layer. Next, the sample was patterned with a Ti/Au hard mask to define the current apertures and sent to Leonard Kroko Inc. for Al-ion implantation. The implant process turn-around time is approximately 3 days. Aperture diameters of 5 µm, 10 µm, 15 µm, and 20 µm were defined in this step. After implantation, the Ti/Au hard mask was

removed in aqua regia. A second mesa with a depth of 400 nm was ICP etched (Mesa 2) and followed by a blanket e-beam deposition of 150 nm SiO_2 to protect the active region and contact layers during the porosification step of the nanoporous DBRs. Next, deep trenches aligned along the *c*-direction were etched to expose the sidewalls of the DBR stack. Following this, the DBRs were EC etched for 14 hours to selectively porosify the highly doped n-type DBR layers using a bias voltage of 5 V at 100 rpm stirring. Complete porosification was confirmed when the two lateral etch fronts along the *a*-direction met at the center of the trench. Next, the blanket SiO_2 was stripped in buffered HF and a patterned layer of SiN_x was deposited across Mesa 1 and the trench to passivate the sidewalls of the active region and the nanoporous DBRs. Passivation of the DBR sidewalls was required to prevent the build-up of undeveloped PR from the following consecutive steps. ITO of 50 nm was e-beam deposited and annealed under nitrogen ambience at 550˚C for 15 minutes, after which the p-metal and n-metal were deposited which consisted of Ti/Au (20 nm/300 nm) and Ti/Al/Ni/Au (20 nm/100 nm/50 nm/300 nm), respectively. Finally, a 30-nm-thick SiN_x cavity spacer and the top dielectric DBR were blanket deposited using PECVD then patterned and etched down using RIE. The top DBR consists of 25 pairs of alternating ¼-λ SiO_2 and SiN_x. Excluding calibration, the total processing time from the growth of the epilayers to the final fabrication step takes roughly 3.5 week. A cross-sectional schematic and SEM images of the completed VCSEL structure is illustrated in Fig. 4.14. Overall, the entire fabrication process is relatively simple with a straightforward device design utilizing standard micro-fabrication techniques. As will be established in the next section, this process results in a high yield of devices [189].

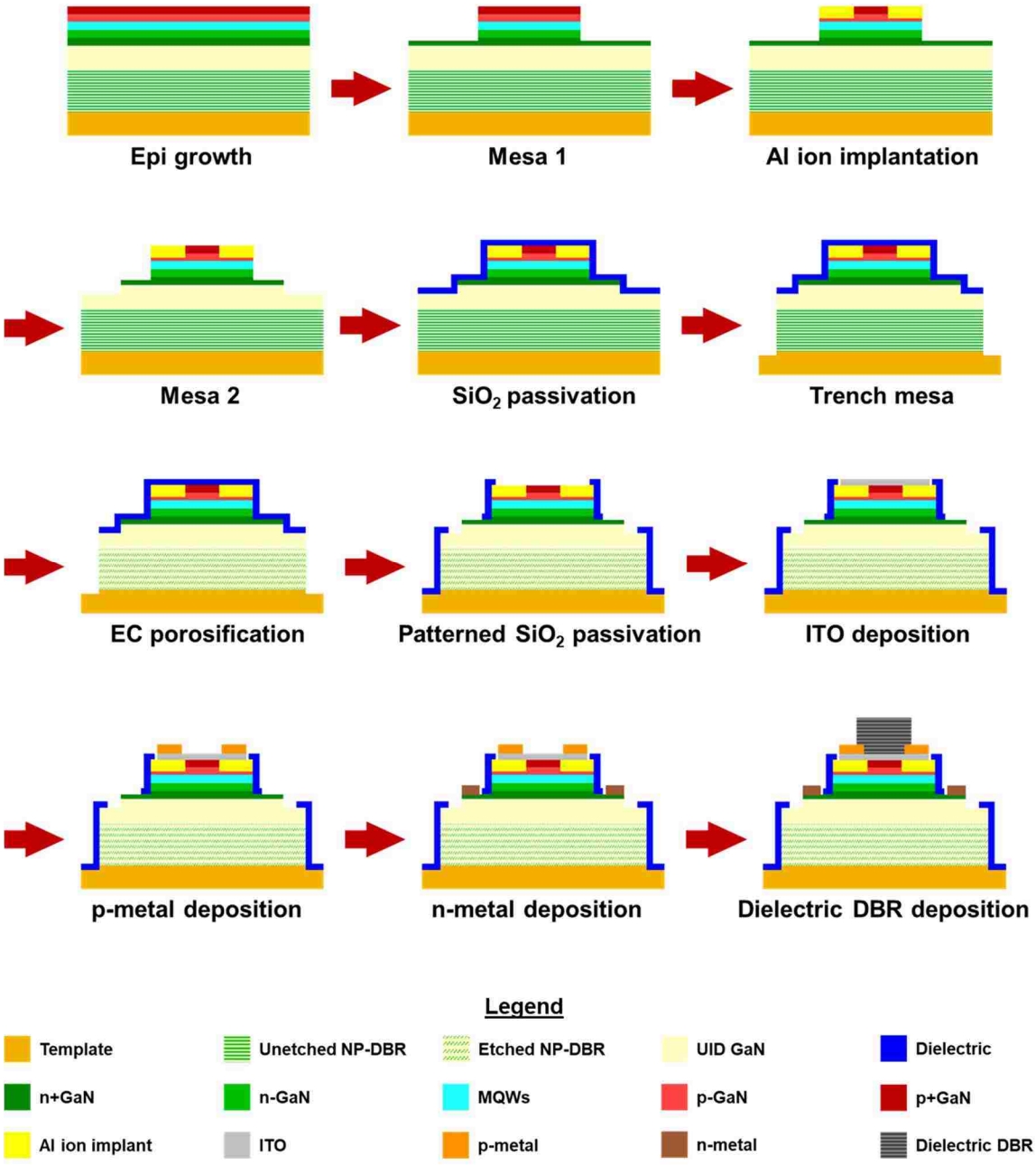

Figure 4.13. Processing steps for the fabrication of the *m*-plane nanoporous VCSEL.

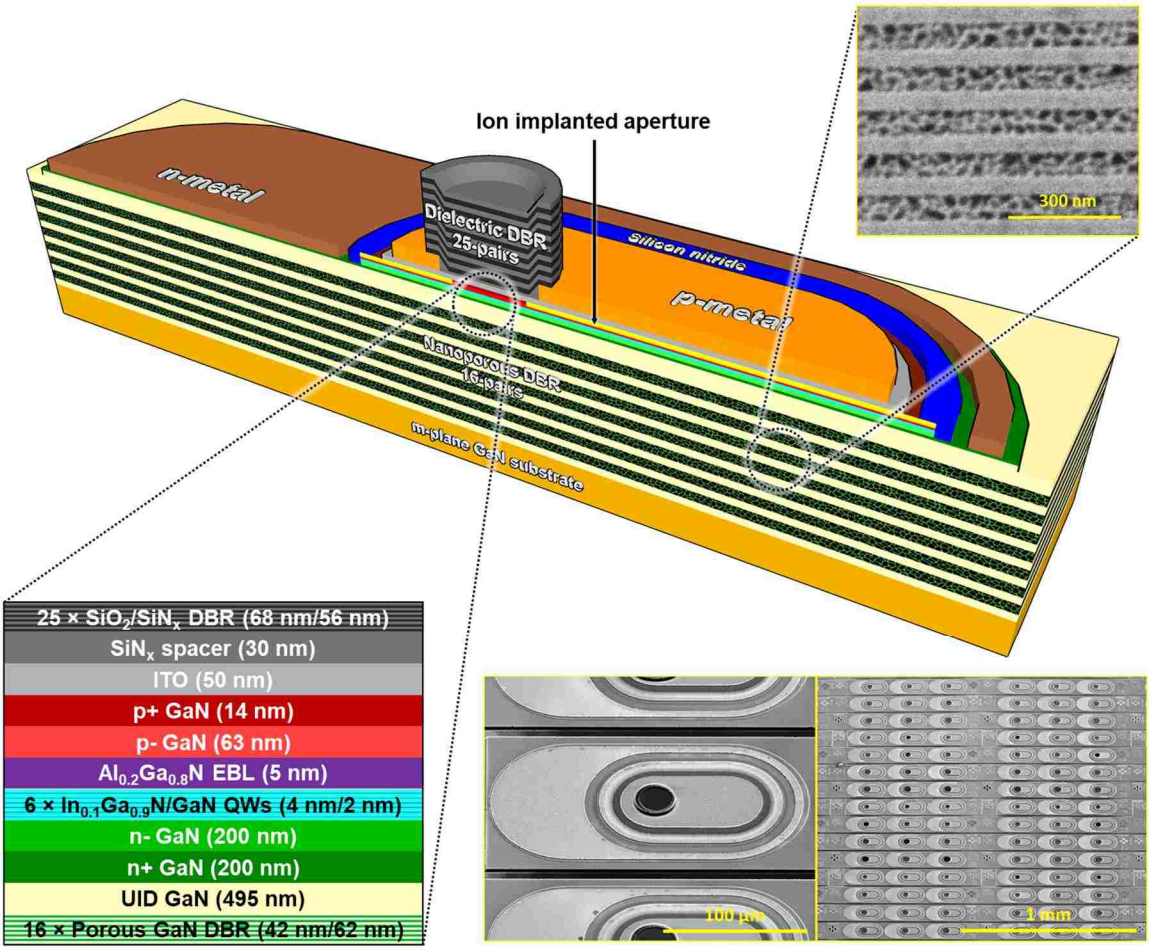

Figure 4.14. Cross-sectional schematic of the *m*-plane nanoporous VCSEL showing the epilayer stack. Also shown are the SEM images of the bottom nanoporous DBR and the angled topographic view of the VCSEL structure.

4.4. VCSEL characterization

Characterization of the nanoporous VCSELs were performed under pulsed conditions with a pulse width of 50 ns and a duty cycle of 0.05% at RT. Such narrow pulse widths will allow the devices to be driven at very high current densities without catastrophically damaging the VCSELs through internal heating. High current density operation is often required in VCSELs, particularly for first demonstrations, where the threshold current density may be quite high. One of the issues faced while testing with 50 ns pulse widths was the limited detection capability of our high-speed detector. Ideally, a square current

pulse should produce an identical square voltage and light pulse with some hysteresis from the circuit [see Appendix A.6 for pulsed setup]. Unfortunately, the light output power at 50 ns pulses fell below the detection limit of our high-speed detector, resulting in the light signal to remain zero. This was solved by using a slow yet highly sensitive Si detector to measure the output power levels down to nanowatt scales using an external power meter. In this method, the measured light was the time average of the total detected light across the entire period of the pulse, including the section when the VCSEL remained off. The exact light output power within the pulse was calculated using the measured power meter reading divided by the duty cycle of the pulsed measurement (0.05%).

4.4.1. Optoelectronic characteristics

Figure 4.15 (a) shows the light-current density-voltage (*L-J-V*) characteristics of a VCSEL with a 20-μm-diameter aperture measured from the top. The onset of lasing is indicated by a clear non-linear 'kink' in the *L-J* curve. The threshold current density and threshold voltage for this particular device are ~20 kA/cm^2 and 9.6 V, respectively. One might expect a low mirror loss to be associated with a low threshold current density. However, we do not see this in our devices and other demonstrations of electrically injected VCSELs report threshold current densities less than 10 kA/cm^2. Although the reason for such high threshold is unclear, it is likely the combined effect of poor injection efficiency with misaligned cavity mode. A mode offset can lead to increased absorption in the ITO and/or reduced enhancement factor as shown in the TMM simulation shown in Fig. 4.15 (b). The threshold current density will be explored again later in the section. Nevertheless, the maximum output power from the top of the VCSEL was measured to be around 1.5 mW, which is higher than any previously reported *m*-plane GaN-based VCSEL [189].

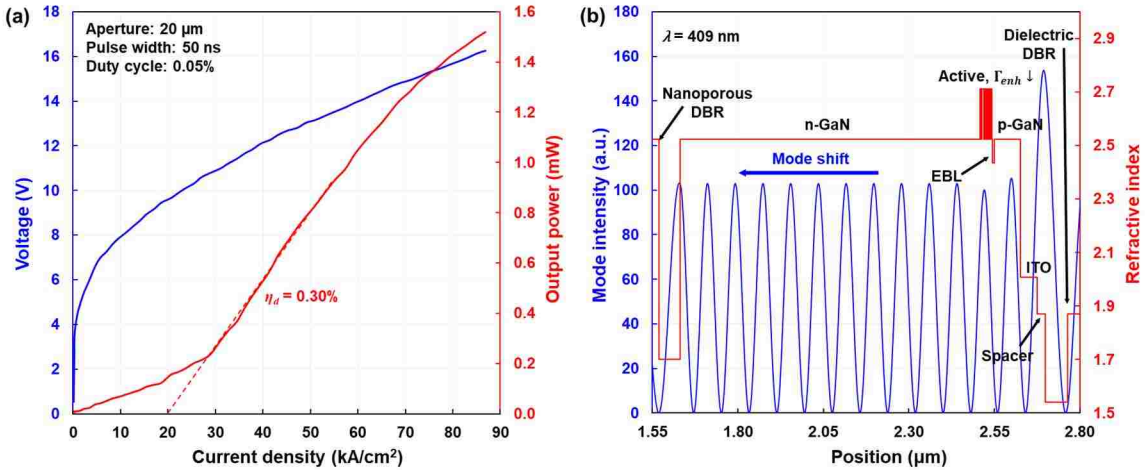

Figure 4.15 (a) *L-J-V* plot of a 20-μm-diameter nanoporous VCSEL under pulsed operation. (b) Mode intensity and refractive index profile of the VCSEL showing the shift in the cavity mode, where Γ_{enh} reduces from ~1.7 to 1.64.

Emission collection from the bottom was also attempted after polishing the backside of the wafer to check if higher output powers can be achieved from the same device. However, the amount of stimulated emission collected was too small to be well detected even by the high sensitivity detector, although weak stimulated emission appeared in the spectrum. The ratio of the output powers from either facet can be estimated by the F-factor stated in Section 1.1.3 calculated from the reflectance of the cavity mirrors [9]. It is difficult to measure the exact mirror reflectance of the bottom nanoporous DBR. However, the F-factors can be determined using the VAT refractive indices of the bottom nanoporous DBR and the measured reflectance of the top dielectric DBR. Figure 4.16 (a) shows the reflectance spectrum obtained from a dummy DBR sample deposited alongside the actual VCSEL samples. At 409 nm, the peak reflectance of the dielectric DBR is 99.657%. Using this, Eqn. (1.13) and Eqn. (1.14) is plotted in Fig. 4.16 (b) as a function of r_{bottom} with α and L being 10 cm^{-1} and 330 μm, respectively. Note that $F_{top} + F_{bottom} \neq 1$ when substrate absorption/Fresnel loss is considered in Eqn. (1.14). Calculating F_{top} from Eqn. (1.12), Eqn. (1.27), and Fig. 4.15 (a) at 409 nm yields a value of 0.9492, which corresponds

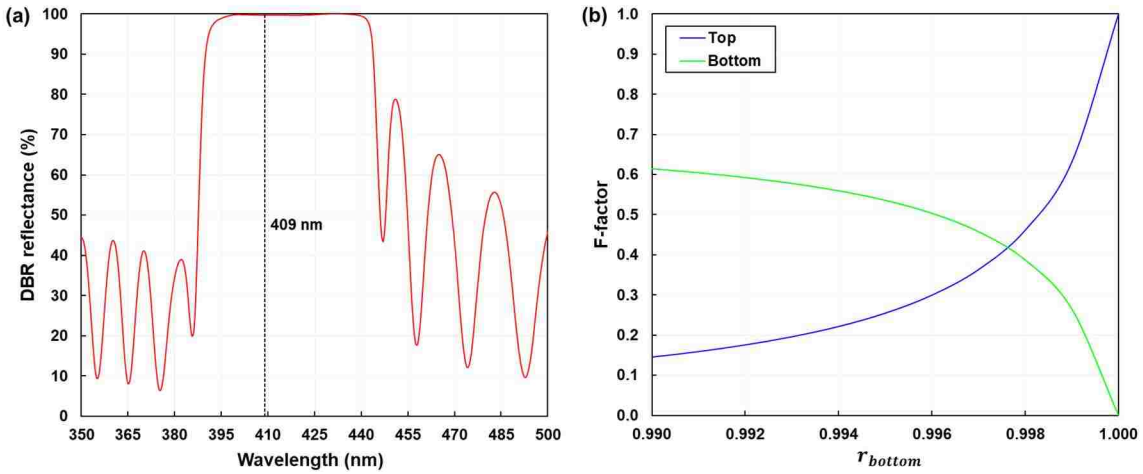

Figure 4.16 (a) Top dielectric DBR reflectance spectrum showing a peak reflectance of 99.7% at 409 nm. (b) Plot of F_{top} and F_{bottom} as a function of estimated r_{bottom}, showing that R_{bottom} must be at least 99.7% to emit equal power from both facets.

to F_{bottom} of 0.0376 in Fig. 4.16 (b). This implies that most of the stimulated emission is escaping through the top DBR and that the bottom nanoporous DBR mirror has a very high reflectance (>99.9%) as evident by the low F_{bottom}. Mirror reflectance above 99% from the nanoporous DBRs have been observed in some regions when performing μ-reflectance, but the reflectance was non-uniform due to pore agglomeration [149]. Hence, a more uniform and conservative lower reflectance of 98.7% was reported. Given the previous high reflectance observations and the low output power from the backside, the VCSELs reported here must have at least 99.7% reflectance in the bottom DBR to get equal power from the backside. Therefore, the nanoporous DBRs must have a mirror reflectance >99.9% which agrees with the output power characteristics presented here. The combined mirror reflectance from both DBRs result in a mirror loss (α_m) of ~13.8 cm^{-1}.

Applying the gain curve from Section 4.2.2 to the measured threshold current density provides valuable insight into the threshold modal gain and the cavity losses of the VCSEL. To accommodate the 20 kA/cm^2 threshold current density, the 6-QW gain curve from Fig.

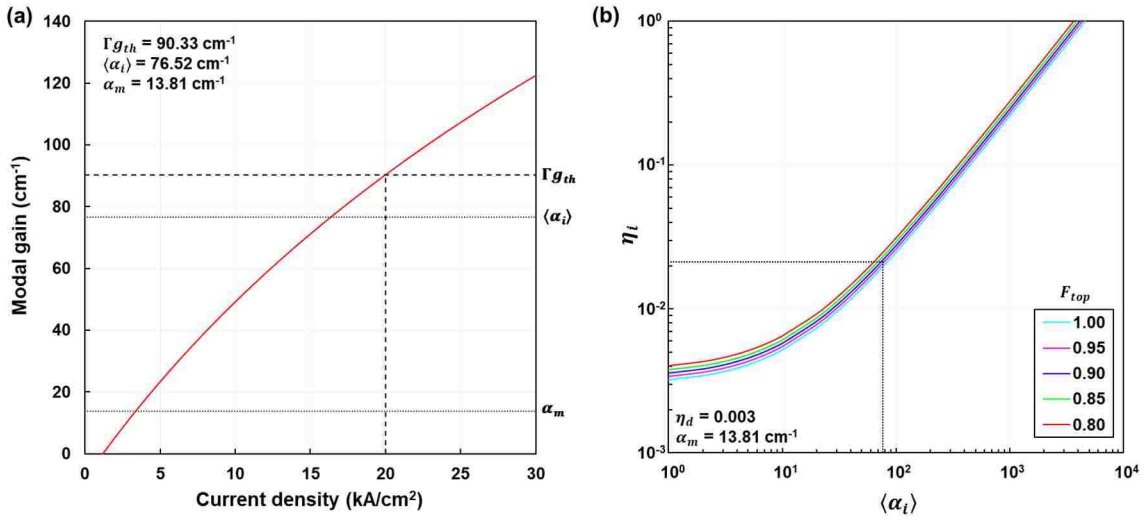

Figure 4.17 (a) Gain curve showing the threshold modal gain at 20 kA/cm^2 with α_m and $\langle\alpha_i\rangle$ overlaid on the plot for comparison. (b) Plot showing the effect of the calculated $\langle\alpha_i\rangle$, α_m, η_d, and F_{top} on the injection efficiency η_i.

4.11 (a) was extended to give a threshold modal gain of 90.33 cm^{-1}, as shown in Fig. 4.17 (a). According to Eqn. (1.11), in order to decrease the threshold current density, the number of QWs in the active region must be increased. The high Γg_{th} is associated with the shifting of the longitudinal mode in Fig. 4.15 (b) for which the QWs are no longer centered at the mode peak. The shift also misaligns the ITO layer away from the null, resulting in a high $\langle\alpha_i\rangle$ of 76.5 cm^{-1}. Overlaying the calculated values of α_m and $\langle\alpha_i\rangle$ in Fig. 4.17 (a), we see that the internal loss accounts for ~85% of the total loss in the VCSEL, assuming there is negligible scattering loss. Therefore, future VCSEL designs should not only confirm correct epilayer thicknesses but also consider replacing the lossy ITO intracavity spreading layer with the more conductive and transparent GaN-based TJs [81].

A differential efficiency (η_d) of ~0.3% was calculated from the slope of the *L-J* curve in Fig. 4.15 (a). As per Eqn. (1.12), η_d is depends on the F-factor F_{top}, the injection efficiency η_i, the mirror loss α_m, and the total internal loss $\langle\alpha_i\rangle$. To determine the root cause of such low η_d, Fig. 4.17 (b) plots the injection efficiency η_i as a function of the

internal loss $\langle \alpha_i \rangle$ for a range of different F_{top} values by setting the measured values of η_d and α_m as constants. F_{top} was previously calculated to be ~0.95 and changing its value has a negligible effect on η_i for any given $\langle \alpha_i \rangle$. Hence, the internal loss evaluated from Fig. 4.17 (a) corresponds to an injection efficiency of ~2%! Typical injection efficiencies for *m*-plane devices are greater than 80%. The extremely small value of η_i in the nanoporous VCSEL is likely associated with the 5 nm p-$Al_{0.2}Ga_{0.8}N$ EBL. It is possible that the Al-composition and/or the EBL width may be too high, preventing the injection of carriers into the active region. Though the EBL was calibrated and grown to the exact specification of earlier demonstrations of *m*-plane GaN VCSELs, the conditions may not be optimal for our specific epitaxial structure. A thorough in-depth analysis on the doping, alloy composition, and thickness of the EBL is vital for understanding the injection of carriers into the active region.

The series resistance R_s was measured to be ~25 Ω from the *J-V* plot in Fig. 4.15 (a). Most of the voltage drop would occur in the p-side contacts as we have seen earlier in Section 4.1.2. Therefore, it is also important to know the spreading resistance $R_{spreading}$ of the ITO layer. The spreading resistance can be estimated using the model provided in [20] for circular-shaped contacts, where $R_{spreading}$ is given as

$$R_{spreading} = \frac{\rho}{2\pi t}\int_{r_1}^{r_2}\frac{1}{r}dr = \frac{\rho}{2\pi t} ln\left[\frac{r_2}{r_1}\right]. \quad (4.5)$$

Here, ρ is the layer resistivity, t is the layer thickness, r_1 is the radius of the aperture, and r_2 is the radius of the metal contact. The p-side spreading resistance within the ITO was estimated to be ~13 Ω which is almost half of the total series resistance. The spreading resistance can be improved dramatically by incorporating a GaN-based TJ in place of the

ITO as a current spreading layer [81,90] lowering $R_{spreading}$ to ~3 Ω, based on the reported lateral resistivity of the TJs. Additionally, increasing the thickness of the n+GaN contact layer on the n-side and increasing the doping concentration would further reduce the resistance. However, a trade-off exists as increasing the doping concentration can contribute to free-carrier absorption in the cavity.

Figure 4.18 shows the emission spectrum at four different pump currents below and above threshold, and the corresponding near-field microscope images of the aperture region. A longitudinal mode was observed at 408.7 nm, with a FWHM of ~0.6 nm at a current of $2I_{th}$, but for an independent single peak, the linewidths were <0.3 nm. A secondary peak located at 409.1 nm is not necessarily indicative of higher order longitudinal modes because the effective cavity length ($L_{eff} \approx 1.45$ μm) results in a mode spacing of ~25.5 nm, allowing only a single longitudinal mode to exist within the gain bandwidth based on the intended design. However, the emission characteristics in Chapter 3 have indicated that non-uniformities in the optical cavity resonance due to localized changes in the effective refractive index of the nanoporous layers can lead to locally

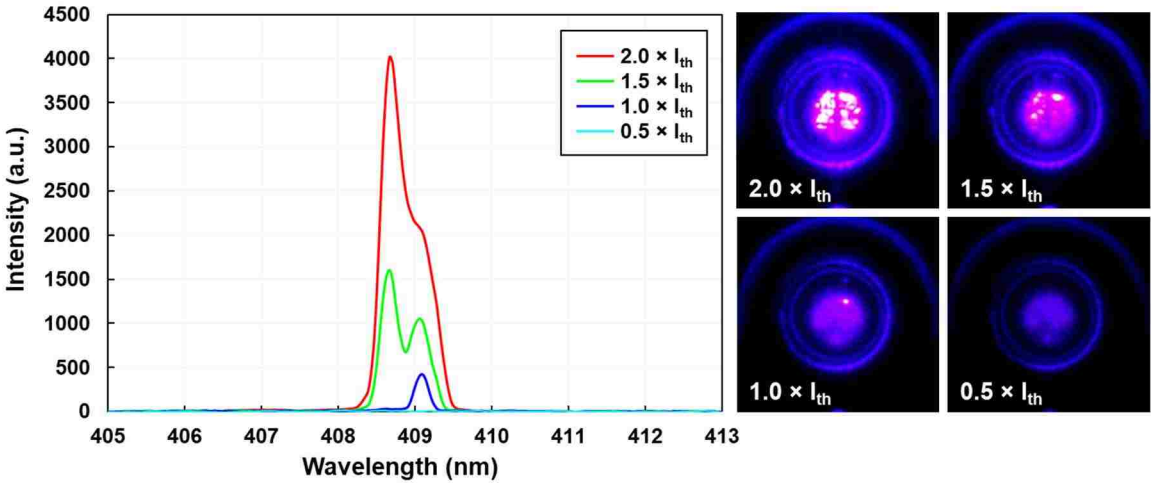

Figure 4.18. Emission spectrum under various pump currents and the corresponding near-field images of the aperture region.

different single-longitudinal modes with same mode number but slightly different wavelengths, resulting in multiple peaks within the lasing spectrum [159,160]. As shown in the near-field images, a single spot at 409.1 nm starts lasing near threshold. Then at higher currents, the mode at 408.7 nm dominates the stimulated emission in the aperture. The filamentary nature of the emission across the aperture is commonly observed in III-nitride VCSELs, but its origin is not well understood [78,80,81]. Previous reports have implicated poor transverse optical confinement, inhomogeneous current spreading of the ITO, and/or localized variations of the contact resistance despite having uniform layer refractive indices inside the cavity [92,190]. Higher order transverse modes in large diameter apertures, coupled with non-uniform injection, might also result in similar emission patterns, but the origin of the filamentation in the reported VCSELs requires further study. The discrete vertical divide across the lasing aperture observed in the near-field image at $2I_{th}$ is the intersection of the nanopore etching fronts from the positive and negative a-directions, forming a break in the aperture. Modifications to the aperture location on the mesa or etching from the c-direction are expected to solve this issue in future designs.

While VCSELs fabricated on c-plane GaN exhibits randomly polarized emission from device-to-device, nonpolar m-plane VCSELs emissions are polarization locked along the a-direction for all devices due to the anisotropic in-plane gain discussed in Section 1.2.4. The polarization characteristics of the nonpolar nanoporous VCSELs are shown in Fig. 4.19. Figure 4.19 (a) shows a polar plot of the normalized output power (measured with an optical power meter) as a function of the polarizer angle for three such devices with polarization-pinned emission in the a-direction. Figure 4.19 (b) shows the spectrometer

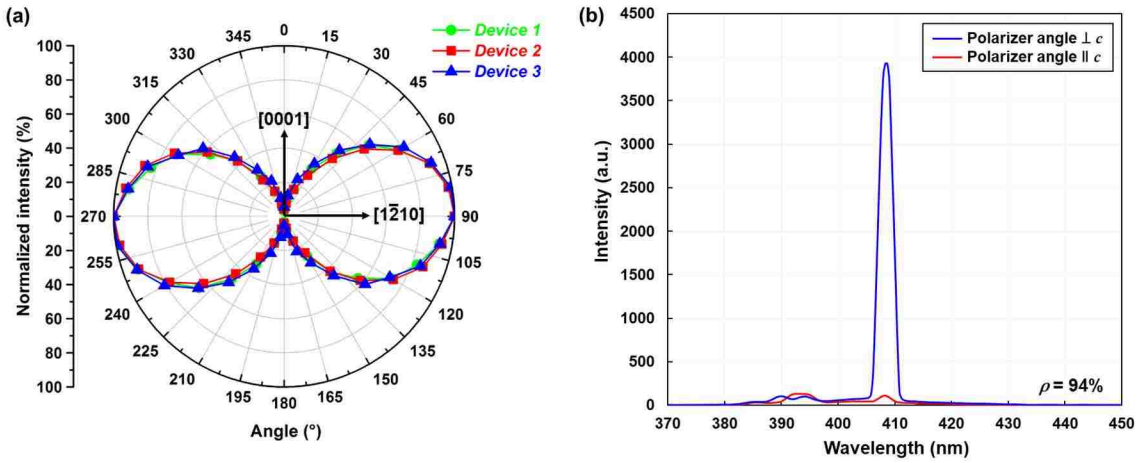

Figure 4.19 (a) Polar plot showing stable polarization-pinned emission along [$1\bar{2}10$] for three devices in different parts of the sample. (b) Spectrum when the polarizer angle is perpendicular and parallel to the *c*-direction.

measurement of the 20-µm-aperture diameter device with the polarizer angle parallel and perpendicular to the *c*-direction. The maximum stimulated emission intensity was observed when the polarizer angle was aligned perpendicular to the *c*-direction (along *a*-direction [$1\bar{2}10$]) and the intensity dropped to spontaneous emission levels when the polarizer angle was parallel to the *c*-direction [0001]. Using Eqn. (2.7), the polarization ratio was calculated to be ~94%. The slight drop from 100% polarization ratio is caused by the power meter collecting remnants of spontaneous emission and scattered light. The spontaneous emission can be completely removed from the polarization measurement if the calculation is performed using the integrated spectrum of Fig. 4.19 (b). Note that many other devices were also tested, all of which exhibited the same polarization-pinning characteristics, eliminating any concern of optical scattering from the nanoporous DBRs.

4.4.2. Thermal performance analysis

Temperature-dependent characterization of the VCSEL was performed on a temperature-controlled stage ranging from RT to 333 K in 10 K increments. Light output power versus drive current curves for five different temperatures are plotted in Fig. 4.20

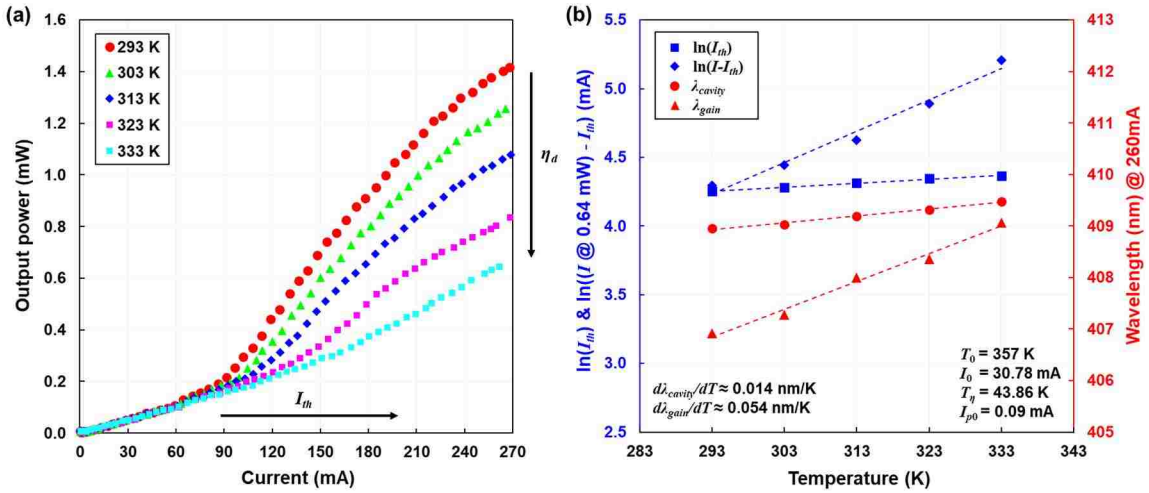

Figure 4.20 (a) Output power vs. drive current at different stage temperatures. (b) Natural-log of the threshold and drive current, and the wavelength shift for the gain peak and cavity mode, as a function of temperature. (dashed lines) Corresponding linear fits.

(a). As a general trend, the maximum output power is inversely proportional to temperature, while the threshold current increases with temperature. These trends occur because the peak gain is reduced by non-radiative carrier losses at elevated temperatures due to increased carrier leakage and Auger recombination [9,191–194]. Choosing the peak output power at the highest stage temperature (0.64 mW) from Fig. 4.20 (a), the threshold current and the current above threshold at 0.64 mW for different temperatures is plotted in Fig. 4.20 (b). The sensitivity of the currents to temperature can be determined using the empirical relations,

$$I_{th} = I_0 e^{T/T_0} \tag{4.6}$$

$$I - I_{th} = I_{p0} e^{T/T_\eta} \tag{4.7}$$

where the first equation signifies the threshold current dependence on temperature, while the second equation denotes the temperature dependence of the drive current I above threshold [9]. Here, T is the stage temperature in K, I_0 and I_{p0} are fitting parameters, and T_0 and T_η are the characteristic temperatures of the VCSEL. The values of I_0, I_{p0}, T_0, and

T_η are ~30.7 mA, ~0.09 mA, ~357 K and ~44 K, respectively. The high value of T_0 implies that the effect of temperature on the threshold current is relatively insignificant. This behavior is not uncommon in VCSELs where the gain offset parameter ($\Delta\lambda = \lambda_{gain} - \lambda_{cavit}$) is slightly negative at room temperature [188]. Figure 4.20 (b) also shows the peak gain and the cavity mode wavelength as a function of temperature, where $\lambda_{cavity} > \lambda_{gain}$ at 293 K. As temperature increases, λ_{gain} shifts to longer wavelengths with the overall gain declining from thermal redistribution of carriers [191,195,196]. Similarly, λ_{cavity} also increases due to the slow change of the effective cavity index with temperature [98]. Typically, $\frac{d\lambda_{gain}}{dT} > \frac{d\lambda_{cavity}}{dT}$ and from Fig. 4.20 (b) obtained values of $\frac{d\lambda_{gain}}{dT}$ of ~0.054 nm/K and $\frac{d\lambda_{cavity}}{dT}$ of ~0.014 nm/K, which are comparable to numbers reported in literature [88,98]. Therefore, at some elevated temperature, $\Delta\lambda$ approaches zero when the peak gain shifts and aligns with the cavity mode enabling stable VCSEL operation over a broad range of temperatures.

The preliminary thermal results hinted at the possibility of CW operation of the nanoporous VCSELs. Unfortunately, the devices broke down when the duty cycle was raised beyond 3%. In order to determine the cause of this breakdown, thermal properties of the nanoporous VCSEL structure had to be studied. Obviously, the air voids in the nanoporous layers will significantly reduce the thermal conductivity of GaN, but presence of stacked layers in the DBR would lessen the effect as a whole. To obtain the actual thermal conductivity of the nanoporous layers, a wafer was grown consisting of a 1-µm-thick n-GaN layer followed by a thin 50 nm undoped GaN cap and cleaved into two pieces. One of the samples will be unetched used as a bulk GaN reference (sample A), and the

other was fabricated with porous doped layer to a porosity similar to the VCSEL DBR porosity of ~66% (sample B). The thermal conductivity measurements on the two samples were performed by Dr. David Cahill's research group at the University of Illinois using time domain thermo-reflectance (TDTR) [197–199]. In TDTR, the sample is heated with a modulated laser source while another laser measures the changes in reflectance to calculate the thermal conductivity of the material. It is also possible to extract the changes in thermal conductivity for different layer porosities, however, the validity of such extrapolation is questionable given that it was based on only two data points. Figure 4.21 (a) plots the trend in thermal conductivity as a function of the porosity and also contains the SEM cross-sections of the two samples. Here, the measured thermal conductivity of sample A and sample B were 170 W/mK and 2.9 W/mK, respectively. The bulk GaN thermal conductivity was similar to those reported in literature [112,200] but the value decreased drastically for the porous sample. Figure 4.21 (a) also plots the changes in index contrast as function of the porosity. At a porosity of 66%, Δn at 409 nm is ~0.84 indicating room for lowering the porosity to improve thermal conductivity. Doing this, however, will

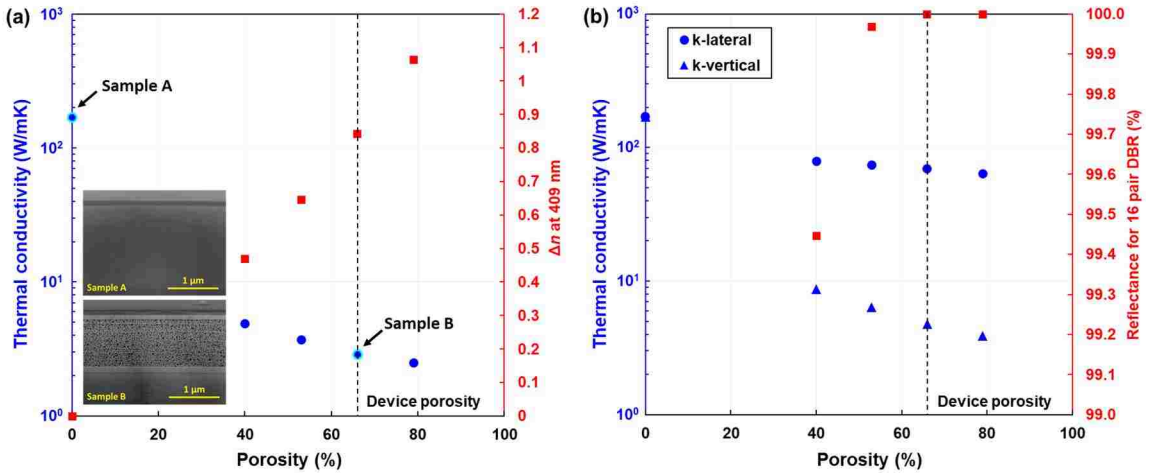

Figure 4.21 (a) Thermal conductivity of sample A and sample B using TDTR performed at UIUC vs. porosity, also shows the refractive index contrast obtained from VAT. (b) Corresponding anisotropic thermal conductivities and peak reflectance of a 16-pair DBR stack used in the VCSELs.

required more DBR pairs to maintain the same reflectance. The data in Fig. 4.21 (a) can be converted to simulate the 16-pair DBR structure used in the nanoporous VCSELs. Note that modeling the thermal conductivities of stacked layers requires extra attention as multi-layer stacks experience enhanced scattering by interface phonons due to the thermal boundary resistance at each interface [114]. Hence, stacked layers can have reduced thermal conductivity anisotropic values compared to the same materials in bulk. Therefore, to accurately model these layers, an effective thermal conductivity was used, with the lateral (k_l) and vertical (k_v) anisotropic thermal conductivities given by [201,202],

$$k_l = \frac{d_1 k_1 + d_2 k_2}{d_1 + d_2} \tag{4.8}$$

$$k_v = \frac{d_1 + d_2}{d_1/k_1 + d_2/k_2}. \tag{4.9}$$

Here, k_1, k_2 and d_1, d_2 are the thermal conductivities and the thicknesses of the alternating DBR layers, respectively. The changes in k_l and k_v with respect to porosity is shown in Fig. 4.21 (b). At 0% porosity when the DBR can be considered bulk GaN, the thermal conductivity is isotropic with a value of 170 W/mK. At the device porosity of 66%, k_l is 69.7 W/mK and k_v is 4.78 W/mK, implying that most of the heat will dissipate laterally as opposed to vertically. This is understandable since phonons travelling vertically will experience more interfaces and insulating layers in the vertical direction. Figure 4.21 (b) also plots the peak reflectance of the DBR versus the layer porosity showing that at the device porosity of 66%, the reflectance is almost 100%. The porosity can be reduced to 50% while still maintaining a reflectance >99.9% to help improve k_v, though there is not much change in k_l.

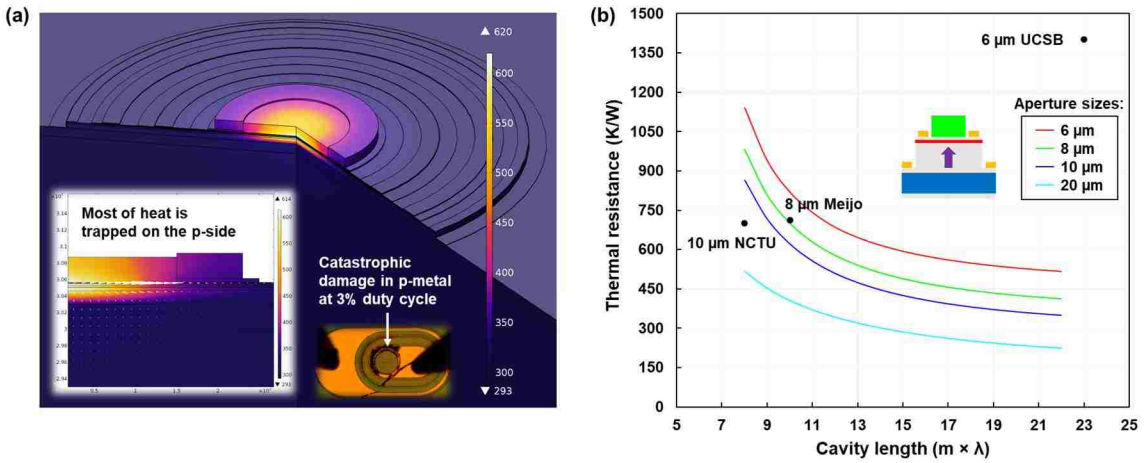

Figure 4.22 (a) Axisymmetric COMSOL™ simulation of the nanoporous VCSEL showing the temperature profile and (inset) heat flow in the cavity layers. It also shows a microscope image of a device with p-metal damage due to heating at 3% duty cycle. (b) Plot of Z_t vs. cavity length for the nanoporous VCSEL with different aperture sizes. Overlaid are the thermal resistance of reported CW-RT VCSEL by NCTU [88], Meijo-Stanley [71], and UCSB [89].

Now that we know the thermal conductivity of the nanoporous DBR, we can model the entire VCSEL structure to estimate the thermal resistance Z_t. Measuring Z_t experimentally using Eqn. (1.29) was not possible since CW operation could not be achieved. Hence, thermal analysis was carried out using a steady-state heat dissipation model to generate the thermal profile within the VCSEL. Due to the symmetry of the aperture of the device, a 2-D axisymmetric model was used to reduce the computation time, while still representing the lateral heat transfer within the device layers accurately. A single small device is examined in a considerably large domain size of 500 µm by 300 µm to prevent erroneous data, since FEM simulations in COMSOL™ typically depend strongly on the simulation domain [203]. The resistive component of the heat generated from the epilayers is negligible compared to the nonradiative recombination component as the wall-plug efficiencies of the devices are quite low. Thus, joule heating was neglected and an apertured non-radiative heat source within the active region was assumed with uniform current spreading. The heat is predominately transferred by conduction so a heat diffusion model

for conduction was used. Figure 4.22 (a) shows the temperature profile of the simulated nanoporous VCSEL operating at the power density for the highest light output power. It shows that the heat generated in the active region is mostly trapped on the p-side due to the poor thermal conductivity of the top dielectric DBR. Assessing the heat flow given by proportional white arrows shown in the inset of Fig. 4.22 (a), we see that heat is concentrated on the p-side and disperses in the lateral direction as predicted in Fig. 4.21 (b). Heating of the p-side explains why at 3% duty cycle, the p-metal contact incurs catastrophic damage before any visible damage to the epilayers can be observed (inset). In addition, the internal temperature rise ΔT for the nanoporous VCSELs is >300°C, whereas reported CW VCSELs operate within ΔT ~160°C, reasoning why CW operation was not possible [71,88,89]. The modeled thermal resistance based on Eqn. (1.29) with respect to the changes in cavity length for various aperture sizes is shown in Fig. 4.22 (b). The cavity length was changed by increasing the thickness of the n-GaN layer below the active region. No significant changes were observed when the cavity length was increased from the p-side. The general trends are very similar to the simulations discussed for Fig. 1.19 (b) where a larger cavity volume helps dissipating the heat more efficiently resulting in a decreased Z_t. Also, overlaid on Fig. 4.22 (b) are the thermal resistance of three the reported CW-RT VCSELs with different architectures and aperture sizes [71,88,89]. Given our 8-λ cavity design with a 20-μm-diameter aperture, the estimated thermal resistance is ~516 K/W which is lower than the reported CW devices. Even though the thermal resistance of our design is based on simulations, the semi-empirical study validates that the nanoporous VCSELs should have thermal resistance at least in the same order of magnitude as [71,88,89]. Thus, CW operation at RT can be expected from the nanoporous VCSELs

without any drastic alterations to the device design, provided the threshold is decreased by a factor of 2 to lower the internal temperatures.

4.4.3. Aperture and yield analysis

The refractive index of GaN in ion implanted apertures decreased by only ~2% between the non-implanted and implanted regions according to Fig. 4.3 (b). Correlating this to calculate the effective mode index of the core (aperture) and cladding region (Al implant) in the cavity using TMM results in an index change $\Delta n/n$ of ~0.1%. Such low $\Delta n/n$ suggest a weak lateral mode confinement in the nanoporous VCSELs, essentially making them gain-guided as opposed to index-guided. Poor optical guiding in the apertures can be the cause of the high threshold current density so it is important to model the confinement. Hence, a simple 2-D core-cladding model was developed using Lumerical™, a FEM-based mode solver, to simulate the lateral (transverse) modes inside a 5 µm and 20 µm diameter aperture. Figure 4.23 shows a schematic of the model with a constant n_{core} of 2.25692 (obtained from TMM simulation) and an infinitely large cladding region, where n_{clad} is

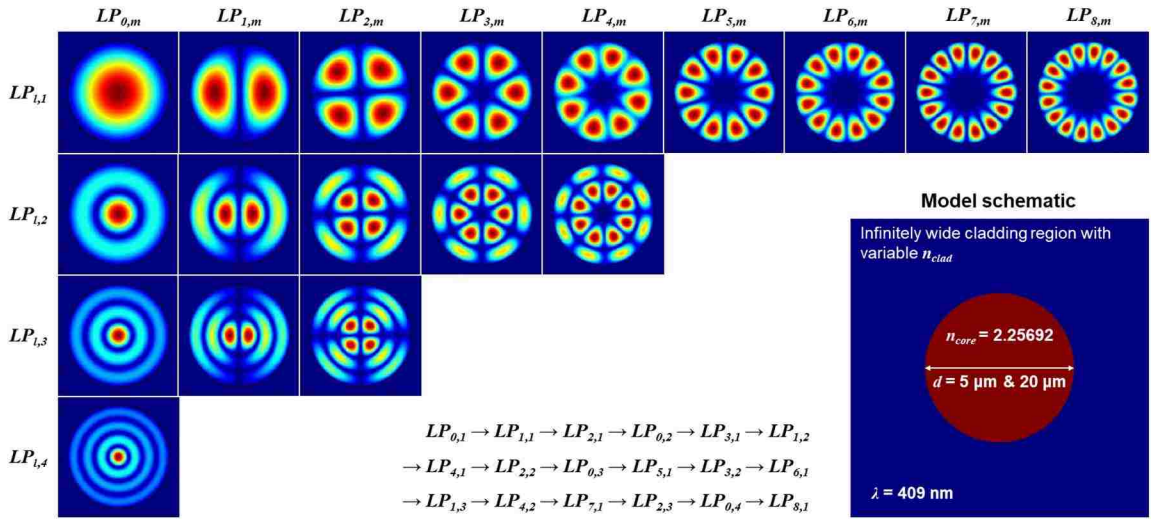

Figure 4.23. Lumerical™ mode solver simulation of the lateral $LP_{l,m}$ modes for a 20 µm aperture with $\Delta n/n$ of 0.25%.

varied to change $\Delta n/n$. For $\Delta n/n$ of 0.25%, the resulting $LP_{l,m}$ mode profiles inside the 20 μm aperture is also shown in Fig 4.23 for 8-azimuthal modes and 4-radial modes. Note that the mode profiles for the 5 μm aperture (not shown in Fig. 4.23) were identical to the 20 μm aperture but the total number of modes were fewer in number. Based on first-order approximation, the total number of confined modes in the core-cladding structure for the 5 μm and 20 μm aperture were ~8 and ~112, respectively [8,204]. The order of the lateral modes is determined by the imaginary part of the effective refractive index obtained from the simulation. The profiles of higher-order modes reside near the edges of the core region resulting in mode leakage and a decreased of the confinement. Consequently, higher-order modes appear later as the imaginary part of the effective refractive index that the mode sees is higher than the lower-order modes. This modal behavior can be visually represented in the array of Fig. 4.23. In general, increasing the effective index contrast between the core and the cladding regions will tightly confine the mode inside the core, allowing higher order modes to be easily supported in the VCSEL [69,83]. But a large abrupt change in Δn can also result in increase scattering and diffraction losses in the cavity, so typically $\Delta n/n$ is maintained below 2% [69,92,205].

The lateral confinement for the 5 μm and 20 μm aperture sizes as a function of $\Delta n/n$ are plotted in Fig. 4.24 (a) and Fig. 4.24 (b), respectively. For simplicity, only eight of the first order radial modes are considered in Fig. 4.24. The confinement is more than 90% for both aperture sizes when $\Delta n/n$ is greater than 1% indicating that the core remains index-guided. Decreasing $\Delta n/n$ further, the confinement exponentially declines for the 5 μm aperture due to mode leakage from the limited area. The drop is more noticeable particularly for higher-order modes that have peaks near the edges of the aperture. As a

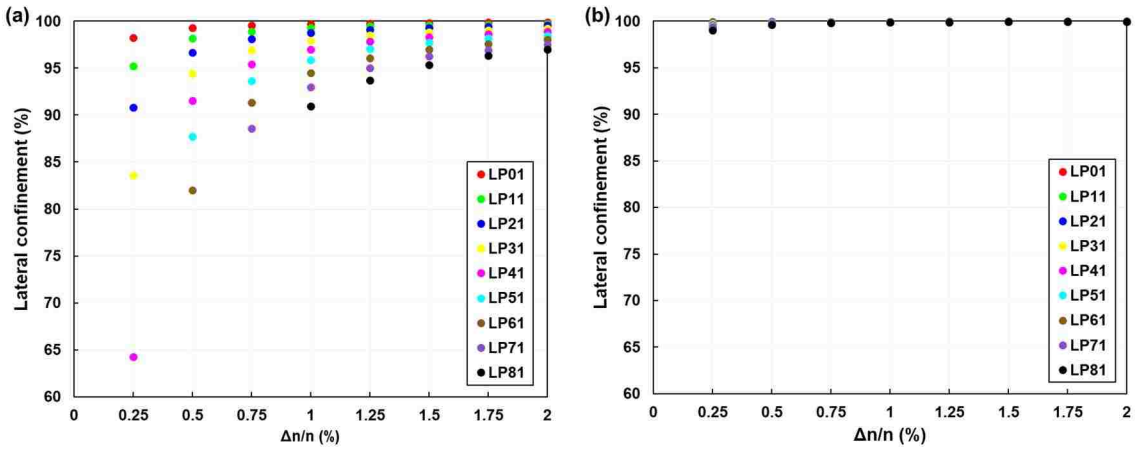

Figure 4.24. Lateral mode confinements as a function of $\Delta n/n$ for 8 $LP_{l,1}$ modes for the (a) 5 µm, and (b) 20 µm aperture design.

result, some high-order mode, like the $LP_{8,1}$, do not even appear in the simulation for $\Delta n/n$ < 1%. Contrary to the 5 µm aperture, the large area in the 20 µm diameter maintains a high confinement down to 0.25%. However, it is expected to drop drastically below 0.25% since the simulation did not converge to any valid solutions at 0.1%, concluding that the nanoporous VCSELs are indeed gain-guided. The ion implanted apertures provide adequate current confinement but very negligible lateral optical confinement. Future designs should adopt the planar dielectric apertures where Δn can be controlled by changing the dielectric/p-GaN etch depth while avoiding anti-guiding [69,71,168].

Unfortunately, none of the conventional mode profiles illustrated in Fig. 4.23 could be observed in the nanoporous VCSELs due to their filamentary emission. The random nature of the filamentation coupled with the distinct divide across the aperture by the nanoporous etch fronts (Fig. 4.18) strongly hinted that the filamentation may originate from the non-uniformity in the cavity resonance as discussed in Chapter 3. This was verified by simulating a similar core-cladding model but with the addition of small nanoscale regions with slightly higher index scattered randomly throughout the core region. The small index

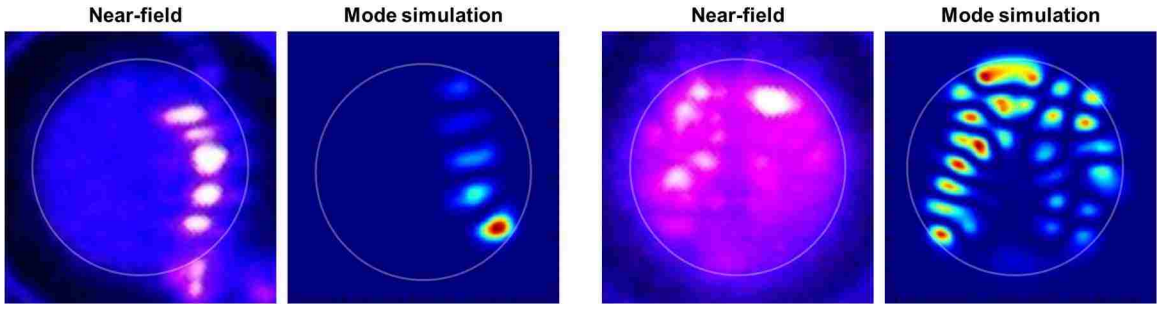

Figure 4.25. Two examples of the near-field emission pattern and mode simulation of 20 μm diameter nanoporous VCSEL aperture.

change was calculated using $\frac{\Delta n}{n} = \frac{\Delta \lambda}{\lambda}$, where $\Delta\lambda$ is the difference in wavelength obtained from the two peaks observed in Fig. 4.18 with λ being the dominant peak. Figure 4.25 depicts two such near-field mode profiles from a 20-μm-diameter aperture VCSEL. In both images, the emission seems to begin from the edges of the aperture. This is likely the result of non-uniform current spreading by the ITO commonly seen in large apertures where the current is concentrated near the edges [11]. Although the simulated profiles conform well to the near-field images, the exact mode numbers are hard to determine because of their irregular shape. The mode is probably a high-order mode that reached a balance between the preferred high-order mode due to non-uniform current spreading and the suppression of high-order modes due to poor lateral confinement.

Almost all previously reported GaN-based VCSELs have exhibited filamentary emissions to some degree even without the use of random porous layers in the structure [62,63,72,75,77,78,80,81,100,206]. A few instances of uniform Gaussian profiles have been reported with the use of backside curved mirrors in long cavity VCSELs with aperture diameters less than 10 μm [79,92,93]. The authors claim that decreasing the diffraction and scattering losses in the cavity is essential for obtaining uniform profiles. However, broadening of the beam waist only becomes an issue when long VCSELs cavities

are considered. Generally, diffraction losses are negligible in short cavity (8-λ) VCSELs but can increase for multiple-pass devices (low α_m). Similar arguments can be made about the scattering loss since designs without any step profiles also exhibit filamentation. Furthermore, it is difficult to assess the root cause of filamentation in small apertures since it eliminates spatial variations in growth non-uniformity and cavity lengths. Filamentation in the nanoporous approach can be reduced by forming even more densely packed smaller pores by increasing n-type doping in the DBR and etching at a lower bias. Further in-depth analysis is required for understanding filamentation in III-nitride VCSELs.

One of the biggest advantages of the nonpolar VCSELs with nanoporous DBRs is the ease of fabrication that resulted in a high yield of devices. Out of the 50 or so devices tested including the smaller aperture sizes (5 μm, 10 μm, and 15 μm), almost 90% of the VCSELs lased at some wavelength depending on the location of the device on the wafer. This variation in emission wavelength was due to the gradual changes in effective cavity resonance relative to the gain bandwidth as the porosity varied across the wafer. The changes in the porosity in the DBR was caused by the spatial variation in current flow during EC etching. The DBRs closer to the indium contact (surface of solution) had smaller pores due to lower currents than the DBRs at the opposite end of the wafer [see Appendix A.4 for a map of the wafer]. Since this was a first demonstration for electrically injected devices with a brand-new architecture, the changes in the effective cavity length was a welcomed discrepancy to allow on-chip tunability of the cavity resonance. We note that this variation on porosity can be avoided on a full wafer fabrication where most of the wafer would be submerged in the etchant. Patterning noble metal contacts near the periphery of the DBRs should also help with the uniformity during the EC etching process.

The high yield also allows us to perform statistical analysis on the devices to gain an understanding of some of the fundamental limitations of the nanoporous VCSEL. Figure 4.26 plots the (a) output power/intensity, (b) slope efficiency, (c) threshold current/current density, and (d) differential resistance as a function of the aperture size. The data points represent the average value of all the devices tested for that particular aperture diameter with error bars. In Fig. 4.26 (a), the total output power increases almost linearly with increasing aperture sizes because of the enlarged emission areas. However, the emission intensity remained reasonably constant for the 10 and 15 μm but dropped for the 20 μm aperture. Given the filamentary nature of emission observed in the VCSELs, the average

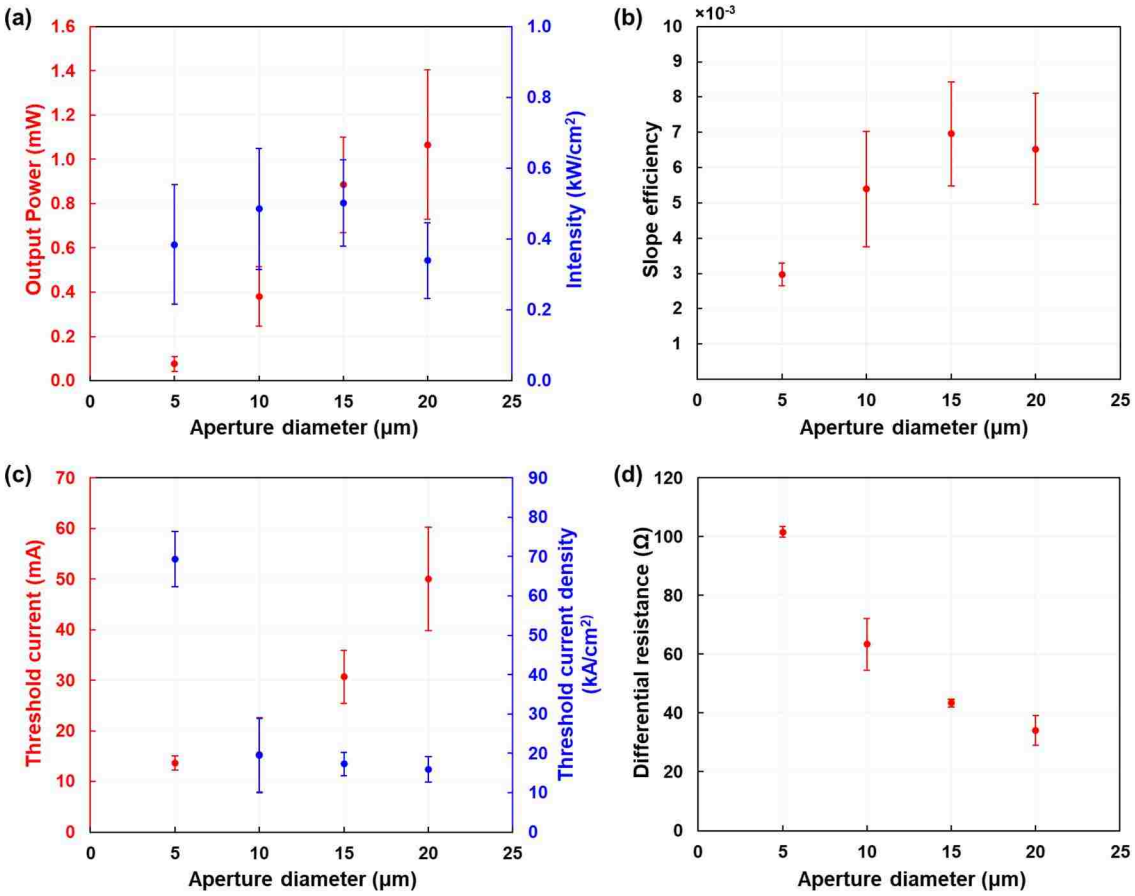

Figure 4.26. Plots showing the (a) output power/intensity, (b) slope efficiency, (c) threshold current/current density, and (d) differential resistance as a function of the aperture size. The data represent the average of 50 device measurements with error bars.

output power is expected to drop due to specular non-uniform emission from large apertures. The lower intensity of the 5 μm aperture is due to the lasing spot being in close proximity to the non-ideal etch front divide in the nanoporous DBRs. We see similar trends for the slope efficiency in Fig. 4.26 (b) which correlates with the output power. The drop in slope efficiency for the 20 μm is a result of nonuniform current spreading in the ITO. More current is required near the center of the aperture to obtain the same power of stimulated emissions occurring at the edge. The current spreading in the p-side, as mentioned in Section 4.4.1, can be significantly improved by replacing the ITO with GaN-based TJs which will also help reduce the layer absorption loss. Now for the threshold current, increasing the aperture size generally means an increased I_{th} as more current is needed to inject across a larger area to reach the same threshold current density. However, in Fig. 4.26 (c), the current density drastically changes from ~60 kA/cm^2 for the 5 μm to ~15 kA/cm^2 for the 10 μm aperture. This is primarily the cause of poor lateral confinement in the 5 μm apertures in addition to the lasing spot being at a non-ideal location near where the EC etch fronts meet. As previous explained for Fig. 4.24 (a), a limited confinement imply that the active region must be pumped harder to reach the threshold modal gain (Γg_{th}). Since Γ is small, the threshold material gain g_{th} must be large which is correlates to high current densities as per [13]. Beyond 10 μm apertures where the confinement is more or less steady, the threshold current density remains fairly constant. Figure 4.26 (d) plots the differential resistance against the aperture size, where it drops gradually from ~100 Ω to ~34 Ω. All the VCSELs had the same device dimensions apart from the aperture diameters, meaning that the current flow was restricted in the axial direction for the smaller apertures resulting in the high differential resistance. The larger aperture sizes allow the

flow of current at lower voltages. Overall, the trends in Fig. 4.26 highlighted the importance of choosing the proper aperture diameters. Small apertures suffer from weak confinement, while large apertures suffer from filamentation and non-uniform current spreading. It appears that for the current design, 10 μm and 15 μm apertures are the most optimized. Addressing some of the aforementioned issue in future designs may optimize the other aperture sizes as well.

4.5. Summary

In summary, this chapter demonstrated the first ever electrically injected GaN-based VCSEL with a nanoporous bottom DBR. The VCSELs achieved a maximum output power of ~1.5 mW from the topside, which is a record for nonpolar *m*-plane VCSELs. All devices tested were uniformly polarization locked in the *a*-direction with a near unity polarization ratio, implying negligible optical scattering from the nanoporous DBR. Temperature-dependent analysis produced stable threshold current behavior with increasing temperature. In the future, integration of a tunnel junction current spreading layer instead of ITO should reduce the threshold current density and operating voltage to allow CW operation. Increasing the cavity length will benefit from the increased overlap of multiple cavity modes with the gain spectrum along with reduced thermal resistance. Furthermore, the performance of the VCSELs is expected to improve significantly by enhancing the lateral mode confinement by replacing the ion implanted apertures with a planar dielectric-step aperture. For a first demonstration, the results were very promising suggesting that the nanoporous epitaxial DBRs indeed offers a viable approach for electrically injected GaN-based VCSELs to mitigate some issues affecting III-nitride VCSELs.

5. Conclusion

The nanoporous design offers a unique solution for solving some of the DBR related issues faced in III-nitride VCSELs. As described in the thesis, the simplicity in growth and fabrication of the devices make them attractive to research for understanding the fundamental properties of III-nitride VCSELs. The high yield of VCSELs may also be of interest to the industry for commercialization by further developing and optimizing the design. It is often assumed that porous structures would introduce significant scattering losses in the cavity, coupled with poor thermal properties. Though it is true to some extent, we have shown that with proper control of the design aspects, it is possible to obtain stimulated emission from electrically injected GaN-based VCSELs using nanoporous DBRs. Our record high output power in *m*-plane along with the high yield of polarization-pinned devices is a testament to what can be achieved.

Electrically injected nanoporous VCSELs opens the doors to several optimization and research related avenues for future exploration. Firstly, several epilayers such as the p-GaN, EBL, and QWs/barriers, need to be optimized to enhance the overall devices performance. Presently, the devices exhibit Schottky p-GaN contacts which increases the operating voltage and decreases the wall-plug efficiency of the VCSELs. Ohmic contacts can be obtained with the appropriate p-type doping concentration coupled with proper activation of the Mg-dopants. In Chapter 4, it was shown that the threshold current density could be further reduced by increasing the number of QWs in the active region, and low injection efficiency was likely due to growth inconsistencies in the EBL. A thorough

systematic analysis on both the EBL and the active region is yet to be performed, which is quintessential to the realization of high output power devices.

The uniformity of the *m*-plane nanoporous DBRs is another area for improvement. We observed that the porosity varies spatially across the sample due to changes in the current density during the EC etching. This inhomogeneity can be reduced by fabricating the VCSELs on full wafers where a large portion of the sample would be submerged into the etchant. Our current process avoids the deposition of metals on the sample prior to the porosification step to prevent corrosion in acids. However, the use of noble metals (like Au or Pt) around the DBR trenches, should withstand the weak oxalic acid etchant and improve the uniformity of the nanoporous layers by efficiently spreading the current across the entire wafer. Furthermore, increasing the n-doping concentration of the DBR layers and lowering the EC etch bias to obtain densely packed smaller pores will definitely aid in minimizing the filamentary emission from the aperture. The exact cause of filamentation is still debated in the community and requires further investigation to remove it completely.

The ultimate goal would be to demonstrate a RT-CW operated nanoporous VCSEL, but it could not be achieved due to the high threshold current densities. Steps towards lowering the threshold by replacing the highly absorption layers should be explored. ITO was used as intracavity current spreading layer and has the highest absorption coefficient out of all the layers in the cavity. Recent developments in GaN-based TJs grown in either MBE or MOCVD [81,89,90], have shown promising results in terms of enhanced lateral current spreading and lowering the total internal loss. The TJ based intracavity contact can seamlessly be applied to our existing device architecture. It also opens the door to a fully epitaxial VCSEL by enabling the growth of top-side nanoporous DBRs to replace the

thermally insulating and lossy top dielectric DBRs. Additionally, the threshold current density can be lowered by making the VCSEL apertures index guided. The Al-ion implanted apertures had very little index contrast between the transverse core and the cladding region which resulted in a gain guided design. The transverse modes were not tightly confined within the core region and the mode leakage caused high threshold current densities in small aperture VCSELs. A patterned dielectric aperture with a planar design will eliminate anti-guiding effects while significantly improving the lateral confinement at the same time.

Lastly, the future direction for the nonpolar nanoporous VCSELs can include the fabrication of polarization-pinned 2-D arrays to study the far-field emission patterns. The 3dB-bandwidth is also expected to be very high for non-polar GaN VCSELs for their small active volume. High-speed measurements are seldom reported by research groups due to measurement limitations or poor device performance. Our group has previously reported high-speed characterization of *m*-plane LEDs using a virtual network analyzer [207,208]. In the time of writing this thesis, we are currently in the process of measuring the modulation speed of the nanoporous VCSELs.

Before concluding this chapter, I would like to acknowledge the fact that VCSELs were among the most difficult and challenging optoelectronic devices that I had to fabricate throughout the course of my PhD. For many years, several academic research groups have attempted electrically injected GaN VCSELs, which only one other group in the United States (UCSB) was able to accomplish. It is no wonder that all major players in the VCSEL community are industry-based R&D groups. Regardless, I am certain that with the collective effort of the industry and academic research groups, it is only a matter of time

before III-nitride VCSELs becomes rapidly commercialized. Moreover, I am thrilled that we were able to leave a noticeable footprint in our very first attempt at an electrically injected VCSEL and contribute a new device design to the III-nitride VCSEL community.

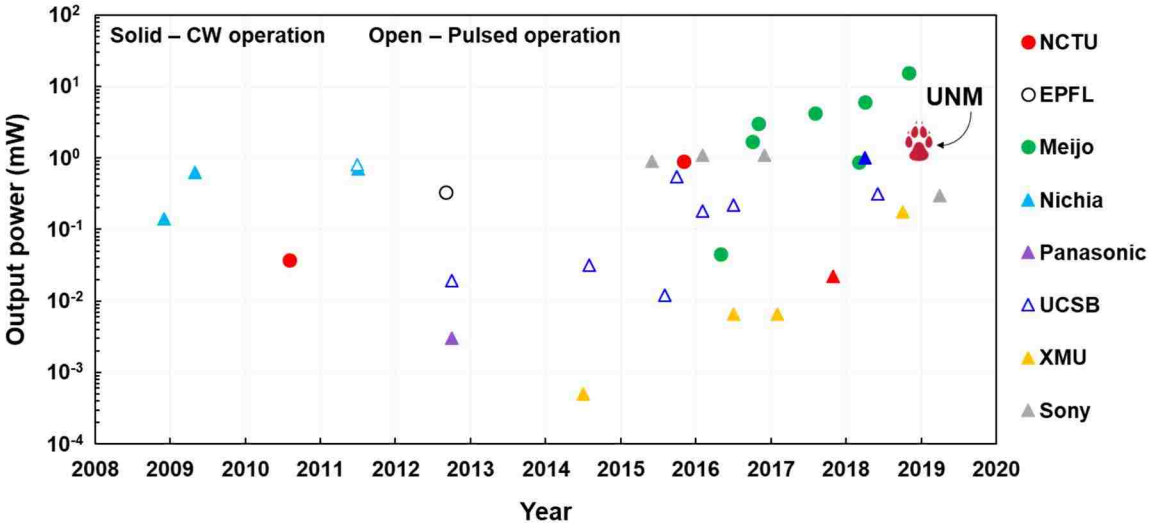

Appendix

A.1 MOCVD Growth recipe

Growth recipe of sample 180830_mVCSEL-6

The numbers below were recorded during the time of growth. Conditions are subject to change depending on the health of the reactor.

Layer	Temp	NanoPor	UID	GaN	n+ GaN	n- GaN	Barrier	InGaN QW	Barrier	EBL	p- GaN	p+ GaN
Repeat	-	← ×16 →		-	-	-	-	← ×6 →		-	-	-
Time	15	8.41	3.68	50.75	20.47	20	1.28	2.56	1.28	3.25	5	4.5
TC/Power	644.8/64.3	636.2/62.9	636/62.9	640.9/64.1	641/64.3	641/64.5	494.1/48	492.2/48	491.7/48	583.5/55.1	584.8/55.2	585.9/55.2
Real temp	964.3	965.3	965.3	967.2	969.1	969	746.5	745.5	745.2	833.5	834.6	835
Voltage/Current	22.2/80.8	21.7/79.5	21.7/79.4	22.1/81	22.2/80.9	22.2/80.9	15.2/60.5	15.1/60.3	15.2/60.4	17.8/69.7	17.9/69.5	17.9/69.8
Pressure/Position	499.1/6.8	499.5/6.9	499.3/6.8	499.5/6.5	499.4/6.7	499.7/6.9	204.7/9	204.7/9.1	204.7/9	204.2/7.7	204.1/7.5	204.3/7.6
RPM	1500	1500	1500	1500	1500	1500	1100	1100	1100	750	750	750
Flange temp.	24.5	24.3	24.2	24.4	24.4/64.3	24.4/64.5	22.6	22.5	22.5	23.3	23.3	23.4
Alk/Push inner	234.2/228.2	234.4/228	235/228	235/228	235/228	235/227	132/119	133.2/119	132/119	83.2/63	83/63.2	83.6/62.8
Alk/Push outer	590/905	590/905	590.2/905	590/905	590/905	590/905	106/713	107/713.2	106/713.1	76.8/387	77/387	77/387
Hyd pressure	760	760	760	761	761	761	457	457	457	429	428	429
N_2 flow	3712	3710	3708	3712	3710	3710	410	410	410	-	-	-
H_2 flow	-	-	-	-	-	-	-	-	-	3500	3500	3504
NH_3 flow	2099	2100	2099	2100	2101	2100	3671	3672	3672	1998	2000	2001
SiH_4 pure/mix/dd	-	31/500/35	-	-	15/500/15	6/1000/6	-	-	-	-	-	-
TMG raw/push/dd/pres	34/42/ 34/900	14/46/ 16/900	14/46/ 16/600	14/46/ 16/900	14/46/ 16/900	14/46/ 16/900	-	-	-	6/100/ 6/900	25/40/ 25/900	10/45/ 10/900
TEG raw/pres	-	-	-	-	-	-	60/900	60/900	60/900	-	-	-
TMI raw/pres	-	-	-	-	-	-	-	120/800	-	-	-	-
TMA raw/push/dd/pres	-	-	-	-	-	-	-	-	-	10/65/ 10/900	-	-
Cp_2Mg raw/pres	-	-	-	-	-	-	-	-	-	120/900	60/900	120/900

A.2 Hi-resolution XRD rocking curves

6-period $In_xGa_{1-x}N$ (180809mInGaNxrd)

ID	Material	Thickness (nm)	Concentration
2	GaN (hex)	2.29	---
1	InN (hex)+GaN (hex)	3.05	0.145
Substrate	GaN (hex)	0.00	---

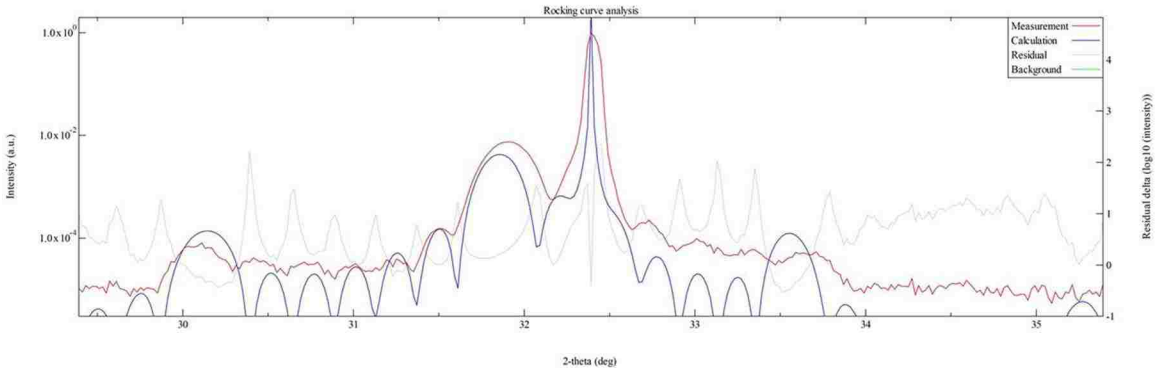

Single layer $Al_xGaN_{1-x}N$ (180810mAlGaNxrd)

ID	Material	Thickness (nm)	Concentration
1	AlN (hex)+GaN (hex)	15.407	0.410398
Substrate	GaN (hex)	0.00	---

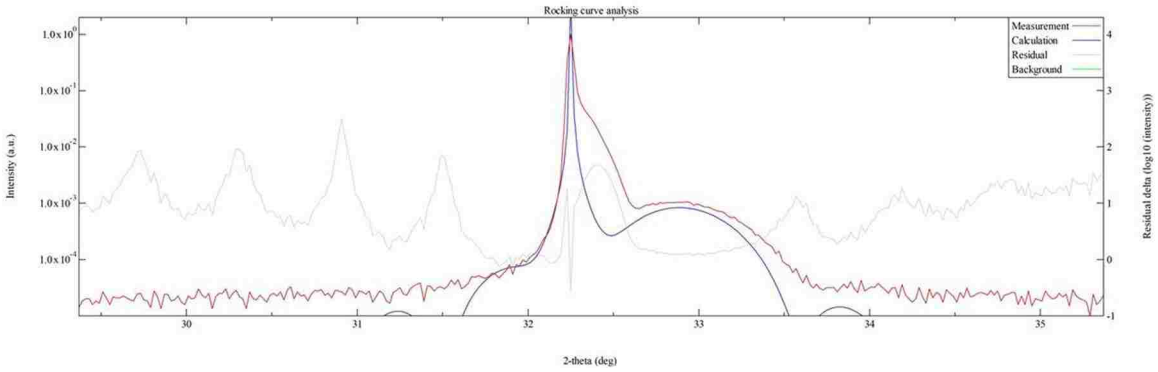

A.3 Fabrication process traveler

UNM Nonpolar III-Nitride Nanoporous DBR VCSEL		
Author: Saadat Mishkat-Ul-Masabih Updated: 04/11/2019		
General prep	PR cabinet	Refill PR and check expiration date
		SPR220-3.0
		SPR220-7.0
		nLOF2020
		nLOF2035
Growth calibration	MOCVD	Grow the following calibration samples:
		nGaN/GaN varied thickness DBR test
		pAlGaN XRD
		InGaN/GaN 6QWs XRD
		nGaN-QW-pGaN LED-PEC
Calibration analysis	XRD	Analyze XRD samples for thickness and composition
	EC etch setup	EC etch DBR test sample to quantify porosity and thickness
	EL setup	In-dot quicktest on LED sample for spectrum and L-I-V
	PEC etch setup	PEC etch LED sample to verify QW and p-side thickness
VCSEL epi growth	MOCVD	Grow VCSEL epi with corrected growth times and temperature
	Oven	Activate after growth at 650C for 15min
	EL setup	In-dot quicktest on LED sample for spectrum and L-I-V
Remove In	Acid bench	3:1 HCl:HNO_3 aqua regia x3 for 15min. New batch every iteration. Wait till solution is boiling in hotplate and is deep orange in color. End with DI rinse for 5min and N_2 dry.
Mesa1 litho	Solvent bench	Sonicate: 3min Ace, 3min Iso, 5x30sec DI+Liquinox rinse, N_2 dry
	Hotplates	Dehydration bake, 2min in 112C, cool for 1min
	Spinners	Spin HMDS 3000rpm 30sec
		Spin SPR220-3.0 3000rpm 30sec
		Edge-bead removal using razor blade
	Hotplates	Soft bake in 112C for 90sec, cool for 30sec
	Contact aligner	Expose “Mesa1”, CI2 for 12sec, black chuck, hard contact
	Develop bench	Develop in AZ300MIF 60sec, DI rinse, N_2 dry
	Microscope	Inspect and develop more if necessary
Mesa1 etch	Cl etcher	Load dummy carrier
		Run GaN_SMM for 5min chamber conditioning
	Spinners	Spin AZ4330 3000rpm 30sec in carrier
		Drop sample in the middle, press corners to bond
	Hotplates	Bake in 90C for 90sec, cool for 30sec
	Cl etcher	Run GaN_SMM (~2.4nm/sec) to etch till nGaN contact layer
	Develop bench	Preheat NMP for 20min at 80C in sonicator
		Sonicate 3min, 3x30sec DI rinse, N_2 dry
	Microscope	Check for PR residue
	Profilometer	Check for desired etch depth
Aperture litho	Solvent bench	Sonicate: 3min Ace, 3min Iso, 5x30sec DI+Liquinox rinse, N_2 dry
	Hotplates	Dehydration bake, 2min in 112C, cool for 1min
	Spinners	Spin HMDS 3000rpm 30sec
		Spin nLOF2020 3000rpm 30sec
		Edge-bead removal using razor blade
	Hotplates	Soft bake in 112C for 90sec, cool for 30sec
	Contact aligner	Expose “Aperture”, CI1 for 9sec, black chuck, hard contact
	Hotplates	Post-exposure bake in 112C for 60sec, cool for 30sec

	Develop bench	Develop in AZ300MIF 60sec, DI rinse, N_2 dry
	Microscope	Inspect and develop more if necessary
Protective metal dep	Acid bench	1:1 HCl:DI dip 30s, 3x30sec DI rinse, N_2 dry
	Ebeam evap	Deposit Ti/Au 200A/3000A (1A/s for thin to 2A/s for thick layers)
	Develop bench	Preheat NMP for 20min at 80C in sonicator
		Pipette till complete liftoff, 3x30sec DI rinse, N_2 dry
	Microscope	Check for liftoff
Al ion implant	Leonard Kroko Inc.	Wafer size: 5mm by 8mm
		Ion: Al, Dose: 10^{15}ions/cm^2, Energy: 20keV, normal incidence
		~3 day turn-around
	Acid bench	3:1 HCl:HNO_3 aqua regia x3 for 15min. New batch every iteration.
		Wait till solution is boiling in hotplate and is deep orange in color.
		End with DI rinse for 5min and N_2 dry.
Mesa2 litho	Solvent bench	Sonicate: 3min Ace, 3min Iso, 5x30sec DI+Liquinox rinse, N_2 dry
	Hotplates	Dehydration bake, 2min in 112C, cool for 1min
	Spinners	Spin HMDS 3000rpm 30sec
		Spin SPR220-3.0 3000rpm 30sec
		Edge-bead removal using razor blade
	Hotplates	Soft bake in 112C for 90sec, cool for 30sec
	Contact aligner	Expose “Mesa2”, CI2 for 12sec, black chuck, hard contact
	Develop bench	Develop in AZ300MIF 60sec, DI rinse, N_2 dry
	Microscope	Inspect and develop more if necessary
Mesa2 etch	Cl etcher	Load dummy carrier
		Run GaN_SMM for 5min chamber conditioning
	Spinners	Spin AZ4330 3000rpm 30sec in carrier
		Drop sample in the middle, press corners to bond
	Hotplates	Bake in 90C for 90sec, cool for 30sec
	Cl etcher	Run GaN_SMM (~2.4nm/sec) to etch till UID layer before DBR
	Develop bench	Preheat NMP for 20min at 80C in sonicator
		Sonicate 3min, 3x30sec DI rinse, N_2 dry
	Microscope	Check for PR residue
	Profilometer	Check for desired etch depth
Topside passivation	Ebeam evap	Blanket dep 300nm of SiO_2 (1A/s), mount with double-sided tape
Trench litho	Solvent bench	Sonicate: 3min Ace, 3min Iso, 5x30sec DI+Liquinox rinse, N_2 dry
	Hotplates	Dehydration bake, 2min in 112C, cool for 1min
	Spinners	Spin HMDS 3000rpm 30sec
		Spin SPR220-3.0 3000rpm 30sec
		Edge-bead removal using razor blade
	Hotplates	Soft bake in 112C for 90sec, cool for 30sec
	Contact aligner	Expose “Trench”, CI2 for 12sec, black chuck, hard contact
	Develop bench	Develop in AZ300MIF 60sec, DI rinse, N_2 dry
	Microscope	Inspect and develop more if necessary
Trench etch	F etcher	Load dummy carrier
		Run GaN_SMMF for 5min chamber conditioning
	Cl etcher	Load dummy carrier
		Run GaN_SMM for 5min chamber conditioning
	Spinners	Spin AZ4330 3000rpm 30sec in carrier
		Drop sample in the middle, press corners to bond
	Hotplates	Bake in 90C for 90sec, cool for 30sec
	F etcher	Run GaN_SMMF (~2nm/sec) to etch till SiO_2 completely etched
	Cl etcher	Run GaN_SMM (~2.4nm/sec). Etch till DBR sidewalls is exposed
	Develop bench	Preheat NMP for 20min at 80C in sonicator

		Sonicate 3min, 3x30sec DI rinse, N_2 dry
	Microscope	Check for PR residue
	Profilometer	Check for desired etch depth
EC etch	Soldering iron	Scratch and solder indium-pad in sample corner
	Acid bench	Prepare EC etch set up, 0.3M oxalic acid, minimal stirring, no heat
		Clip sample to anode (red wire), Pt wire to cathode (black wire)
		Do not submerge indium-pad or contact clips
		Etch for 1hr in 5V, DI rinse, N_2 dry
	Microscope	Remove sample and inspect to obtain lateral etch rate
	Acid bench	Re-clip sample, continue EC etching until complete porosification.
		Check every hour for level drop. Refill with pipette if required.
		DI rinse, N_2 dry
	Microscope	Check for complete lateral porosification
		Scrap off In-pad using razor blade
	Acid bench	Strip SiO_2 passivation in buffer HF 10min, 3min DI rinse, N_2 dry
	SEM	Image nanopores cross-section to measure porosity and reflectance
Sidewall passivation litho	Solvent bench	Swirl: 3min Ace, 3min Iso, 5x30sec DI+Liquinox rinse, N_2 dry
	Hotplates	Dehydration bake, 2min in 112C, cool for 1min
	Spinners	Spin HMDS 3000rpm 30sec
		Spin nLOF2020 3000rpm 30sec
		Edge-bead removal using razor blade
	Hotplates	Soft bake in 112C for 90sec, cool for 30sec
	Contact aligner	Expose “Dielectric”, CI1 for 9sec, black chuck, hard contact
	Hotplates	Post-exposure bake in 112C for 60sec, cool for 30sec
	Develop bench	Develop in AZ300MIF 60sec, DI rinse, N_2 dry
	Microscope	Inspect and develop more if necessary
SiN_x sidewall deposition	PECVD	Run SiN_ICP2_LS_100 for 5min chamber conditioning
		Drop sample in chuck where deposition is “centered”
		Run SiN_ICP2_LS_100 (~1.8nm/s) and deposit 150nm
	Develop bench	Preheat NMP for 20min at 80C in sonicator
		Pipette till complete liftoff, 3x30sec DI rinse, N_2 dry
	Microscope	Check for liftoff
	Profilometer	Check for desired layer thickness
Current spreading litho	Solvent bench	Swirl: 3min Ace, 3min Iso, 5x30sec DI+Liquinox rinse, N_2 dry
	Hotplates	Dehydration bake, 2min in 112C, cool for 1min
	Spinners	Spin HMDS 3000rpm 30sec
		Spin nLOF2020 3000rpm 30sec
		Edge-bead removal using razor blade
	Hotplates	Soft bake in 112C for 90sec, cool for 30sec
	Contact aligner	Expose “Current spreading”, CI1 for 9sec, black chuck, hard cont.
	Hotplates	Post-exposure bake in 112C for 60sec, cool for 30sec
	Develop bench	Develop in AZ300MIF 60sec, DI rinse, N_2 dry
	Microscope	Inspect and develop more if necessary
ITO deposition	Acid bench	1:1 HCl:DI dip 30s, 3x30sec DI rinse, N_2 dry
	Ebeam evap	Co-load sample and dummy wafers (DSP sapphire and/or Si)
		Deposit ITO 500A (0.5A/s), 10sccm O_2, rotation, no heating
	Develop bench	Preheat NMP for 20min at 80C in sonicator
		Pipette till complete liftoff, 3x30sec DI rinse, N_2 dry
	Microscope	Check for liftoff
	RTA	Anneal samples at 550C for 15mins in 6sccm N_2
	Ellipsometer	Measure thickness, n & k using saved model in “Saadat_ITO”
	AFM	Measure dummy sample RMS roughness in hi-res (20μm x 20μm)
	UV-Vis spm	Verify absorption coefficient using R+T measurement

	CTLM	Perform fits to measure sheet resistance and resistivity
p-contact litho	Solvent bench	Swirl: 3min Ace, 3min Iso, 5x30sec DI+Liquinox rinse, N_2 dry
	Hotplates	Dehydration bake, 2min in 112C, cool for 1min
	Spinners	Spin HMDS 3000rpm 30sec
		Spin nLOF2020 3000rpm 30sec
		Edge-bead removal using razor blade
	Hotplates	Soft bake in 112C for 90sec, cool for 30sec
	Contact aligner	Expose "p-Contact", CI1 for 9sec, black chuck, hard contact
	Hotplates	Post-exposure bake in 112C for 60sec, cool for 30sec
	Develop bench	Develop in AZ300MIF 60sec, DI rinse, N_2 dry
	Microscope	Inspect and develop more if necessary
p-contact deposition	Ebeam evap	Deposit Ti/Au 200A/3000A, mount with double-sided tape (1A/s for thin to 2A/s for thick layers)
	Develop bench	Preheat NMP for 20min at 80C in sonicator
		Pipette till complete liftoff, 3x30sec DI rinse, N_2 dry
	Microscope	Check for liftoff, liftoff more if necessary
n-contact litho	Solvent bench	Swirl: 3min Ace, 3min Iso, 5x30sec DI+Liquinox rinse, N_2 dry
	Hotplates	Dehydration bake, 2min in 112C, cool for 1min
	Spinners	Spin HMDS 3000rpm 30sec
		Spin nLOF2035 3000rpm 30sec
		Edge-bead removal using razor blade
	Hotplates	Soft bake in 112C for 90sec, cool for 30sec
	Contact aligner	Expose "n-Contact", CI1 for 10sec, black chuck, hard contact
	Hotplates	Post-exposure bake in 112C for 60sec, cool for 30sec
	Develop bench	Develop in AZ300MIF 60sec, DI rinse, N_2 dry
	Microscope	Inspect and develop more if necessary
p-contact deposition	Ebeam evap	Deposit Ti/Al/Ni/Au 200A/1000A /500A /3000A, mount with double-sided tape (1A/s for thin to 2-3A/s for thick layers)
	Develop bench	Preheat NMP for 20min at 80C in sonicator
		Pipette till complete liftoff, 3x30sec DI rinse, N_2 dry
	Microscope	Check for liftoff, liftoff more if necessary
Top DBR calibration	PECVD	Run SiO2_ICP2_LS_100 for 5min chamber conditioning
		Drop Si calibration sample in chuck where deposition is "centered"
		Run SiO2_SiN_ICP2_100 five times for 25 pairs of SiO_2/SiN_x
	UV-Vis spm	Check reflectance and stopband using dielectric reference mirror
	Acid bench	Cleave calibration sample, dip cleaved edge in buffer HF for 10sec
		3x30sec DI rinse, N_2 dry
	SEM	Image cleaved edge cross-section for thickness and deposition rate
	Vertical	Fit TMM with measured values to check layer thickness and index
Top DBR depostion	PECVD	Run SiN_ICP2_LS_100 for 5min chamber conditioning
		Drop sample + dummy Si in chuck where deposition is "centered"
		Run SiN_ICP2_LS_100 for SiN_x spacer layer based on SiN_x deposition rate
		Run SiO2_SiN_ICP2_100 five times for 25 pair of SiO_2/SiN_x blanket dep.
	UV-Vis spm	Check sample reflectance and stopband from Si dummy
Top DBR litho	Solvent bench	Swirl: 3min Ace, 3min Iso, 5x30sec DI+Liquinox rinse, N_2 dry
	Hotplates	Dehydration bake, 2min in 112C, cool for 1min
	Spinners	Mount sample on blue tape, place sapphire corals along long edges
		Spin HMDS 3000rpm 30sec, then spin SPR220-7.0 4000rpm 30sec
		Repeat steps if film not uniform
		Edge-bead removal using razor blade only on smaller edges
	Hotplates	Indirect soft bake on top of Q-tips in 112C for 60sec

		Direct soft bake on hotplate in 112C for 90sec, cool for 1min
	Contact aligner	Expose "Top DBR", CI2 for 25sec, black chuck, hard contact
		Hold sample for 3 hours for crucial rehydration
	Hotplates	Post-exposure bake 112C for 60sec
	Develop bench	Develop in AZ300MIF 3min, DI rinse, N_2 dry
	Microscope	Inspect and develop more if necessary
Top DBR etch	F etcher	Load dummy carrier
		Run GaN_SMMF for 5min chamber conditioning
	Spinners	Spin AZ4330 3000rpm 30sec in carrier
		Drop sample in the middle, press corners to bond
	Hotplates	Bake in 90C for 90sec, cool for 30sec
	F etcher	Run GaN_SMMF (~3nm/sec) to over-etch blanket top DBR
	Develop bench	Preheat NMP for 20min at 80C in sonicator
		Pipette till completely stripped, 3x30sec DI rinse, N_2 dry
	Microscope	Check for PR residue
	Profilometer	Check for desired etch depth
Backside polishing (optional)	Solvent bench	Swirl: 3min Ace, 3min Iso, 5x30sec DI+Liquinox rinse, N_2 dry
	Hotplates	Dehydration bake, 2min in 112C, cool for 1min
	Spinners	Spin SPR220-3.0 3000rpm 30sec
		Re-pipette and spin SPR220-3.0 again 3000rpm 30sec
		Edge-bead removal using razor blade
	Hotplates	Soft bake in 112C for 2min, cool for 1min
	Drop gauge	Measure sample height on all 4 corners from the backside
	Hotplates	Heat CMP chuck and melt 2-3 pellets of wax
		Drop sample PR face down on melted wax
	Solvent bench	Remove chuck from hotplate, place wipe and weight on top
		Cool for 5 mins
	CMP	Spin water film over entire wheel
		Place 3µm diamond grit paper on wheel, scrap w/pad to secure
		Mount chuck into arm
		Polish 5mins at 100rpm, force-1, full oscillation and rotation
		Monitor removed material while polishing
	Drop gauge	Demount chuck, measure sample height on 4 corners from the backside
	CMP	Remove 3µm diamond grit paper from wheel, reapply water film
		Place 1µm diamond grit paper on wheel, scrap w/pad to secure
		Mount chuck into arm
		Polish 5mins at 100rpm, force-1, full oscillation and rotation
		Monitor removed material while polishing
	Drop gauge	Demount chuck, measure height on 4 corners from the backside
	CMP	Remove 1µm diamond grit paper from wheel, reapply water film
		Place 200nm diamond grit paper on wheel, scrap w/ pad to secure
		Mount chuck into arm
		Polish 5mins at 100rpm, force-1, full oscillation and rotation
		Monitor removed material while polishing
	Drop gauge	Demount chuck, measure height on 4 corners from the backside
	Microscope	Continue polishing until backside of device is visible
	Hotplates	Heat chuck to melt wax and release sample
		Soak sample in Opticlear™ for 15mins
	Solvent bench	Swirl: 3min Iso, 5x30sec DI rinse, N_2 dry
LIV test	EL setup	Nanoporous VCSEL fabrication complete!

A.4 Sample map

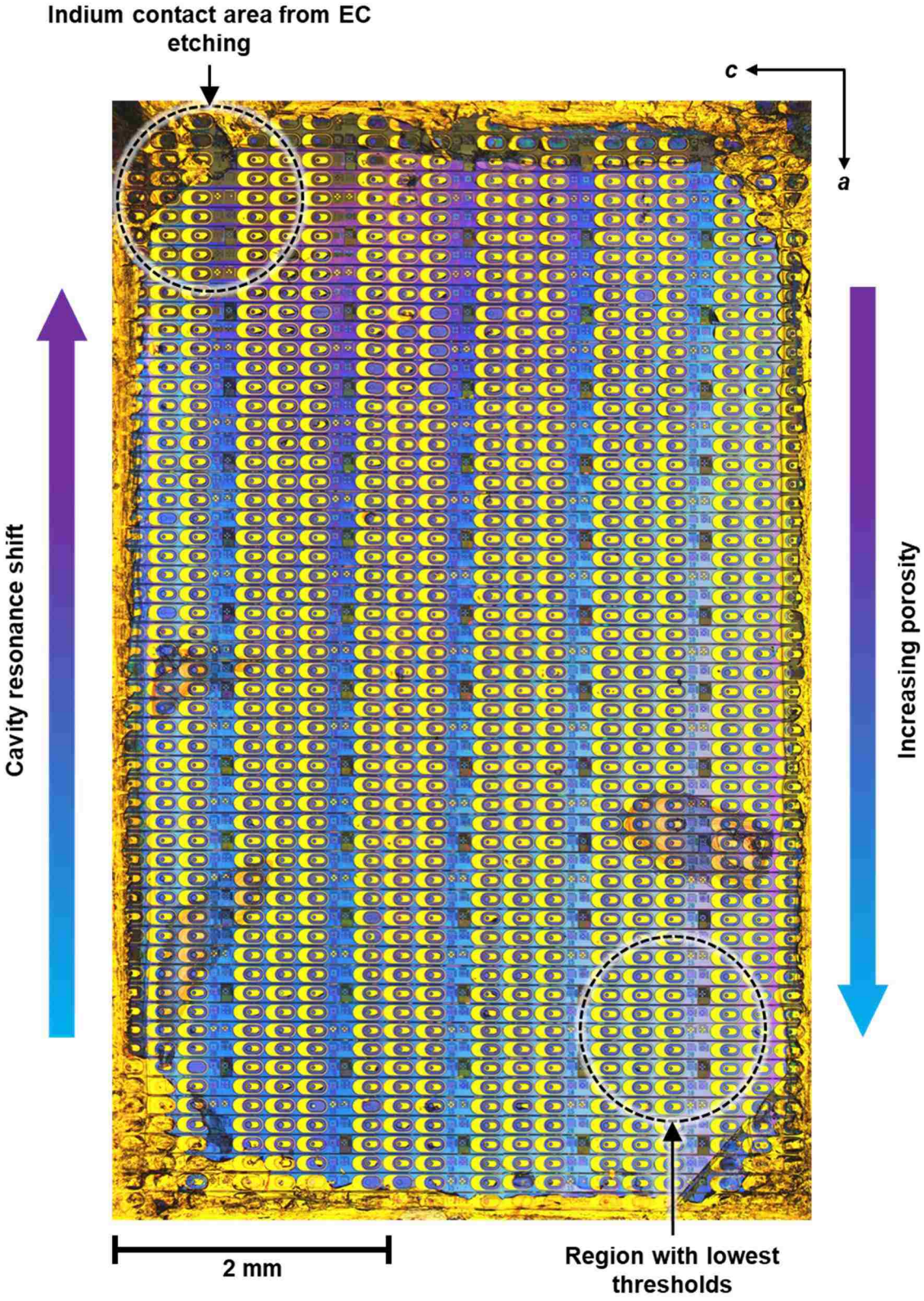

A.5 VAT MATLAB script

You may have to change the hue of SEM images sometimes for the code to work.

```
clear all;
close all;
clc;

R_file = imread('image_name.jpg');  %paste name of SEM image
subplot(4,1,1);                %SEM image must be in same directory as
code
imagesc(R_file);

R_file = rgb2gray(R_file);
subplot(4,1,2);
imagesc(R_file);

R_file = imadjust(R_file);
subplot(4,1,3);
imagesc(R_file);

R_file = im2bw(R_file);
subplot(4,1,4);
imagesc(R_file);

[Nx Ny] = size(R_file);

c=0;

for ii = 1:Nx;
    for jj= 1:Ny;
        if R_file(ii,jj)==0
            c= c+1;
        end
    end
end

porosity = (c/(Nx*Ny))

n_gan = 2.3762;    %change for corresponding wavelength
n_air = 1;
N = 25;            %number of DBR pairs

n_por = (((1-porosity)*(n_gan^2))+(porosity*(n_air^2)))^0.5

R = 100*(((n_air*(n_gan^(2*N))) -
(n_gan*(n_por^(2*N))))/((n_air*(n_gan^(2*N))) +
(n_gan*(n_por^(2*N)))))^2
```

A.6 Setup photos

Pulsed L-I-V/EL setup with heated stage.

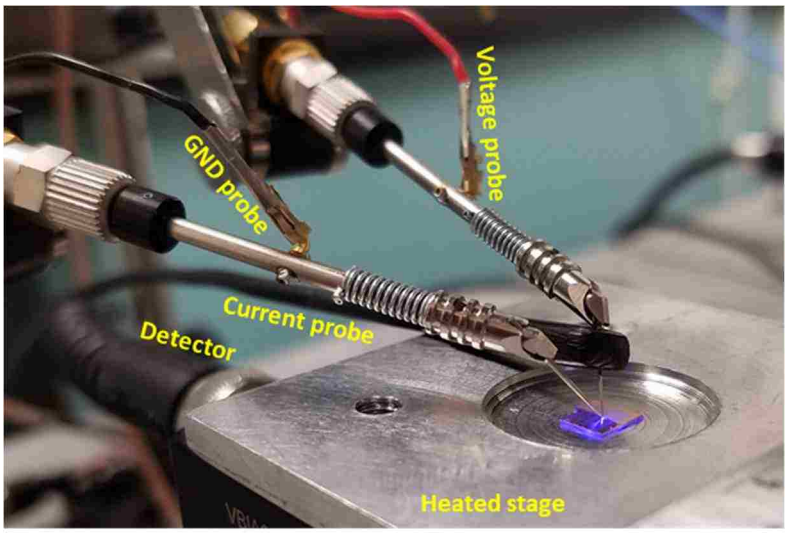

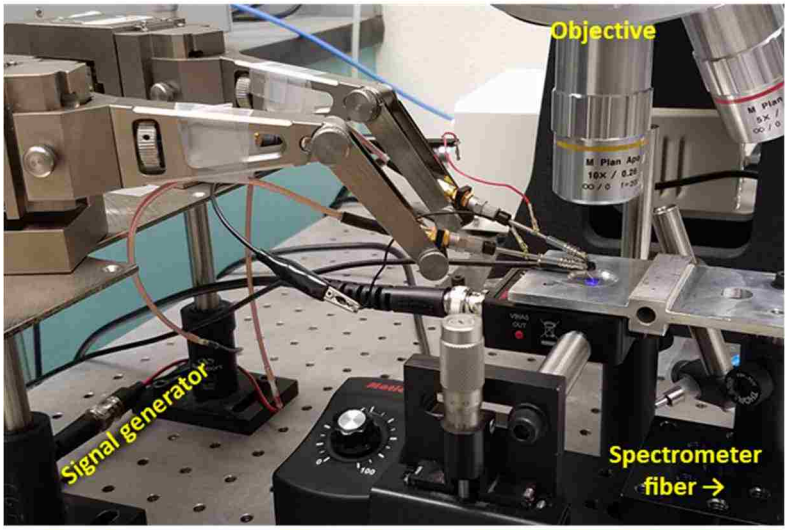

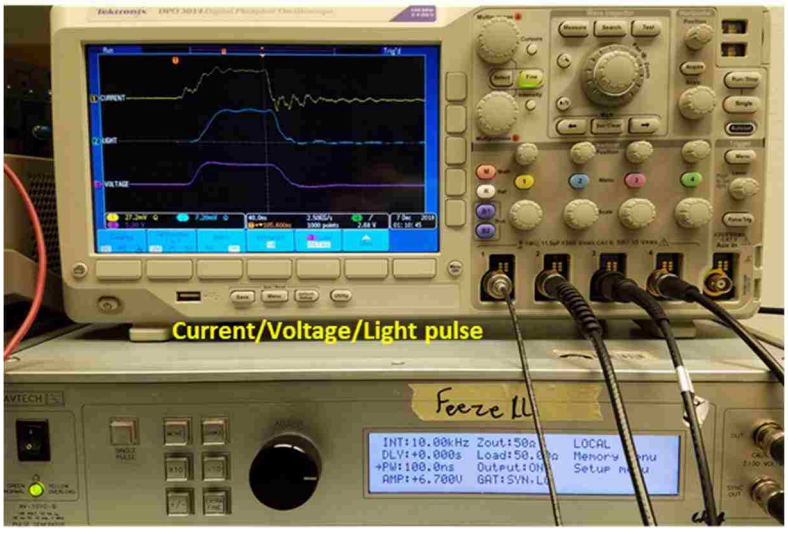

CW normal incidence optical pumping setup.

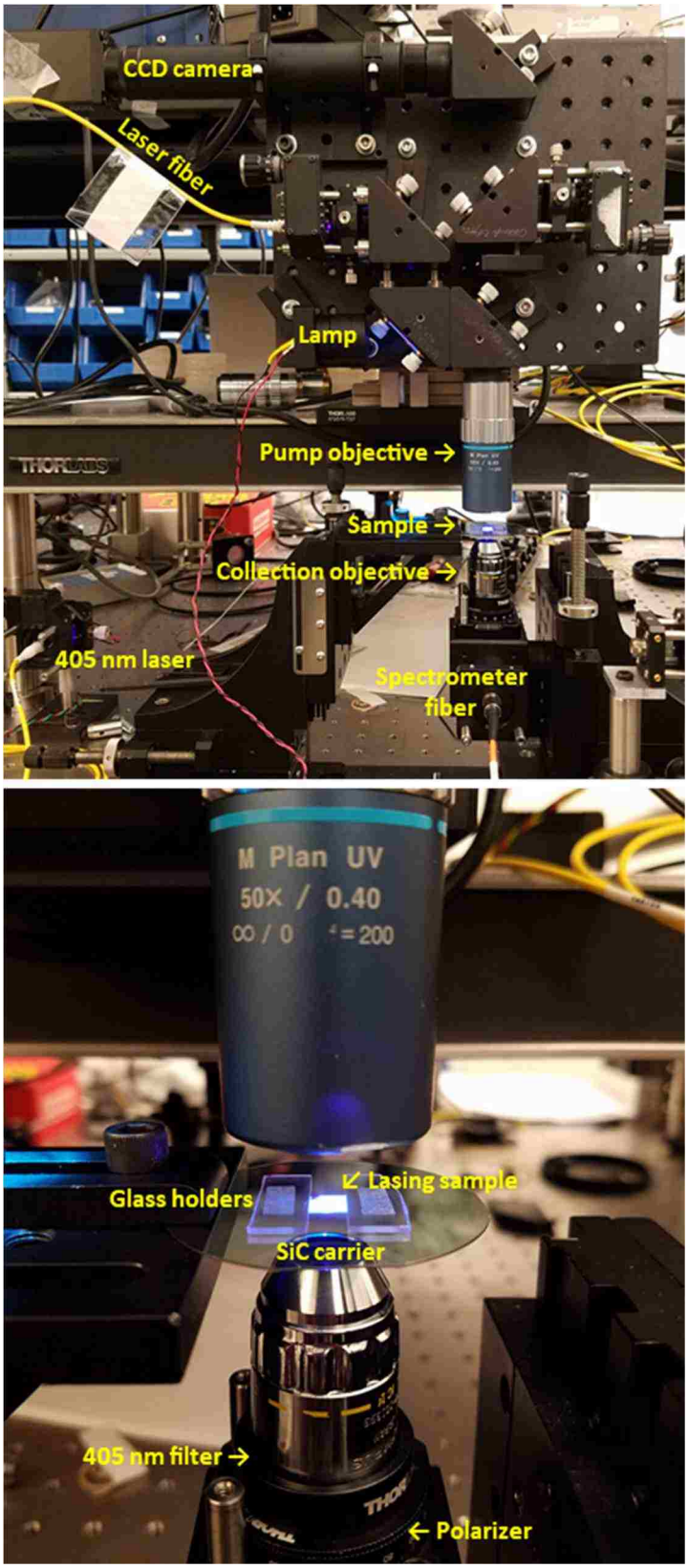

Electrochemical (EC) etching setup.

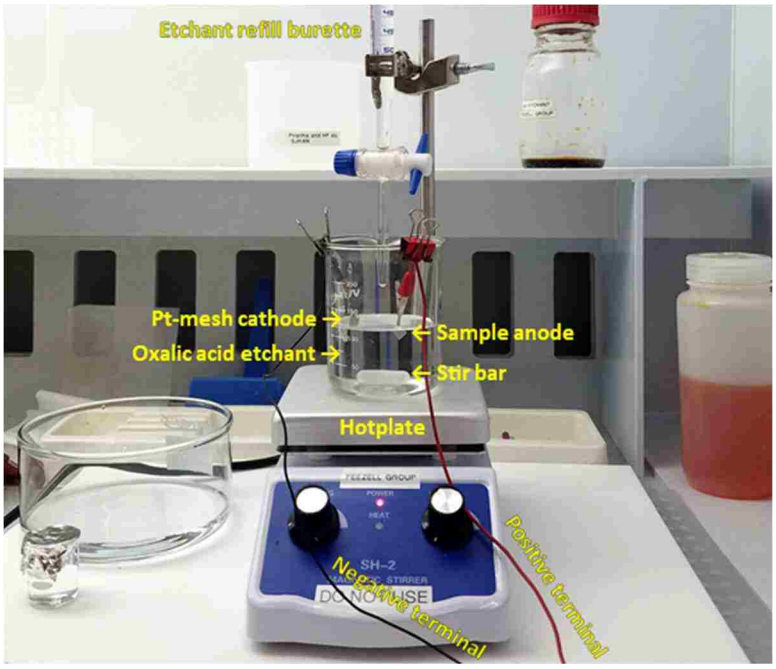

Photoelectrochemical (PEC) etching setup

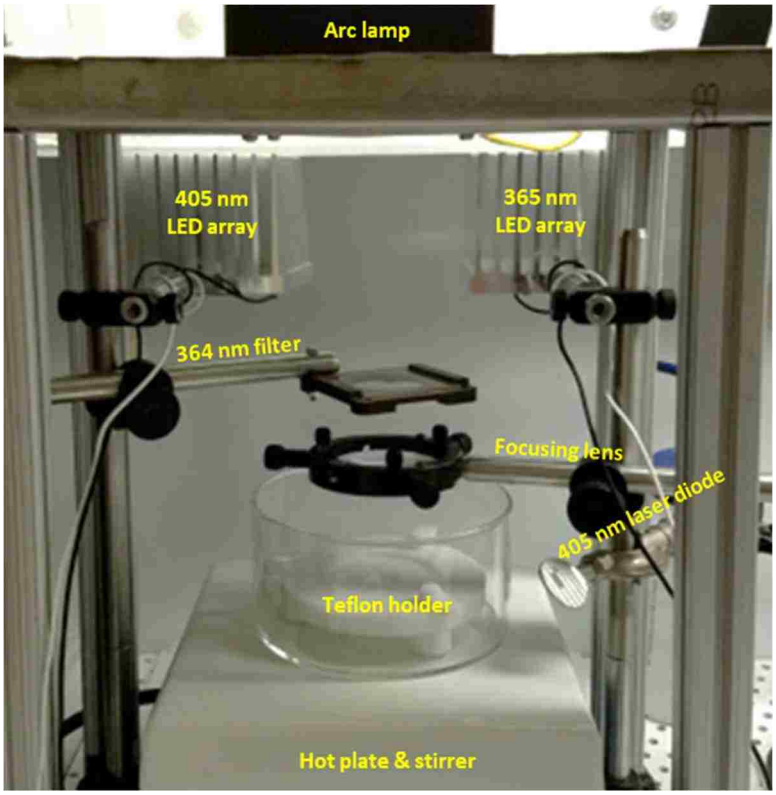

A.7 Time domain thermo-reflectance (TDTR) fitting

Measurements and fitting performed by Jin Gu Kang in Prof. Cahill's group at UIUC.

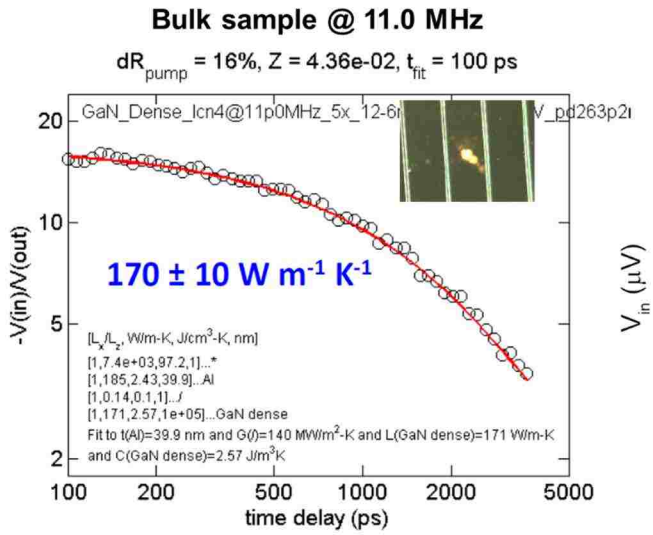

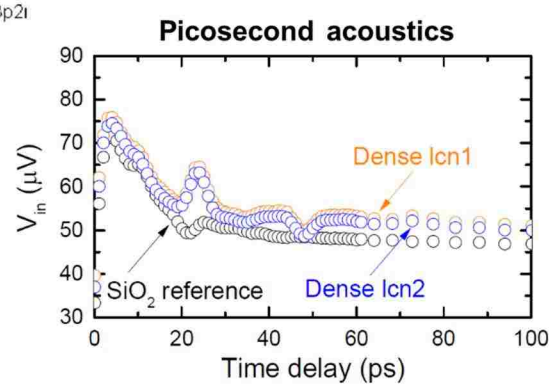

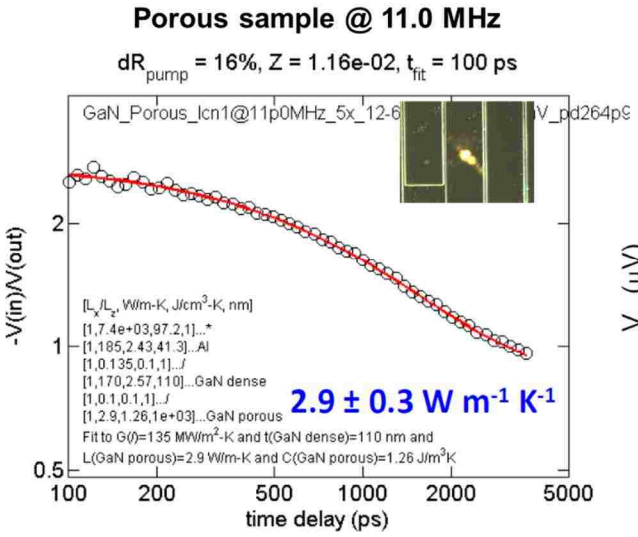

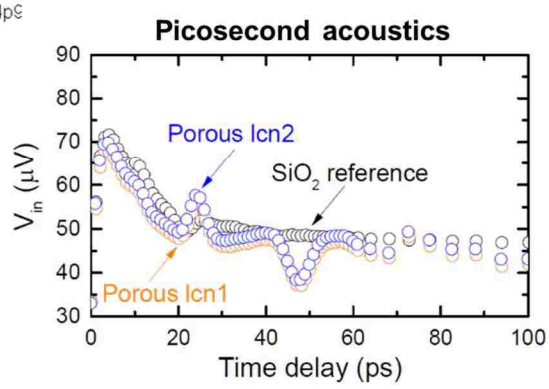

References

1. H. Soda, K. Iga, C. Kitahara, and Y. Suematsu, "GaInAsP/InP Surface Emitting Injection Lasers," Jpn. J. Appl. Phys. **18**, 2329 (1979).

2. K. Iga, "Surface-emitting laser-its birth and generation of new optoelectronics field," IEEE Journal of Selected Topics in Quantum Electronics **6**, 1201–1215 (2000).

3. J. A. Tatum, "Evolution of VCSELs," in *SPIE OPTO*, J. K. Guenter and C. Lei, eds. (2014), p. 90010C.

4. H. Amano, M. Kito, K. Hiramatsu, and I. Akasaki, "P-Type Conduction in Mg-Doped GaN Treated with Low-Energy Electron Beam Irradiation (LEEBI)," Jpn. J. Appl. Phys. **28**, L2112 (1989).

5. S. Nakamura, T. Mukai, and M. Senoh, "Candela-class high-brightness InGaN/AlGaN double-heterostructure blue-light-emitting diodes," Appl. Phys. Lett. **64**, 1687–1689 (1994).

6. F. A. Ponce and D. P. Bour, "Nitride-based semiconductors for blue and green light-emitting devices," Nature **386**, 351 (1997).

7. S. F. Chichibu, A. Uedono, T. Onuma, B. A. Haskell, A. Chakraborty, T. Koyama, P. T. Fini, S. Keller, S. P. DenBaars, J. S. Speck, U. K. Mishra, S. Nakamura, S. Yamaguchi, S. Kamiyama, H. Amano, I. Akasaki, J. Han, and T. Sota, "Origin of defect-insensitive emission probability in In-containing (Al,In,Ga)N alloy semiconductors," Nature Materials **5**, 810–816 (2006).

8. R. Michalzik, *VCSELs: Fundamentals, Technology and Applications of Vertical-Cavity Surface-Emitting Lasers* (Springer, 2012).

9. L. A. Coldren, S. W. Corzine, and M. L. Mashanovitch, *Diode Lasers and Photonic Integrated Circuits* (John Wiley & Sons, 2012).

10. J.-F. Seurin, "Harnessing light for high-power applications | SPIE Homepage: SPIE," http://spie.org/newsroom/1638-harnessing-light-for-high-power-applications?SSO=1.

11. J. T. Leonard, "III-Nitride Vertical-Cavity Surface-Emitting Lasers," Ph.D., University of California, Santa Barbara (2016).

12. E. R. Hegblom, D. I. Babic, B. J. Thibeault, and L. A. Coldren, "Scattering losses from dielectric apertures in vertical-cavity lasers," IEEE Journal of Selected Topics in Quantum Electronics **3**, 379–389 (1997).

13. R. M. Farrell, D. A. Haeger, P. S. Hsu, K. Fujito, D. F. Feezell, S. P. DenBaars, J. S. Speck, and S. Nakamura, "Determination of internal parameters for AlGaN-cladding-free m-plane InGaN/GaN laser diodes," Appl. Phys. Lett. **99**, 171115 (2011).

14. S. W. Corzine, R. H. Yan, and L. A. Coldren, "A tanh substitution technique for the analysis of abrupt and graded interface multilayer dielectric stacks," IEEE Journal of Quantum Electronics **27**, 2086–2090 (1991).

15. C. Bayo and M. Ángel, "Theory of elasticity and electric polarization effects in the group-III nitrides," (2013).

16. F. Bernardini and V. Fiorentini, "Spontaneous versus Piezoelectric Polarization in III–V Nitrides: Conceptual Aspects and Practical Consequences," physica status solidi (b) **216**, 391–398 (1999).

17. B. Gil, "Basic Crystallography and Other Properties Linked with Symmetry," in *Physics of Wurtzite Nitrides and Oxides: Passport to Devices*, B. Gil, ed., Springer Series in Materials Science (Springer International Publishing, 2014), pp. 1–48.

18. M. Monavarian, A. Rashidi, and D. Feezell, "A Decade of Nonpolar and Semipolar III-Nitrides: A Review of Successes and Challenges," physica status solidi (a) **216**, (2019).

19. D. F. Feezell, J. S. Speck, S. P. DenBaars, and S. Nakamura, "Semipolar (20-2-1) InGaN/GaN Light-Emitting Diodes for High-Efficiency Solid-State Lighting," J. Display Technol., JDT **9**, 190–198 (2013).

20. E. F. Schubert, "Light-Emitting Diodes," in *Wiley Encyclopedia of Electrical and Electronics Engineering* (American Cancer Society, 2014), pp. 1–10.

21. A. E. Romanov, T. J. Baker, S. Nakamura, and J. S. Speck, "Strain-induced polarization in wurtzite III-nitride semipolar layers," Journal of Applied Physics **100**, 023522 (2006).

22. M. Meneghini, G. Meneghesso, and E. Zanoni, "Electrical Properties, Reliability Issues, and ESD Robustness of InGaN-Based LEDs," in *III-Nitride Based Light Emitting Diodes and Applications*, T.-Y. Seong, J. Han, H. Amano, and H. Morkoç, eds., Topics in Applied Physics (Springer Singapore, 2017), pp. 363–395.

23. W. G. Scheibenzuber, U. T. Schwarz, R. G. Veprek, B. Witzigmann, and A. Hangleiter, "Calculation of optical eigenmodes and gain in semipolar and nonpolar InGaN/GaN laser diodes," Phys. Rev. B **80**, 115320 (2009).

24. L. Schade, U. T. Schwarz, T. Wernicke, M. Weyers, and M. Kneissl, "Impact of band structure and transition matrix elements on polarization properties of the

photoluminescence of semipolar and nonpolar InGaN quantum wells," physica status solidi (b) **248**, 638–646 (2011).

25. S.-H. Park, "Crystal Orientation Effects on Many-Body Optical Gain of Wurtzite InGaN/GaN Quantum Well Lasers," Jpn. J. Appl. Phys. **42**, L170 (2003).

26. S.-H. Park, "Crystal orientation effects on electronic properties of wurtzite InGaN/GaN quantum wells," Journal of Applied Physics **91**, 9904–9908 (2002).

27. S. Park, D. Ahn, and S. Chuang, "Electronic and Optical Properties of a- and m-Plane Wurtzite InGaN–GaN Quantum Wells," IEEE Journal of Quantum Electronics **43**, 1175–1182 (2007).

28. Z. Q. Li, Z. M. S. Li, and J. Piprek, "Simulations of laser diodes with nonpolar InGaN multi-quantum-wells," physica status solidi c **7**, 2259–2261 (2010).

29. W. G. Scheibenzuber and U. T. Schwarz, "Polarization switching of the optical gain in semipolar InGaN quantum wells," physica status solidi (b) **248**, 647–651 (2011).

30. T. Melo, Y.-L. Hu, C. Weisbuch, M. C. Schmidt, A. David, B. Ellis, C. Poblenz, Y.-D. Lin, M. R. Krames, and J. W. Raring, "Gain comparison in polar and nonpolar/semipolar gallium-nitride-based laser diodes," Semicond. Sci. Technol. **27**, 024015 (2012).

31. S.-H. Park, "Piezoelectric and Spontaneous Polarization Effects on Many-Body Optical Gain of Wurtzite InGaN/GaN Quantum Well with Arbitrary Crystal Orientation," Jpn. J. Appl. Phys. **42**, 5052 (2003).

32. L. Schade, U. T. Schwarz, T. Wernicke, J. Rass, S. Ploch, M. Weyers, and M. Kneissl, "On the optical polarization properties of semipolar InGaN quantum wells," Appl. Phys. Lett. **99**, 051103 (2011).

33. W. W. Chow and M. H. Crawford, "Analysis of lasers as a solution to efficiency droop in solid-state lighting," Appl. Phys. Lett. **107**, 141107 (2015).

34. J. J. Wierer and J. Y. Tsao, "Advantages of III-nitride laser diodes in solid-state lighting," physica status solidi (a) **212**, 980–985 (2015).

35. K. A. Denault, M. Cantore, S. Nakamura, S. P. DenBaars, and R. Seshadri, "Efficient and stable laser-driven white lighting," AIP Advances **3**, 072107 (2013).

36. R. R. Hainich and O. Bimber, *Displays: Fundamentals and Applications* (CRC Press, 2016).

37. C. Lee, C. Shen, H. M. Oubei, M. Cantore, B. Janjua, T. K. Ng, R. M. Farrell, M. M. El-Desouki, J. S. Speck, S. Nakamura, B. S. Ooi, and S. P. DenBaars, "2 Gbit/s data transmission from an unfiltered laser-based phosphor-converted white lighting communication system," Opt. Express, OE **23**, 29779–29787 (2015).

38. K. Austen, "What could derail the wearables revolution?," Nature **525**, 22–24 (2015).

39. J. J. D. McKendry, R. P. Green, A. E. Kelly, Z. Gong, B. Guilhabert, D. Massoubre, E. Gu, and M. D. Dawson, "High-Speed Visible Light Communications Using Individual Pixels in a Micro Light-Emitting Diode Array," IEEE Photonics Technology Letters **22**, 1346–1348 (2010).

40. I. Takai, T. Harada, M. Andoh, K. Yasutomi, K. Kagawa, and S. Kawahito, "Optical Vehicle-to-Vehicle Communication System Using LED Transmitter and Camera Receiver," IEEE Photonics Journal **6**, 1–14 (2014).

41. C. Lee, C. Zhang, M. Cantore, R. M. Farrell, S. H. Oh, T. Margalith, J. S. Speck, S. Nakamura, J. E. Bowers, and S. P. DenBaars, "4 Gbps direct modulation of 450 nm GaN laser for high-speed visible light communication," Opt. Express, OE **23**, 16232–16237 (2015).

42. S. Watson, M. Tan, S. P. Najda, P. Perlin, M. Leszczynski, G. Targowski, S. Grzanka, and A. E. Kelly, "Visible light communications using a directly modulated 422 nm GaN laser diode," Opt. Lett., OL **38**, 3792–3794 (2013).

43. V. V. Rampal, "Blue Green Lasers and Their Military Potential," 1 **33**, 183–193 (1983).

44. T. Kondo, K. Takeda, H. Otoma, A. Murakami, J. Sakurai, H. Nakayama, X. Gu, and F. Koyama, "Developments of VCSELs for printers and optical communications at Fuji Xerox," in *Vertical-Cavity Surface-Emitting Lasers XX* (International Society for Optics and Photonics, 2016), Vol. 9766, p. 97660C.

45. N. Ueki and N. Mukoyama, "VCSEL-Based Laser Printing System," in *VCSELs: Fundamentals, Technology and Applications of Vertical-Cavity Surface-Emitting Lasers*, R. Michalzik, ed., Springer Series in Optical Sciences (Springer Berlin Heidelberg, 2013), pp. 539–548.

46. N. Mukoyama, H. Otoma, J. Sakurai, N. Ueki, and H. Nakayama, "VCSEL array-based light exposure system for laser printing," in *Vertical-Cavity Surface-Emitting Lasers XII* (International Society for Optics and Photonics, 2008), Vol. 6908, p. 69080H.

47. D. F. Feezell, "Status and future of GaN-based vertical-cavity surface-emitting lasers," in *Gallium Nitride Materials and Devices X* (International Society for Optics and Photonics, 2015), Vol. 9363, p. 93631G.

48. H. Yu, Z. Zheng, Y. Mei, R. Xu, J. Liu, H. Yang, B. Zhang, T. Lu, and H. Kuo, "Progress and prospects of GaN-based VCSEL from near UV to green emission," Progress in Quantum Electronics **57**, 1–19 (2018).

49. A. Mowla, T. Taimre, Y. L. Lim, K. Bertling, S. J. Wilson, T. W. Prow, H. P. Soyer, and A. D. Rakić, "Concurrent Reflectance Confocal Microscopy and Laser Doppler Flowmetry to Improve Skin Cancer Imaging: A Monte Carlo Model and Experimental Validation," Sensors **16**, 1411 (2016).

50. "Optical Nanoantennas Set the Stage for a NEMS Lab-on-a-Chip Revolution," AIP Publishing LLC (2015).

51. V. Poher, N. Grossman, G. T. Kennedy, K. Nikolic, H. X. Zhang, Z. Gong, E. M. Drakakis, E. Gu, M. D. Dawson, P. M. W. French, P. Degenaar, and M. A. A. Neil, "Micro-LED arrays: a tool for two-dimensional neuron stimulation," J. Phys. D: Appl. Phys. **41**, 094014 (2008).

52. S. P. Najda, P. Perlin, M. Leszczyński, T. J. Slight, W. Meredith, M. Schemmann, H. Moseley, J. A. Woods, R. Valentine, S. Kalra, P. Mossey, E. Theaker, M. Macluskey, G. Mimnagh, and W. Mimnagh, "A multi-wavelength (u.v. to visible) laser system for early detection of oral cancer," in *Imaging, Manipulation, and Analysis of Biomolecules, Cells, and Tissues XIII* (International Society for Optics and Photonics, 2015), Vol. 9328, p. 932809.

53. T. Vo-Dinh, M. Panjehpour, B. F. Overholt, C. Farris, F. P. Buckley, and R. Sneed, "In vivo cancer diagnosis of the esophagus using differential normalized fluorescence (DNF) indices," Lasers in Surgery and Medicine **16**, 41–47 (1995).

54. M. Panjehpour, C. E. Julius, M. N. Phan, T. Vo-Dinh, and S. Overholt, "Laser-induced fluorescence spectroscopy for in vivo diagnosis of non-melanoma skin cancers," Lasers in Surgery and Medicine **31**, 367–373 (2002).

55. Will Krzewick, "Chip Scale Atomic Clocks: Effects on Timing Error – Temperature (Part 3 of 4) « Microsemi," (n.d.).

56. "The tick-tock of the optical clock," https://phys.org/news/2012-03-tick-tock-optical-clock.html.

57. R. Lutwak, *The Chip-Scale Atomic Clock - Prototype Evaluation* (PN, 2007).

58. N. A. and S. Administration, ed., *NASA's Journey to Mars: Pioneering Next Steps in Space Exploration* (U.S. National Aeronautics and Space Administration, 2016).

59. D. K. Serkland, K. M. Geib, G. M. Peake, R. Lutwak, A. Rashed, M. Varghese, G. Tepolt, and M. Prouty, "VCSELs for atomic sensors," in *Vertical-Cavity Surface-Emitting Lasers XI* (International Society for Optics and Photonics, 2007), Vol. 6484, p. 648406.

60. K. Matsubara, K. Hayasaka, Y. Li, H. Ito, S. Nagano, M. Kajita, and M. Hosokawa, "Frequency Measurement of the Optical Clock Transition of 40Ca+ Ions with an Uncertainty of 10-14 Level," Appl. Phys. Express **1**, 067011 (2008).

61. C. Lacroûte, M. Souidi, P.-Y. Bourgeois, J. Millo, K. Saleh, E. Bigler, R. Boudot, V. Giordano, and Y. Kersalé, "Compact Yb+ optical atomic clock project: design principle and current status," J. Phys.: Conf. Ser. **723**, 012025 (2016).

62. T.-C. Lu, S.-W. Chen, T.-T. Wu, P.-M. Tu, C.-K. Chen, C.-H. Chen, Z.-Y. Li, H.-C. Kuo, and S.-C. Wang, "Continuous wave operation of current injected GaN vertical cavity surface emitting lasers at room temperature," Appl. Phys. Lett. **97**, 071114 (2010).

63. G. Cosendey, A. Castiglia, G. Rossbach, J.-F. Carlin, and N. Grandjean, "Blue monolithic AlInN-based vertical cavity surface emitting laser diode on free-standing GaN substrate," Appl. Phys. Lett. **101**, 151113 (2012).

64. D. H. Hsieh, A. J. Tzou, T. S. Kao, F. I. Lai, D. W. Lin, B. C. Lin, T. C. Lu, W. C. Lai, C. H. Chen, and H. C. Kuo, "Improved carrier injection in GaN-based VCSEL via AlGaN/GaN multiple quantum barrier electron blocking layer," Opt. Express, OE **23**, 27145–27151 (2015).

65. T. Furuta, K. Matsui, K. Horikawa, K. Ikeyama, Y. Kozuka, S. Yoshida, T. Akagi, T. Takeuchi, S. Kamiyama, M. Iwaya, and I. Akasaki, "Room-temperature CW operation of a nitride-based vertical-cavity surface-emitting laser using thick GaInN quantum wells," Jpn. J. Appl. Phys. **55**, 05FJ11 (2016).

66. T. Furuta, K. Matsui, Y. Kozuka, S. Yoshida, N. Hayasi, T. Akagi, N. Koide, T. Takeuchi, S. Kamiyama, M. Iwaya, and I. Akasaki, "1.7-mW nitride-based vertical-cavity surface-emitting lasers using AlInN/GaN bottom DBRs," in *2016 International Semiconductor Laser Conference (ISLC)* (2016), pp. 1–2.

67. K. Matsui, T. Furuta, N. Hayashi, Y. Kozuka, T. Akagi, T. Takeuchi, S. Kamiyama, M. Iwaya, and I. Akasaki, "3-mW RT-CW GaN-based VCSELs and their temperature dependance," in (2016), p. B1.1.04.

68. T. Takeuchi, S. Kamiyama, M. Iwaya, and I. Akasaki, "GaInN vertical-cavity surface-emitting lasers with AlInN/GaN DBRs," in *12th International Conference on Nitride Semiconductors* (2017), p. B 9.1.

69. N. Hayashi, J. Ogimoto, K. Matsui, T. Furuta, T. Akagi, S. Iwayama, T. Takeuchi, S. Kamiyama, M. Iwaya, and I. Akasaki, "A GaN-Based VCSEL with a Convex Structure for Optical Guiding," physica status solidi (a) **215**, 1700648 (2018).

70. M. Kuramoto, S. Kobayashi, T. Akagi, K. Tazawa, K. Tanaka, T. Saito, and T. Takeuchi, "Enhancement of slope efficiency and output power in GaN-based vertical-cavity surface-emitting lasers with a SiO2-buried lateral index guide," Appl. Phys. Lett. **112**, 111104 (2018).

71. M. Kuramoto, S. Kobayashi, T. Akagi, K. Tazawa, K. Tanaka, T. Saito, and T. Takeuchi, "High-output-power and high-temperature operation of blue GaN-based vertical-cavity surface-emitting laser," Appl. Phys. Express **11**, 112101 (2018).

72. Y. Higuchi, K. Omae, H. Matsumura, and T. Mukai, "Room-Temperature CW Lasing of a GaN-Based Vertical-Cavity Surface-Emitting Laser by Current Injection," Appl. Phys. Express **1**, 121102 (2008).

73. K. Omae, Y. Higuchi, K. Nakagawa, H. Matsumura, and T. Mukai, "Improvement in Lasing Characteristics of GaN-based Vertical-Cavity Surface-Emitting Lasers Fabricated Using a GaN Substrate," Appl. Phys. Express **2**, 052101 (2009).

74. D. Kasahara, D. Morita, T. Kosugi, K. Nakagawa, J. Kawamata, Y. Higuchi, H. Matsumura, and T. Mukai, "Demonstration of Blue and Green GaN-Based Vertical-Cavity Surface-Emitting Lasers by Current Injection at Room Temperature," Appl. Phys. Express **4**, 072103 (2011).

75. T. Onishi, O. Imafuji, K. Nagamatsu, M. Kawaguchi, K. Yamanaka, and S. Takigawa, "Continuous Wave Operation of GaN Vertical Cavity Surface Emitting Lasers at Room Temperature," IEEE Journal of Quantum Electronics **48**, 1107–1112 (2012).

76. C. Holder, J. S. Speck, S. P. DenBaars, S. Nakamura, and D. Feezell, "Demonstration of Nonpolar GaN-Based Vertical-Cavity Surface-Emitting Lasers," Appl. Phys. Express **5**, 092104 (2012).

77. W.-J. Liu, X.-L. Hu, L.-Y. Ying, J.-Y. Zhang, and B.-P. Zhang, "Room temperature continuous wave lasing of electrically injected GaN-based vertical cavity surface emitting lasers," Appl. Phys. Lett. **104**, 251116 (2014).

78. C. O. Holder, J. T. Leonard, R. M. Farrell, D. A. Cohen, B. Yonkee, J. S. Speck, S. P. DenBaars, S. Nakamura, and D. F. Feezell, "Nonpolar III-nitride vertical-cavity

surface emitting lasers with a polarization ratio of 100% fabricated using photoelectrochemical etching," Appl. Phys. Lett. **105**, 031111 (2014).

79. S. Izumi, N. Fuutagawa, T. Hamaguchi, M. Murayama, M. Kuramoto, and H. Narui, "Room-temperature continuous-wave operation of GaN-based vertical-cavity surface-emitting lasers fabricated using epitaxial lateral overgrowth," Appl. Phys. Express **8**, 062702 (2015).

80. J. T. Leonard, D. A. Cohen, B. P. Yonkee, R. M. Farrell, T. Margalith, S. Lee, S. P. DenBaars, J. S. Speck, and S. Nakamura, "Nonpolar III-nitride vertical-cavity surface-emitting lasers incorporating an ion implanted aperture," Appl. Phys. Lett. **107**, 011102 (2015).

81. J. T. Leonard, E. C. Young, B. P. Yonkee, D. A. Cohen, T. Margalith, S. P. DenBaars, J. S. Speck, and S. Nakamura, "Demonstration of a III-nitride vertical-cavity surface-emitting laser with a III-nitride tunnel junction intracavity contact," Appl. Phys. Lett. **107**, 091105 (2015).

82. T. Hamaguchi, N. Fuutagawa, S. Izumi, M. Murayama, and H. Narui, "Milliwatt-class GaN-based blue vertical-cavity surface-emitting lasers fabricated by epitaxial lateral overgrowth," physica status solidi (a) **213**, 1170–1176 (2016).

83. J. T. Leonard, B. P. Yonkee, D. A. Cohen, L. Megalini, S. Lee, J. S. Speck, S. P. DenBaars, and S. Nakamura, "Nonpolar III-nitride vertical-cavity surface-emitting laser with a photoelectrochemically etched air-gap aperture," Appl. Phys. Lett. **108**, 031111 (2016).

84. G. Weng, Y. Mei, J. Liu, W. Hofmann, L. Ying, J. Zhang, Y. Bu, Z. Li, H. Yang, and B. Zhang, "Low threshold continuous-wave lasing of yellow-green InGaN-QD vertical-cavity surface-emitting lasers," Opt. Express, OE **24**, 15546–15553 (2016).

85. C. Shen, J. T. Leonard, E. C. Young, T. K. Ng, S. P. DenBaars, J. S. Speck, S. Nakamura, A. Y. Alyamani, M. M. El-Desouki, and B. S. Ooi, "GHz modulation bandwidth from single-longitudinal mode violet-blue VCSEL using nonpolar InGaN/GaN QWs," in *2016 Conference on Lasers and Electro-Optics (CLEO)* (2016), pp. 1–2.

86. T. Hamaguchi, H. Nakajima, M. Ito, J. Mitomo, S. Satou, N. Fuutagawa, and H. Narui, "Lateral carrier confinement of GaN-based vertical-cavity surface-emitting diodes using boron ion implantation," Jpn. J. Appl. Phys. **55**, 122101 (2016).

87. Y. Mei, G.-E. Weng, B.-P. Zhang, J.-P. Liu, W. Hofmann, L.-Y. Ying, J.-Y. Zhang, Z.-C. Li, H. Yang, and H.-C. Kuo, "Quantum dot vertical-cavity surface-emitting lasers covering the 'green gap,'" Light: Science & Applications **6**, e16199 (2017).

88. T.-C. Chang, S.-Y. Kuo, J.-T. Lian, K.-B. Hong, S.-C. Wang, and T.-C. Lu, "High-temperature operation of GaN-based vertical-cavity surface-emitting lasers," Appl. Phys. Express **10**, 112101 (2017).

89. C. A. Forman, S. Lee, E. C. Young, J. A. Kearns, D. A. Cohen, J. T. Leonard, T. Margalith, S. P. DenBaars, and S. Nakamura, "Continuous-wave operation of m-plane GaN-based vertical-cavity surface-emitting lasers with a tunnel junction intracavity contact," Appl. Phys. Lett. **112**, 111106 (2018).

90. S. Lee, C. A. Forman, C. Lee, J. Kearns, E. C. Young, J. T. Leonard, D. A. Cohen, J. S. Speck, S. Nakamura, and S. P. DenBaars, "GaN-based vertical-cavity surface-emitting lasers with tunnel junction contacts grown by metal-organic chemical vapor deposition," Appl. Phys. Express **11**, 062703 (2018).

91. R. Xu, Y. Mei, H. Xu, L. Ying, Z. Zheng, H. Long, D. Zhang, B. Zhang, and J. Liu, "Green Vertical-Cavity Surface-Emitting Lasers Based on Combination of Blue-Emitting Quantum Wells and Cavity-Enhanced Recombination," IEEE Transactions on Electron Devices **65**, 4401–4406 (2018).

92. T. Hamaguchi, M. Tanaka, J. Mitomo, H. Nakajima, M. Ito, M. Ohara, N. Kobayashi, K. Fujii, H. Watanabe, S. Satou, R. Koda, and H. Narui, "Lateral optical confinement of GaN-based VCSEL using an atomically smooth monolithic curved mirror," Scientific Reports **8**, 10350 (2018).

93. T. Hamaguchi, H. Nakajima, M. Tanaka, M. Ito, M. Ohara, T. Jyoukawa, N. Kobayashi, T. Matou, K. Hayashi, H. Watanabe, R. Koda, and K. Yanashima, "Sub-milliampere-threshold continuous wave operation of GaN-based vertical-cavity surface-emitting laser with lateral optical confinement by curved mirror," Appl. Phys. Express **12**, 044004 (2019).

94. U. Kaufmann, P. Schlotter, H. Obloh, K. Köhler, and M. Maier, "Hole conductivity and compensation in epitaxial GaN:Mg layers," Phys. Rev. B **62**, 10867–10872 (2000).

95. D. Sizov, R. Bhat, and C. Zah, "Optical absorption of Mg-doped layers and InGaN quantum wells on c-plane and semipolar GaN structures," Journal of Applied Physics **113**, 203108 (2013).

96. E. Kioupakis, P. Rinke, and C. G. V. de Walle, "Determination of Internal Loss in Nitride Lasers from First Principles," Appl. Phys. Express **3**, 082101 (2010).

97. C. J. Eiting, P. A. Grudowski, and R. D. Dupuis, "Growth of low resistivity p-type GaN by metal organic chemical vapour deposition," Electronics Letters **33**, 1987–1989 (1997).

98. N. Watanabe, T. Kimoto, and J. Suda, "The temperature dependence of the refractive indices of GaN and AlN from room temperature up to 515 °C," Journal of Applied Physics **104**, 106101 (2008).

99. S. Strite and H. Morkoç, "GaN, AlN, and InN: A review," Journal of Vacuum Science & Technology B: Microelectronics and Nanometer Structures Processing, Measurement, and Phenomena **10**, 1237–1266 (1992).

100. T. Lu, J. Chen, S. Chen, H. Kuo, C. Kuo, C. Lee, and S. Wang, "Development of GaN-Based Vertical-Cavity Surface-Emitting Lasers," IEEE Journal of Selected Topics in Quantum Electronics **15**, 850–860 (2009).

101. M. Imura, K. Nakano, N. Fujimoto, N. Okada, K. Balakrishnan, M. Iwaya, S. Kamiyama, H. Amano, I. Akasaki, T. Noro, T. Takagi, and A. Bandoh, "High-Temperature Metal-Organic Vapor Phase Epitaxial Growth of AlN on Sapphire by Multi Transition Growth Mode Method Varying V/III Ratio," Jpn. J. Appl. Phys. **45**, 8639 (2006).

102. A. Yamamoto, Y. Murakami, K. Koide, M. Adachi, and A. Hashimoto, "Growth Temperature Dependences of MOVPE InN on Sapphire Substrates," physica status solidi (b) **228**, 5–8 (2001).

103. R. Butté, J.-F. Carlin, E. Feltin, M. Gonschorek, S. Nicolay, G. Christmann, D. Simeonov, A. Castiglia, J. Dorsaz, H. J. Buehlmann, S. Christopoulos, G. B. H. von Hög, A. J. D. Grundy, M. Mosca, C. Pinquier, M. A. Py, F. Demangeot, J. Frandon, P. G. Lagoudakis, J. J. Baumberg, and N. Grandjean, "Current status of AlInN layers lattice-matched to GaN for photonics and electronics," J. Phys. D: Appl. Phys. **40**, 6328–6344 (2007).

104. T. Aschenbrenner, H. Dartsch, C. Kruse, M. Anastasescu, M. Stoica, M. Gartner, A. Pretorius, A. Rosenauer, T. Wagner, and D. Hommel, "Optical and structural characterization of AlInN layers for optoelectronic applications," Journal of Applied Physics **108**, 063533 (2010).

105. J. Piprek, *Nitride Semiconductor Devices: Principles and Simulation* (John Wiley & Sons, 2007).

106. M. N. Polyanskiy, "Refractive index database," https://refractiveindex.info (2019).

107. S. Lee, S. Mishkat-Ul-Masabih, J. T. Leonard, D. F. Feezell, D. A. Cohen, J. S. Speck, S. Nakamura, and S. P. DenBaars, "Smooth and selective photo-electrochemical etching of heavily doped GaN:Si using a mode-locked 355 nm microchip laser," Appl. Phys. Express **10**, 011001 (2016).

108. Saadat Mishkat-Ul-Masabih, Andrew Aragon, Morteza Monavarian, Daniel, and Feezell, "Effect of Mask Orientation and Growth Parameters on the Epitaxial Lateral Overgrowth of GaN on Free-Standing Nonpolar Substrates," in *21st American Conference on Crystal Growth and Epitaxy* (2017), pp. P1-27.

109. Stanislav Vitanov, "Simulation of High Electron Mobility Transistors," Dissertation, Vienna University of Technology (2010).

110. B. N. Pantha, R. Dahal, J. Li, J. Y. Lin, H. X. Jiang, and G. Pomrenke, "Thermoelectric properties of InxGa1−xN alloys," Appl. Phys. Lett. **92**, 042112 (2008).

111. W. Liu and A. A. Balandin, "Thermoelectric effects in wurtzite GaN and AlxGa1−xN alloys," Journal of Applied Physics **97**, 123705 (2005).

112. J. Zou, D. Kotchetkov, A. A. Balandin, D. I. Florescu, and F. H. Pollak, "Thermal conductivity of GaN films: Effects of impurities and dislocations," Journal of Applied Physics **92**, 2534–2539 (2002).

113. D. Thuau, I. Koymen, and R. Cheung, "A Microstructure for Thermal Conductivity Measurement of Conductive Thin Films," Microelectron. Eng. **88**, 2408–2412 (2011).

114. A. Sarua, H. Ji, K. P. Hilton, D. J. Wallis, M. J. Uren, T. Martin, and M. Kuball, "Thermal Boundary Resistance Between GaN and Substrate in AlGaN/GaN Electronic Devices," IEEE Transactions on Electron Devices **54(12)**, 3152–3158 (2007).

115. S. M. Mishkat-Ul-Masabih, J. T. Leonard, D. A. Cohen, S. Nakamura, and D. F. Feezell, "Techniques to reduce thermal resistance in flip-chip GaN-based VCSELs," physica status solidi (a) **214**, 1600819 (2017).

116. R. Sharma, E. D. Haberer, C. Meier, E. L. Hu, and S. Nakamura, "Vertically oriented GaN-based air-gap distributed Bragg reflector structure fabricated using band-gap-selective photoelectrochemical etching," Appl. Phys. Lett. **87**, 051107 (2005).

117. R. Sharma, Y.-S. Choi, C.-F. Wang, A. David, C. Weisbuch, S. Nakamura, and E. L. Hu, "Gallium-nitride-based microcavity light-emitting diodes with air-gap distributed Bragg reflectors," Appl. Phys. Lett. **91**, 211108 (2007).

118. J. H. Ryu, H. Y. Kim, H. K. Kim, Y. S. Katharria, N. Han, J. H. Kang, Y. J. Park, M. Han, B. D. Ryu, K. B. Ko, E.-K. Suh, and C.-H. Hong, "High performance of InGaN light-emitting diodes by air-gap/GaN distributed Bragg reflectors," Opt. Express, OE **20**, 9999–10003 (2012).

119. M. Bellanger, V. Bousquet, G. Christmann, J. Baumberg, and M. Kauer, "Highly Reflective GaN-Based Air-Gap Distributed Bragg Reflectors Fabricated Using AlInN Wet Etching," Appl. Phys. Express **2**, 121003 (2009).

120. R. Tao, M. Arita, S. Kako, K. Kamide, and Y. Arakawa, "Strong coupling in non-polar GaN/AlGaN microcavities with air-gap/III-nitride distributed Bragg reflectors," Appl. Phys. Lett. **107**, 101102 (2015).

121. C. Zhang, S. H. Park, D. Chen, D.-W. Lin, W. Xiong, H.-C. Kuo, C.-F. Lin, H. Cao, and J. Han, "Mesoporous GaN for Photonic Engineering—Highly Reflective GaN Mirrors as an Example," ACS Photonics **2**, 980–986 (2015).

122. X. Yang, H. Xiao, D. Cao, C. Zhao, L. Shen, and J. Ma, "Fabrication, annealing, and regrowth of wafer-scale nanoporous GaN distributed Bragg reflectors," Scripta Materialia **156**, 10–13 (2018).

123. G.-J. Wang, B.-S. Hong, Y.-Y. Chen, Z.-J. Yang, T.-L. Tsai, Y.-S. Lin, and C.-F. Lin, "GaN/AlGaN ultraviolet light-emitting diode with an embedded porous-AlGaN distributed Bragg reflector," Appl. Phys. Express **10**, 122102 (2017).

124. J. Park, J.-H. Kang, and S.-W. Ryu, "High Diffuse Reflectivity of Nanoporous GaN Distributed Bragg Reflector Formed by Electrochemical Etching," Appl. Phys. Express **6**, 072201 (2013).

125. B.-C. Shieh, Y.-C. Jhang, K.-P. Huang, W.-C. Huang, J.-J. Dai, C.-F. Lai, and C.-F. Lin, "InGaN light-emitting diodes with embedded nanoporous GaN distributed Bragg reflectors," Appl. Phys. Express **8**, 082101 (2015).

126. G.-Y. Shiu, K.-T. Chen, F.-H. Fan, K.-P. Huang, W.-J. Hsu, J.-J. Dai, C.-F. Lai, and C.-F. Lin, "InGaN Light-Emitting Diodes with an Embedded Nanoporous GaN Distributed Bragg Reflectors," Scientific Reports **6**, 29138 (2016).

127. T. Braniste, J. Ciers, Ed. Monaico, D. Martin, J.-F. Carlin, V. V. Ursaki, V. V. Sergentu, I. M. Tiginyanu, and N. Grandjean, "Multilayer porous structures of HVPE and MOCVD grown GaN for photonic applications," Superlattices and Microstructures **102**, 221–234 (2017).

128. P. Griffin, T. Zhu, and R. Oliver, "Porous AlGaN-Based Ultraviolet Distributed Bragg Reflectors," Materials **11**, 1487 (2018).

129. S.-M. Lee, S.-H. Gong, J.-H. Kang, M. Ebaid, S.-W. Ryu, and Y.-H. Cho, "Optically pumped GaN vertical cavity surface emitting laser with high index-contrast nanoporous distributed Bragg reflector," Opt. Express, OE **23**, 11023–11030 (2015).

130. F.-H. Fan, Z.-Y. Syu, C.-J. Wu, Z.-J. Yang, B.-S. Huang, G.-J. Wang, Y.-S. Lin, H. Chen, C. H. Kao, and C.-F. Lin, "Ultraviolet GaN Light-Emitting Diodes with Porous-AlGaN Reflectors," Scientific Reports **7**, 4968 (2017).

131. C. Zhang, K. Xiong, G. Yuan, and J. Han, "A resonant-cavity blue–violet light-emitting diode with conductive nanoporous distributed Bragg reflector," physica status solidi (a) **214**, 1600866 (2017).

132. C. Zhang, G. Yuan, K. Xiong, S. H. Park, and J. Han, "New Directions in GaN Photonics Enabled by Electrochemical Processes," ECS Trans. **72**, 47–56 (2016).

133. D. Chen, H. Xiao, and J. Han, "Nanopores in GaN by electrochemical anodization in hydrofluoric acid: Formation and mechanism," Journal of Applied Physics **112**, 064303 (2012).

134. M. J. Schwab, D. Chen, J. Han, and L. D. Pfefferle, "Aligned Mesopore Arrays in GaN by Anodic Etching and Photoelectrochemical Surface Etching," J. Phys. Chem. C **117**, 16890–16895 (2013).

135. Y. Zhang, S.-W. Ryu, C. Yerino, B. Leung, Q. Sun, Q. Song, H. Cao, and J. Han, "A conductivity-based selective etching for next generation GaN devices," physica status solidi (b) **247**, 1713–1716 (2010).

136. C. Zhang, G. Yuan, A. Bruch, K. Xiong, H. X. Tang, and J. Han, "Toward Quantitative Electrochemical Nanomachining of III-Nitrides," J. Electrochem. Soc. **165**, E513–E520 (2018).

137. J. Park, K. M. Song, S.-R. Jeon, J. H. Baek, and S.-W. Ryu, "Doping selective lateral electrochemical etching of GaN for chemical lift-off," Appl. Phys. Lett. **94**, 221907 (2009).

138. T. Zhu, Y. Liu, T. Ding, W. Y. Fu, J. Jarman, C. X. Ren, R. V. Kumar, and R. A. Oliver, "Wafer-scale Fabrication of Non-Polar Mesoporous GaN Distributed Bragg Reflectors via Electrochemical Porosification," Scientific Reports **7**, 45344 (2017).

139. K. Fujito, K. Kiyomi, T. Mochizuki, H. Oota, H. Namita, S. Nagao, and I. Fujimura, "High-quality nonpolar m -plane GaN substrates grown by HVPE," physica status solidi (a) **205**, 1056–1059 (2008).

140. K. Fujito, S. Kubo, and I. Fujimura, "Development of Bulk GaN Crystals and Nonpolar/Semipolar Substrates by HVPE," MRS Bulletin **34**, 313–317 (2009).

141. A. Hirai, Z. Jia, M. C. Schmidt, R. M. Farrell, S. P. DenBaars, S. Nakamura, J. S. Speck, and K. Fujito, "Formation and reduction of pyramidal hillocks on m-plane {11$\bar{}$00} GaN," Appl. Phys. Lett. **91**, 191906 (2007).

142. H. Yamada, K. Iso, M. Saito, K. Fujito, S. P. DenBaars, J. S. Speck, and S. Nakamura, "Impact of Substrate Miscut on the Characteristic of m-plane InGaN/GaN Light Emitting Diodes," Jpn. J. Appl. Phys. **46**, L1117 (2007).

143. K. M. Kelchner, L. Y. Kuritzky, S. Nakamura, S. P. DenBaars, and J. S. Speck, "Stable vicinal step orientations in m-plane GaN," Journal of Crystal Growth **411**, 56–62 (2015).

144. R. M. Farrell, D. A. Haeger, X. Chen, C. S. Gallinat, R. W. Davis, M. Cornish, K. Fujito, S. Keller, S. P. DenBaars, S. Nakamura, and J. S. Speck, "Origin of pyramidal hillocks on GaN thin films grown on free-standing m-plane GaN substrates," Appl. Phys. Lett. **96**, 231907 (2010).

145. R. M. Farrell, "Growth, Fabrication, and Characterization of Continuous-Wave Aluminum Gallium Nitride -Cladding-Free m-plane Indium Gallium Nitride / Gallium Nitride Laser Diodes," Ph.D., University of California, Santa Barbara (2010).

146. D. D. Koleske, A. E. Wickenden, R. L. Henry, J. C. Culbertson, and M. E. Twigg, "GaN decomposition in H2 and N2 at MOVPE temperatures and pressures," Journal of Crystal Growth **223**, 466–483 (2001).

147. W. J. Tseng, D. H. van Dorp, R. R. Lietem, P. M. Vereecken, and G. Borghs, "Anodic Etching of n-GaN Epilayer into Porous GaN and Its Photoelectrochemical Properties," J. Phys. Chem. C **118**, 29492–29498 (2014).

148. C. Yang, L. Liu, S. Zhu, Z. Yu, X. Xi, S. Wu, H. Cao, J. Li, and L. Zhao, "GaN with Laterally Aligned Nanopores To Enhance the Water Splitting," J. Phys. Chem. C **121**, 7331–7336 (2017).

149. S. Mishkat-Ul-Masabih, T. S. Luk, A. Rishinaramangalam, M. Monavarian, M. Nami, and D. Feezell, "Nanoporous distributed Bragg reflectors on free-standing nonpolar m-plane GaN," Appl. Phys. Lett. **112**, 041109 (2018).

150. Y. Gao, M. D. Craven, J. S. Speck, S. P. Den Baars, and E. L. Hu, "Dislocation- and crystallographic-dependent photoelectrochemical wet etching of gallium nitride," Appl. Phys. Lett. **84**, 3322–3324 (2004).

151. M. M. Braun and L. Pilon, "Effective optical properties of non-absorbing nanoporous thin films," Thin Solid Films **496**, 505–514 (2006).

152. E. Matioli, S. Brinkley, K. M. Kelchner, S. Nakamura, S. DenBaars, J. Speck, and C. Weisbuch, "Polarized light extraction in m-plane GaN light-emitting diodes by embedded photonic-crystals," Appl. Phys. Lett. **98**, 251112 (2011).

153. E. Feltin, G. Christmann, J. Dorsaz, A. Castiglia, J. F. Carlin, R. Butté, N. Grandjean, S. Christopoulos, G. B. H. von Högersthal, A. J. D. Grundy, P. G. Lagoudakis, and J. J. Baumberg, "Blue lasing at room temperature in an optically pumped lattice-matched AlInN/GaN VCSEL structure," Electronics Letters **43**, 924–926 (2007).

154. J.-T. Chu, T. Lu, H.-H. Yao, C.-C. Kao, W.-D. Liang, J.-Y. Tsai, H. Kuo, and S.-C. Wang, "Room-Temperature Operation of Optically Pumped Blue-Violet GaN-Based Vertical-Cavity Surface-Emitting Lasers Fabricated by Laser Lift-Off," Jpn. J. Appl. Phys. **45**, 2556 (2006).

155. J. M. Redwing, D. A. S. Loeber, N. G. Anderson, M. A. Tischler, and J. S. Flynn, "An optically pumped GaN–AlGaN vertical cavity surface emitting laser," Appl. Phys. Lett. **69**, 1–3 (1996).

156. S.-C. Wang, T.-C. Lu, C.-C. Kao, J.-T. Chu, G.-S. Huang, H.-C. Kuo, S.-W. Chen, T.-T. Kao, J.-R. Chen, and L.-F. Lin, "Optically Pumped GaN-based Vertical Cavity Surface Emitting Lasers: Technology and Characteristics," Jpn. J. Appl. Phys. **46**, 5397 (2007).

157. J.-T. Chu, T.-C. Lu, M. You, B.-J. Su, C.-C. Kao, H.-C. Kuo, and S.-C. Wang, "Emission characteristics of optically pumped GaN-based vertical-cavity surface-emitting lasers," Appl. Phys. Lett. **89**, 121112 (2006).

158. H. Morkoç, *Nitride Semiconductors and Devices* (Springer Science & Business Media, 2013).

159. S. M. Mishkat-Ul-Masabih, T. S. Luk, M. Monavarian, and D. F. Feezell, "Polarization-pinned emission of a continuous-wave optically pumped nonpolar GaN-based VCSEL using nanoporous distributed Bragg reflectors," Opt. Express, OE **27**, 9495–9501 (2019).

160. S. M. Mishkat-Ul-Masabih, T. S. Luk, M. Monavarian, and D. F. Feezell, "Optically Pumped Polarization-Pinned GaN-Based Vertical-Cavity Surface-Emitting Lasers using Nanoporous Distributed Bragg Reflectors," in *2018 IEEE International Semiconductor Laser Conference (ISLC)* (2018), pp. 1–2.

161. H. Nagel, A. G. Aberle, and R. Hezel, "Optimised antireflection coatings for planar silicon solar cells using remote PECVD silicon nitride and porous silicon dioxide," Progress in Photovoltaics: Research and Applications **7**, 245–260 (1999).

162. T. S. Dory, "Process for plasma depositing silicon nitride and silicon dioxide films onto a substrate," United States patent US4877641A (October 31, 1989).

163. M. Kuramoto, C. Sasaoka, N. Futagawa, M. Nido, and A. A. Yamaguchi, "Reduction of Internal Loss and Threshold Current in a Laser Diode with a Ridge by Selective Re-Growth (RiS-LD)," physica status solidi (a) **192**, 329–334 (2002).

164. C. Henry, "Theory of the linewidth of semiconductor lasers," IEEE Journal of Quantum Electronics **18**, 259–264 (1982).

165. E. M. Purcell, H. C. Torrey, and R. V. Pound, "Resonance Absorption by Nuclear Magnetic Moments in a Solid," Phys. Rev. **69**, 37–38 (1946).

166. Y. Yamamoto, S. Machida, and G. Björk, "Microcavity semiconductor laser with enhanced spontaneous emission," Phys. Rev. A **44**, 657–668 (1991).

167. S. Kako, T. Someya, and Y. Arakawa, "Observation of enhanced spontaneous emission coupling factor in nitride-based vertical-cavity surface-emitting laser," Appl. Phys. Lett. **80**, 722–724 (2002).

168. E. Hashemi, J. Gustavsson, J. Bengtsson, M. Stattin, G. Cosendey, N. Grandjean, and Å. Haglund, "Engineering the Lateral Optical Guiding in Gallium Nitride-Based Vertical-Cavity Surface-Emitting Laser Cavities to Reach the Lowest Threshold Gain," Jpn. J. Appl. Phys. **52**, 08JG04 (2013).

169. M. Bender, W. Seelig, C. Daube, H. Frankenberger, B. Ocker, and J. Stollenwerk, "Dependence of oxygen flow on optical and electrical properties of DC-magnetron sputtered ITO films," Thin Solid Films **326**, 72–77 (1998).

170. H. Iwase, Y. Hoshi, and M. Kameyama, "Electrical properties of indium-tin oxide films deposited on nonheated substrates using a planar-magnetron sputtering system and a facing-targets sputtering system," Journal of Vacuum Science & Technology A **24**, 65–69 (2005).

171. L. Kerkache, A. Layadi, E. Dogheche, and D. Rémiens, "Physical properties of RF sputtered ITO thin films and annealing effect," J. Phys. D: Appl. Phys. **39**, 184–189 (2005).

172. X. A. Cao, S. J. Pearton, A. P. Zhang, G. T. Dang, F. Ren, R. J. Shul, L. Zhang, R. Hickman, and J. M. Van Hove, "Electrical effects of plasma damage in p-GaN," Appl. Phys. Lett. **75**, 2569–2571 (1999).

173. E. D. Haberer, C. H. Chen, M. Hansen, S. Keller, S. P. DenBaars, U. K. Mishra, and E. L. Hu, "Enhanced diffusion as a mechanism for ion-induced damage propagation in GaN," Journal of Vacuum Science & Technology B: Microelectronics and Nanometer Structures Processing, Measurement, and Phenomena **19**, 603–608 (2001).

174. S. Kaneko, H. Torii, M. Soga, K. Akiyama, M. Iwaya, M. Yoshimoto, and T. Amazawa, "Epitaxial Indium Tin Oxide Film Deposited on Sapphire Substrate by Solid-Source Electron Cyclotron Resonance Plasma," Jpn. J. Appl. Phys. **51**, 01AC02 (2012).

175. E. Kubota, Y. Shigesato, M. Igarashi, T. Haranou, and K. Suzuki, "Effects of Magnetic Field Gradient on Crystallographic Properties in Tin-Doped Indium Oxide Films Deposited by Electron Cyclotron Resonance Plasma Sputtering," Jpn. J. Appl. Phys. **33**, 4997 (1994).

176. J. T. Leonard, D. A. Cohen, B. P. Yonkee, R. M. Farrell, S. P. DenBaars, J. S. Speck, and S. Nakamura, "Smooth e-beam-deposited tin-doped indium oxide for III-nitride vertical-cavity surface-emitting laser intracavity contacts," Journal of Applied Physics **118**, 145304 (2015).

177. D. Raoufi, A. Kiasatpour, H. R. Fallah, and A. S. H. Rozatian, "Surface characterization and microstructure of ITO thin films at different annealing temperatures," Applied Surface Science **253**, 9085–9090 (2007).

178. G. Gonçalves, E. Elangovan, P. Barquinha, L. Pereira, R. Martins, and E. Fortunato, "Influence of post-annealing temperature on the properties exhibited by ITO, IZO and GZO thin films," Thin Solid Films **515**, 8562–8566 (2007).

179. H. R. Fallah, M. Ghasemi, A. Hassanzadeh, and H. Steki, "The effect of annealing on structural, electrical and optical properties of nanostructured ITO films prepared by e-beam evaporation," Materials Research Bulletin **42**, 487–496 (2007).

180. T. Gerfin and M. Grätzel, "Optical properties of tin-doped indium oxide determined by spectroscopic ellipsometry," Journal of Applied Physics **79**, 1722–1729 (1996).

181. R. A. Synowicki, "Spectroscopic ellipsometry characterization of indium tin oxide film microstructure and optical constants," Thin Solid Films **313–314**, 394–397 (1998).

182. J. F. Muth, J. H. Lee, I. K. Shmagin, R. M. Kolbas, H. C. Casey, B. P. Keller, U. K. Mishra, and S. P. DenBaars, "Absorption coefficient, energy gap, exciton binding energy, and recombination lifetime of GaN obtained from transmission measurements," Appl. Phys. Lett. **71**, 2572–2574 (1997).

183. J. H. Klootwijk and C. E. Timmering, "Merits and limitations of circular TLM structures for contact resistance determination for novel III-V HBTs," in *Proceedings of the 2004 International Conference on Microelectronic Test Structures (IEEE Cat. No.04CH37516)* (2004), pp. 247–252.

184. D. K. Schroder, *Semiconductor Material and Device Characterization* (Wiley-Interscience, 2006).

185. L. F. Lester, J. M. Brown, J. C. Ramer, L. Zhang, S. D. Hersee, and J. C. Zolper, "Nonalloyed Ti/Al Ohmic contacts to n-type GaN using high-temperature premetallization anneal," Appl. Phys. Lett. **69**, 2737–2739 (1996).

186. H. Y. Ryu, K. H. Ha, J. K. Son, S. N. Lee, H. S. Paek, T. Jang, Y. J. Sung, K. S. Kim, H. K. Kim, Y. Park, and O. H. Nam, "Determination of internal parameters in blue InGaN laser diodes by the measurement of cavity-length dependent characteristics," Appl. Phys. Lett. **93**, 011105 (2008).

187. S. Mogg, N. Chitica, U. Christiansson, R. Schatz, P. Sundgren, C. Asplund, and M. Hammar, "Temperature sensitivity of the threshold current of long-wavelength InGaAs-GaAs VCSELs with large gain-cavity detuning," IEEE Journal of Quantum Electronics **40**, 453–462 (2004).

188. B. Lu, P. Zhou, J. Cheng, K. J. Malloy, and J. C. Zolper, "High temperature pulsed and continuous-wave operation and thermally stable threshold characteristics of vertical-cavity surface-emitting lasers grown by metalorganic chemical vapor deposition," Appl. Phys. Lett. **65**, 1337–1339 (1994).

189. S. M. Mishkat-Ul-Masabih, A. A. Aragon, M. Monavarian, T. S. Luk, and D. F. Feezell, "Electrically injected nonpolar GaN-based VCSELs with lattice-matched nanoporous distributed Bragg reflector mirrors," Appl. Phys. Express **12**, 036504 (2019).

190. F. R. Nash, "Mode guidance parallel to the junction plane of double-heterostructure GaAs lasers," Journal of Applied Physics **44**, 4696–4707 (1973).

191. J. Piprek, Y. A. Akulova, D. I. Babic, L. A. Coldren, and J. E. Bowers, "Minimum temperature sensitivity of 1.55 μm vertical-cavity lasers at −30 nm gain offset," Appl. Phys. Lett. **72**, 1814–1816 (1998).

192. J. Piprek, D. I. Babić, and J. E. Bowers, "Simulation and analysis of 1.55 μm double-fused vertical-cavity lasers," Journal of Applied Physics **81**, 3382–3390 (1997).

193. J. Piprek, "High-temperature lasing of long-wavelength VCSELs: problems and prospects," in *Vertical-Cavity Surface-Emitting Lasers* (International Society for Optics and Photonics, 1997), Vol. 3003, pp. 182–194.

194. E. Kioupakis, P. Rinke, K. T. Delaney, and C. G. Van de Walle, "Indirect Auger recombination as a cause of efficiency droop in nitride light-emitting diodes," Appl. Phys. Lett. **98**, 161107 (2011).

195. Y. M. Zhang, J. Piprek, N. Margalit, M. Anzlowar, and J. Bowers, "Cryogenic performance of double-fused 1.5-/spl mu/m vertical cavity lasers," Journal of Lightwave Technology **17**, 503–508 (1999).

196. M. Kubota, K. Okamoto, T. Tanaka, and H. Ohta, "Temperature dependence of polarized photoluminescence from nonpolar m-plane InGaN multiple quantum wells for blue laser diodes," Appl. Phys. Lett. **92**, 011920 (2008).

197. D. G. Cahill, "Thermal-conductivity measurement by time-domain thermoreflectance," MRS Bulletin **43**, 782–789 (2018).

198. D. G. Cahill, "Analysis of heat flow in layered structures for time-domain thermoreflectance," Review of Scientific Instruments **75**, 5119–5122 (2004).

199. A. J. Schmidt, R. Cheaito, and M. Chiesa, "A frequency-domain thermoreflectance method for the characterization of thermal properties," Review of Scientific Instruments **80**, 094901 (2009).

200. M. D. Kamatagi, N. S. Sankeshwar, and B. G. Mulimani, "Thermal conductivity of GaN," Diamond and Related Materials **16**, 98–106 (2007).

201. M. J. As'adi, K. Abbasian, D. Armaghan Bostanabad, and T. Nurmohammadi, "Thermal analysis of high-index-contrast grating (HCG)-based VCSEL," Optik **125**, 4017–4022 (2014).

202. M. Osinski and W. Nakwaski, "Effective thermal conductivity analysis of 1.55 mu m InGaAsP/InP vertical-cavity top-surface-emitting microlasers," Electronics Letters **29**, 1015–1016 (1993).

203. V. O. Turin and A. A. Balandin, "Electrothermal simulation of the self-heating effects in GaN-based field-effect transistors," Journal of Applied Physics **100**, 054501 (2006).

204. G. P. Agrawal, *Fiber-Optic Communication Systems*, 4 edition (Wiley, 2010).

205. D. Feezell, D. A. Buell, D. Lofgreen, M. Mehta, and L. A. Coldren, "Optical Design of InAlGaAs Low-Loss Tunnel-Junction Apertures for Long-Wavelength Vertical-Cavity Lasers," IEEE Journal of Quantum Electronics **42**, 494–499 (2006).

206. T.-C. Lu, C.-C. Kao, H.-C. Kuo, G.-S. Huang, and S.-C. Wang, "CW lasing of current injection blue GaN-based vertical cavity surface emitting laser," Appl. Phys. Lett. **92**, 141102 (2008).

207. A. Rashidi, M. Monavarian, A. Aragon, A. Rishinaramangalam, and D. Feezell, "Nonpolar m-Plane InGaN/GaN Micro-Scale Light-Emitting Diode With 1.5 GHz Modulation Bandwidth," IEEE Electron Device Letters **39**, 520–523 (2018).

208. A. Rashidi, M. Monavarian, A. Aragon, S. Okur, M. Nami, A. Rishinaramangalam, S. Mishkat-Ul-Masabih, and D. Feezell, "High-Speed Nonpolar InGaN/GaN LEDs for Visible-Light Communication," in *Conference on Lasers and Electro-Optics (2017), Paper STh1C.7* (Optical Society of America, 2017), p. STh1C.7.